Synthesis and application of hybrid materials based on plasmonic nanoparticles

D i s s e r t a t i o n

zur Erlangung des akademischen Grades
d o c t o r r e r u m n a t u r a l i u m
(Dr. Rer. Nat.)
im Fach Chemie

eingereicht an der
Mathematisch-Naturwissenschaftlichen Fakultät
der Humboldt-Universität zu Berlin
von

M. Sc. Andreas Ott

Präsident der Humboldt-Universität zu Berlin
Prof. Dr. Jan-Hendrik Olbertz

Dekan der Mathematisch-Naturwissenschaftlichen Fakultät
Prof. Dr. Elmar Kulke

Gutachter/in: 1. Prof. Dr. Matthias Ballauff

2. Prof. Dr. Oliver Benson

Datum der Einreichung: 26.01.2016

Datum der Promotion: 17.05.2016

I have been so electrically occupied of late that I feel as if hungry for a little chemistry: but then the conviction crosses my mind that these things hang together under one law and that the more haste we make onwards each in his own path the sooner we shall arrive, and meet each other, at that state of knowledge of natural causes from which all varieties of effects may be understood and enjoyed.

— Michael Faraday 1838, letter to Eilhard Mitscherlich.

Abstract

Hybrid nanostructures combine the assets of the individual materials with a vast amount of new properties. In this work various metal nanoparticles have been synthesized and investigated on their optical properties. The synthesized metal nanoparticles have been implemented for potential applications, e.g. fabrication of a spaser or in solar cells. At first, the size, shape and refractive index effects of gold and silver nanoparticles have been investigated. The insight gained helps to optimize the synthesis of metal nanoparticles with specific optical properties needed for further applications.

Optimized hybrid gold nanostructures have been synthesized and functionalized with dye molecules or quantum dots to investigate energy transfer effects. These hybrid structures have been optically pumped to achieve spasing. However, comparison with a theory showed that such metal nanostructures need unrealistic high gain to overcome the inherent losses and achieve spasing.

Silver and gold nanoparticles have been synthesized for applications in thin film solar cells. It has been shown that silver lacks chemical stability and thus, if oxidized, the nanoparticles exhibit weak scattering and strong Ohmic losses. The oxide layer of silver nanospheres could be via annealing. By contrast, gold nanoparticles, known for their higher stability, have been implemented in a perovskite solar cell. Such a modified solar cell showed an increase in efficiency by ~40% through increased generation of carriers.

Anisotropic Janus carrier systems have been synthesized and functionalized with metal nanoparticles. Gold nanoparticles have been deposited either uniformly or on one lobe only of the dumbbell-shaped carrier system by using its chemical anisotropy. These gold nanoparticles have been grown to a gold shell. Platinum nanoparticles have been deposited on a single lobe and its self-propelling ability in a chemical fuel was investigated by means of dynamic light scattering.

Keywords: metal nanoparticles, plasmonics, spaser, solar cell, light trapping, hybrid nanoparticles.

Zusammenfassung

Hybride Nanostrukturen verbinden die Vorzüge von individuellen Materialien, die neue Eigenschaften hervorrufen können. In dieser Arbeit wurden verschiedene Metal Nanostrukturen synthetisiert und deren optische Eigenschaften analysiert. Die Herstellung eines Spasers oder Lichteinfang in Solarzellen wurde untersucht. Der Einfluß von Größe, Form und Brechungsindex auf die Metal-Plasmonen wurde erforscht. Die gewonnen Erkenntnisse genutzt um Metal Nanopartikel mit gezielten Eigenschaften herzustellen.

Hybride Gold Nanostrukturen (funktionalisiert mit Farbstoffen oder Quantenpunkten) wurden hergestellt und Energie-Transfereffekte untersucht. Diese hybriden Nanostrukturen wurden optisch gepumpt um Spasing zu erreichen. Allerdings wurde festgestellt, dass eine unrealistisch hohe Verstärkung benötigen wird, um die charakteristischen Verluste im Metal zu überwinden.

Silber und Gold Nanopartikel wurden synthetisiert um diese in Dünnschichtsolarzellen einzusetzen. Es konnte gezeigt werden, dass Silber chemisch instabil ist und, wenn oxidiert, hohe Absorption auftritt. Durch hohe Temperaturen konnte die Oxidschicht auf den Silberpartikeln reduziert werden und damit auch die Verluste. Stabilere Gold Partikel wurden in Perovskit-Solarzellen eingebaut, wodurch die Effizienz einer solch modifizierten Solarzelle um ~40% gesteigert werden konnte. Dies wurde durch eine erhöhte Anzahl an generierten Ladungsträgern mittels metallischen Lichtfallen erreicht.

Zusätzlich wurden anisotrope Janus Trägerpartikel synthetisiert und mit Metal Nanopartikeln funktionalisiert. Gold Nanopartikel wurden abgeschieden und zu einer Gold Hülle gewachsen. Dies erfolgte entweder gleichförmig über das gesamte Hantel-Trägerpartikel oder einseitig unter Ausnutzung der chemischen Anisotropie. Desweiteren wurden Platin Nanopartikel einseitig abgeschieden und in Wasserstoffperoxid Lösung gegeben. Die Partikel wurden daraufhin mittels dynamischer Lichtstreuung auf Selbstvortrieb untersucht.

Schlagwörter: Metal Nanopartikel, Plasmonik, Spaser, Solarzellen, Lichtfalle, hybride Nanopartikel.

Table of Content

1. Introduction

1.1 Optical properties of metal nanoparticles

Derived from the Greek word "nano", meaning dwarf in English, nanoparticles are microscopic objects in the size range of 1 nm to 100 nm.[1] For a long time such objects were hidden from the human eye due to the fundamental limit that light cannot be focused down to a spot smaller than half of its wavelength (Abbe-limit).[2] The wavelength region for visible light is around 400 – 750 nm, making it impossible with common optical microscopes to investigate these objects.

However, nanoparticles made of copper, gold and silver have a long history. Without the awareness of actually producing nanoparticles, glass stainers used for more than 3000 years techniques to reduce metal compounds in the presence of a suitable reducing agent to form nanoparticles in the glass melt. The first coloured glasses have been fabricated in Egypt and Mesopotamia with copper or cuprite nanoparticles incorporated.[3] An outstanding example of coloured glasses is the cup of Lycurgus made in 324 A.D. Its glass shows a green jade colour when illuminated from outside due to scattered light of gold-silver alloy nanoparticles of 50 – 100 nm size.[4] When the cup is illuminated from the back, however, it shows a bright red colour which results from absorbed light, caused by the nanoparticles. In the medieval age copper nanoparticles were used to stain glasses red for windows in churches.[4] Around the 15th to 16th century first written documents appeared that showed how to use gold to attain red stained glass and it was suspected that very small gold particles are involved.

To support the wave theory of light, Faraday fabricated and investigated gold nanoparticles in 1857. He wanted to demonstrate that subwavelength objects strongly interact with the light waves by showing that the gold nanoparticle suspensions absorb light, which results in the red colour. However, he was not aware that he had succeeded.[5] Zsigmondy proved the colloidal and metallic character of gold nanoparticles in solution in 1898.[6] With the help of Siedentopf, he was able to observe gold nanoparticles directly in gold ruby glass and estimate their size using their invented ultra-microscope, a microscope similar to dark field microscopes.[7] Later on, they were also able to convincingly show that colloids are nano- to micrometre-sized particles that are dispersed in the liquid. He was therefore awarded with the Nobel Prize in chemistry in 1925.

Maxwell developed his theory of light being an electromagnetic wave around the same

Figure 1.1: Images of the Lycurgus cup when illuminated from the front (left) or inside (right). © Trustees of the British Museum.

time as Faraday was searching for the experimental proves.[8] He was able to mathematically link optical and electromagnetic properties. In 1908 Mie solved the exact solution to Maxwell's equation for the optical response of an arbitrary sized sphere which is subject to an electromagnetic wave.[9] The derived scattering spectra show resonant structures which we call today plasmon resonances and can explain the colour of colloidal metal nanoparticles.

The term plasmon was not used until the 1950s. Similar to gaseous plasmas, which are oscillations of electron densities, the metal electrons can oscillate collectively. Compared to gaseous plasma, however, the electron density in metals is much higher which leads to a higher plasma frequency. Quantization of such plasma oscillations resulted in a new quasi-particle that was named plasmon. Bulk plasmons travel through the metal as longitudinal waves and cannot be excited directly by transversal light waves. Yet, they can be excited by high energy electrons which can be monitored in electron energy loss spectroscopy. In 1957 Ritchie derived a theory to explain the lower-energy losses of thin metal foils that have been found in experiments.[10] These plasma oscillations travel along the surface of a metal and couple strongly to electromagnetic fields near the metal surface and are called surface plasmon polaritons (SPP). Though these waves are of transversal nature they cannot be directly excited by light due to the difference in momentum of light and SPP. By using a prism with a high refractive index or patterned metal surfaces light can excite the SPP of a metal.[11, 12] The interest in SPP was facilitated since then and led to the discovery of dramatically increased Raman scattering signals of pyridine on a rough silver surface in 1974.[13] Though discussed controversially, the effect was attributed to the strongly enhanced electromagnetic fields generated by the SPP and called surface enhanced Raman scattering (SERS).[14]

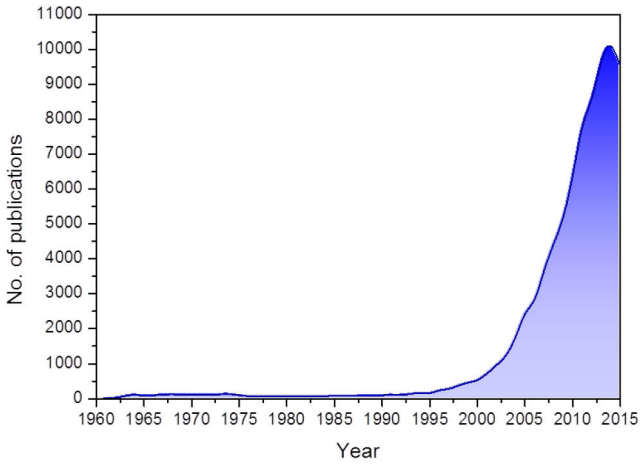

Figure 1.2: Number of annual publications as listed on the Scopus database with the search for gold and silver metal nanoparticles/colloids.

Recent advances in tools for characterization (like electron microscopy and atomic force microscopy) and nano-fabrication led to a rapidly emerging interest in metal nanoparticles since the 1990s (Figure 1.2). As the electromagnetic wave cannot propagate on a metal nanoparticle surface that is much smaller than the light, the electron oscillations are strongly localized. These oscillations are hence called localized surface plasmon resonances (LSPR). They are highly dependent on the shape and size of a metal nanoparticle.

Metal nanoparticles and –structures can nowadays be fabricated on demand to fulfil the needs for individual purpose-built applications. The use of the high and surface-sensible electromagnetic fields generated at the metal interface led to various sensor based applications like SERS[13, 15], refractive index sensing[16, 17], scanning near-field optical microscopy[18-20] and metal enhanced fluorescence[21-26]. All sensing applications have in common, that single molecule detection is in theory possible. Additionally, metal nanostructures find implementation in thin film solar cells[27-29] and more unconventional utilization, e.g. surface plasmon amplification by stimulated emission of radiation (spaser)[30-33], optical trapping[34] or metamaterials[35]. Sometimes closely related to the field of "plasmonics" (the research field of electron-oscillations in metals), metal nanoparticles attained great attention in the area of catalysis[29, 36-38], energy conversion[39], imaging,[40-42] and medicine[40, 42-44].

1.2 Strong local electric fields and loss compensation

Naturally, a mismatch between the characteristic wavelengths of photons and electrons exists, which leads to slow and weak light-matter interactions.[45] The field of "nano-optics", however, deals with interactions that are much stronger and faster and enhances weak effects like

Raman scattering. The reason for this is the dramatically increased electric field, the "near-field", around the metal nanostructure. The metal nanoparticle acts as an antenna that concentrates the light in a small spot via surface plasmon generation. These near-fields can induce non-linear effects (e.g. electron-phonon coupling or harmonic generation)[46] and strongly interact with any matter in the vicinity. Interactions with the intense local electric field induce enhanced optical processes like emission or absorption.[14, 47] These enhancements are the origin for useful applications like SERS and metal enhanced fluorescence.

Light concentration and the generation of high local fields has been the field of dielectric lenses and resonators previously. Due to the fundamental law of the diffraction limit (Abbe limit), the light cannot be focussed down to smaller spots than half of the wavelength and the mode volume is limited to $v_m \sim (\lambda/2)^3$.[48] Metal nanoparticles, however, overcome this limitation by exciting surface plasmons that squeeze light radiation into subwavelength volumes. In contrast to dielectric photonic structures, inherent dissipative losses in metals are present. They occur due to inelastic non-radiative processes of the electron oscillations or radiative scattering. These optical losses inhibit applications of plasmonic technologies like subwavelength photonic circuits. Compensation or elimination of these losses is now being actively investigated by introduction of optical gain.[45, 49]

One way to overcome losses in metal nanoparticles was theoretically described by Bergman and Stockman in 2003.[30] Surface plasmon amplification by stimulated emission of radiation (spaser) describes the amplification of surface plasmons. Hence, it would be suitable for an active element in ultra-small photonic circuits with very fast switching properties (< 100 fs) and has potential applications in probing nano-objects as a coherent light source with high spatial resolution.[45] The required gain can be provided by semiconductors or molecules.

Currently, there are numerous publications of plasmonic lasers that use metal slabs as plasmon source and semiconductor materials as cavity and gain materials. These systems are nanometre-sized in one dimension but quite elongated in the other directions.[50-55] They use a Fabry-Pérot cavity with SPPs propagating at the interface of the metal, and therefore are rather called plasmonic lasers.[45] The first successful experimental realization was in 2009.[50] In the same year, Noginov *et al.* proposed a true nanoscopic spaser system that consisted of a spherical 14 nm gold core and a silica shell with embedded dye molecules as gain medium.[31] At high pump rates the emission spectrum showed a narrow peak with high intensities and no saturation was found. However, this spaser system has been investigated in solution with an ensemble of millions of nanoparticles and it cannot be ruled out that a cooperative effect or

other effects caused the measured signal. Hence, it is highly desirable to unambiguously prove spasing for individual particles and another demonstration of such a system has yet to be repeated. Furthermore, there are certain limits for the used gain medium beyond the problem of dye solubility, e.g. self-quenching etc. The high pump rates that are needed additionally lead to degradation of the dye molecules. Hence, such a system should be carefully investigated to unambiguously demonstrate spasing.

1.3 Plasmonic solar cells

The International Energy Agency estimated the total world energy consumption in 2012 to be 17.7 TW with one major branch for electric energy generated (~18%). This equals 3.2 TW and the main sources of electric energy have been fossil fuels, hydroelectricity and nuclear power.[56] However, renewable energy sources and in particular solar cells have an exponential growth, generating 176 GW in 2014.[57] The prime solar cell type used is based on crystalline silicon waver. Silicon, as a material, has proven to be an ideal photovoltaic material: (i) it is abundant, (ii) has a nearly optimal bandgap, (iii) excellent junction formation, (iv) high carrier diffusion length and (v) effective surface passivation methods. The only demerit of silicon is the low absorption of the solar spectrum, in particular at higher wavelengths.[27] Hence, typical silicon wafers are several 100 μm thick, which causes the highest cost factor in solar cell production nowadays.

Thin-film solar cells can drastically reduce the costs and allow the utilization of scarce materials (tellurium, indium, gallium). Such solar cells, however, suffer from low absorbance. Through light-trapping, such limitations can be overcome and in the laboratory thin-film solar cells have already out-performed multi-crystalline silicon solar cells.[58] Metal nanoparticles provide possibilities to efficiently trap light in the active domain of the solar cells and increase the effective path length through the absorber or increase the electron-hole formation.

Important factors for large scale applications of metallic structures are cheapness, control over morphology and density, and high throughput. Metal nanoparticles produced by wet chemistry can fulfil these requirements but several aspects need to be addressed. This can be e.g. proper particle design with high/low albedo (fraction of light scattered to the far-field) or oxidation effects.

1.4 Objectives of this thesis

The aim of the present thesis is to use the unique optical properties of metal nanoparticles and combine their highly generated electromagnetic fields with their surrounding medium to implement them in future possible devices. The work focuses mainly on silver and gold nanoparticles as these two metals show LSPR that are active in the ultra-violet (UV) to near-infrared (NIR) region and hence, find most attention in this research area. High electromagnetic fields are generated when the LSPR of metal nanoparticles are stimulated, which can couple efficiently to its surrounding medium. The size and shape of the metal nanoparticles must be precisely adjusted and a high degree of quality is necessary (i.e. avoiding oxides, erratic surfaces, low dispersity etc.). The work has been split into four different topics:

(i) The first part of the thesis shows the effect of the size, shape, material and the surrounding medium on the optical properties of metal nanoparticles. Therefore, gold and silver nanoparticles with spherical, cubic and rod-like shapes have been synthesized. Furthermore, these metal nanoparticles have been coated with e.g. a polymer microgel to show the effect of the refractive index on the LSPR.

(ii) Efficient energy transfer from dye molecules to gold nanoparticles has been achieved by spatial and spectral overlap. Two kinds of shapes (quasi-spherical/rod-shaped) and different sizes of gold nanoparticles have been synthesized to match the emission of the dye molecules with the LSPR. Various approaches have been followed to bring dye molecules near the gold nanoparticle: First, gold-silica core-shell nanoparticles with dye molecules embedded in the silica shell were fabricated. Second, gold nanoparticles have been functionalized via layer-by-layer approach with polymers modified with dye molecules. Third, thin dye films have been spin-casted with gold nanoparticles embedded in these films. And fourth, quantum dots have been attached to a polymer microgel which is coated on the gold nanoparticle. Solution based methods and single particle investigations were used to characterize these hybrid systems and were investigated on spaser phenomena.

(iii) Plasmonic metal nanoparticles have been fabricated which exhibit strong scattering properties. Quasi-spherical and rod-shaped nanoparticles of silver and gold have been synthesized for implementation in thin-film solar cells. These particles showed increased absorption of light in the active absorber, which

potentially increases the efficiency of solar cells. Silver nanoparticles have shown high dependency of the oxidation state of the surface and a thoroughly investigation of their optical properties was conducted.[59] Gold nanorods were embedded in a perovskite solar cell and showed an increased efficiency by ~40%.

(iv) Janus dumbbell-shaped particles have been synthesized and used as a carrier system. This carrier system provides broad modification possibilities via silane and polymer chemistry. Open gold semi-shells and dumbbell-shaped gold shells were fabricated with altered plasmonic properties. The modification process is rational and can be easily adapted to other metal nanoparticles (e.g. platinum) with new functionalities.

2. Fundamentals and theory

2.1 Preparation and stabilization of metal nanostructures

Metal nanostructures preparation can be divided in two main methods: “top-down” and “bottom-up”. Top-down approaches usually involve physical methods with a substrate present. There are numerous elaborate techniques that have been mainly developed specifically for the semiconductor industry to miniaturize transistors.[60] On the other hand bottom-up approaches are made by chemical methods based in solution and involve the reduction of a metal salt.

The sophisticated physical methods can produce regular and well-defined metal nanostructures on substrates that can be reproduced with high accuracy. However, most techniques are limited to feature sizes of 10 nm and are not able to produce three-dimensional objects, as they are grown on a substrate. Some examples for top-down methods are optical lithography[60], electron beam lithography[61], focused-ion beam milling[62], soft lithography, stencil lithography[60, 63], laser ablation[38] and ball milling[64].

Chemical methods can produce rather high amounts of metal nanoparticles that overcome these limitations. Nonetheless, these methods have their drawbacks, i.e. complicate synthesis for advanced shapes and possible oxidation of metal surfaces, as these methods are solution-based. Oxidation e.g. of silver under ambient conditions is a common issue. Therefore gold nanoparticles are a reasonable alternative, though it suffers from greater optical losses than silver.

2.1.1 Bottom-up methods

As mentioned in the section before, top-down processes suffer from resolution limits. Edge roughness, defects and grain boundaries in the metals lead to optical losses. For strong plasmonics effects this can be overcome by the use of bottom-up methods. Wet chemical synthesis of nanoparticle colloids is by far the most popular method. It allows for high control over size and shape and further functionalization.

As mentioned earlier, Faraday in the 19th century was pioneering in the field of colloidal fabrication of gold nanoparticles. His preparation technique is the fundamental scheme of today’s modern metal nanoparticle chemistry. A metal salt or complex is dissolved in a liquid and reduced by appropriate reducing agents to their zero valence state. Small nuclei (clusters) form initially which will grow subsequently. The capping material is of utmost importance in

the growth process. It determines shape, size, and polydisperity and stabilizes the resulting particles. The binding strength of the capping agent and the metal surface must be matched well, as weak bonds will lead to growth of very large particles and/or aggregation, while too strong binding can limit further growth of the nanoparticle. Commonly, metal nanoparticles are stabilized by molecules via electrostatic repulsion. In the simplest case, the capping material is the reducing agent as well. In the mid-20th century Turkevich developed a method to synthesize monodisperse gold nanoparticles by the reduction of chlorauric acid with sodium citrate in boiling water.[65] Frens improved the reaction and showed that the size can be tuned by the amounts of citrate molecules in the range of 5 - 100 nm.[66, 67] This is possible as citrate acts not only as a reducing agent but also as a stabilizer. With more citrate present in the reaction solution larger surface areas can be stabilized leading to smaller gold nanoparticles. Similarly silver nanoparticles can be produced.[68] However, the particle size distribution varies significantly as silver is more reactive, which results in overlap of nucleation and growth of the silver nanoparticles. There have been attempts to slow down the reaction by using a more viscous solvent (e.g. ethylene glycol) or seed mediated growth to attain regular sized quasi-spherical silver nanoparticles.[69, 70]

Even for well controlled reactions larger metal nanoparticles usually become more polydisperse as nucleation and growth appear at the same time. Clusters continue to develop while previously formed particles are already growing. This issue can be overcome by using the seed mediated growth of metal nanoparticles. For example, monodisperse citrate stabilized gold nanoparticles of 14 nm in diameter can be used as seeds and grow to larger quasi-spherical nanoparticles of up to 200 nm in size.[71] Nucleation must be avoided in the growth step to fabricate monodisperse samples. Therefore, a weak reducing agent is used (e.g. ascorbic acid or hydrazine for gold) which allows reduction only on the existing metal surface. This method is not only used for growing larger spherical particles, but also for shape control.

The optical properties of metal nanoparticles strongly depend on their shape. Thus, it is desirable to manipulate the shape for fundamental research and applications. If the capping agent has structure directing properties, anisotropic shape can be induced. A prominent example is gold nanorods. Quasi-spherical gold seeds of a few nanometres in size are produced by reduction of chlorauric acid with a strong reducing agent (sodium borohydride) in the presence of the surfactant CTAB (cetyltrimethylammonium bromide). The growth solution consists of chlorauric acid reduced by ascorbic acid, which is a much weaker

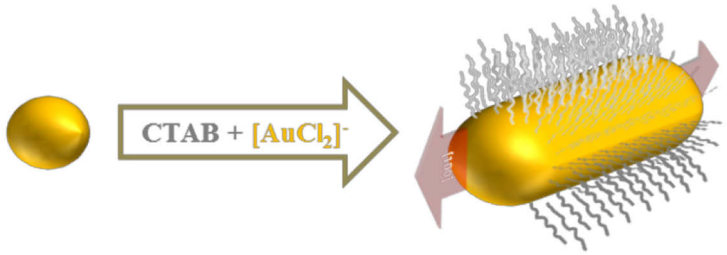

Figure 2.1: One-dimensional growth of gold nanorods via facet-specific binding of CTAB molecules. The diffusion of the gold(I) complex is limited at higher CTAB densities inhibiting isotropic growth.

reducing agent. The surfactant CTAB that stabilizes the gold nanoparticles has different preferential adsorption on the various gold facets. It was proposed that CTAB micelles or a CTAB double layer are adsorbed on the gold surface with different densities. A lower density of adsorbed CTAB molecules on the gold {111} facet offers more/wider channels for the reactive gold species and, therefore, grows preferentially in the elongated [100] direction.[72, 73] However, the amount of gold nanorods is still low and the nanorods have variations in their aspect ratio. This is improved significantly by adding silver ions to the reaction.[74]

Besides the wet chemical synthesis there are other bottom-up methods, e.g. electrodeposition.[75] Electrodeposition is similar to the wet chemical synthesis. Instead of adding a reducing agent as electron source, a dissolved metal salt is reduced on the working electrode by applying a potential and supplying the electrons. Various shapes can be formed as well via different capping agents.[76, 77] Additionally soft and hard templates can be used to structure the metal on the substrate.[78, 79]

Today, many different shapes like spheres, rods, wires, stars, cubes, triangles, pyramids and octahedrons can be synthesized via wet chemical methods.[80] The synthesis of anisotropic nanomaterials is not only limited to various metals; metal oxides[81, 82] and semiconductor materials[83] have sophisticated synthesis protocols as well.

2.1.2 Stabilization of colloidal metal nanoparticles

Chapter 2.1.1 discussed the importance of the capping agent that stabilizes the metal nanoparticle in the solution. There are various capping agents, from molecules to polymers, which can be hydrophilic in aqueous reactions or hydrophobic in oil-phase reactions. The metal nanoparticles synthesized are usually susceptible to aggregation if the external conditions in the dispersion changes e.g. induced by changing the pH and salt concentrations, increase in temperature or introduction of a new solvent. Aggregation of metal nanoparticles usually is not desired, as the optical properties are greatly altered due to coupling effects and is therefore an important matter in the preparation of optically active nanoparticles.[84, 85]

Metal nanoparticles formed in aqueous media are stabilized by charged molecules like citrate or by surfactants like CTAB.[65-67, 72] These nanoparticles are stabilized via electrostatic repulsion and can be described by the DLVO theory. Bio-inspired routes have been employed as well where peptides or proteins are used to stabilize the metal nanoparticles.[86-88] Non-aqueous polar media like glycol stabilizes particles commonly via polymers like polyvinylpyrrolidone (PVP).[69, 80] Polymeric stabilizers for metal nanoparticles have been widely investigated because they not only offer effective protection (steric stabilization). They also adjust solubility and amphiphilicity as well as allow for functionalization.[89] As an example, gold nanoparticles have been functionalized with adsorption of various layers of alternating positive and negative polyelectrolytes (layer-by-layer method).[24] These polyelectrolytes have been functionalized with dye molecules and the distance-dependent fluorescence quenching/enhancement was investigated. Similarly, poly(ethylene glycol) functionalized nanoparticles have been widely used to make nanoparticles stable under physiological conditions and have promises in pharmaceutical and biological applications.[44]

Metal nanoparticles dispersed in organic solvents usually are synthesized in reversed micelles where water droplets containing the metal salt are dispersed in an oil phase. These droplets are stabilized by surfactants or block-copolymers and define the particle size of the metal nanoparticles, which have been reduced inside these droplets.[90-92] Another approach to stabilize metal nanoparticles in organic solvents is to exchange capping agents, usually via thiol alkanes.

Metal nanoparticles stabilized by core-shell formation

To stabilize metal nanoparticles and preserve their unique optical properties a thicker protective shell around the metal nanoparticle can be synthesized. This shell may consist of a polymer network or metal oxides. These shells can be charged and provide additionally steric stabilization. Therefore, such systems show higher colloidal stability than the blank metal nanoparticles. A shell formed around a metal nanoparticle benefits not only of higher stability, but allows also for functionalization with new reactive groups and incorporation of active molecules[21, 25, 26, 31-33, 93, 94], environment responsive behaviour (e.g. temperature or pH)[94-96] or bio-compatibility[42]. Two important examples of possible shells shall be mentioned here: inorganic amorphous silica and thermosensitive poly(N-isopropylacrylamide) (PNIPA).

Amorphous silica shells have become one of the favourite methods to stabilize and functionalize metal nanoparticles. They offer multiple advantages: i) colloidal stability at high volume fractions, ii) stability in a wide range of different media, iii) optical transparency, iv)

chemical inertness, v) photochemical stability, vi) cheapness and vii) a simple coating methodology.[97] The first group to synthesize gold-silica core-shell nanoparticles were Mulvaney and Liz-Marzán in 2000.[97] They followed a modified Stöber process that produces monodisperse silica spheres.[98] The gold nanoparticles have been initially grafted with (3-aminopropyl) triethoxysilane (APTES) and sodium metasilicate to form a thin silica layer on the gold surface. Under Stöber process conditions an amorphous silica shell with adjustable thickness is grown by hydrolyzation and condensation of tetraethoxysilane (TEOS) (Figure 2.2). This process can be easily adapted to other metal nanoparticles.[25, 99] Besides the aforementioned merits of a silica shell, functionalization of the silica is easily possible due to numbers of different silane reagents like APTES. The surface supplies silanol (*Si-OH*) bonds that can be functionalized via grafting with new silane molecules or the silica shell itself is modified by co-condensation of TEOS derivatives. It has been shown that stable dye-functionalized silica particles were produced[100] and energy transfers between dye molecules and metal nanoparticles have been investigated.[21, 25, 26, 31-33, 99] This was achieved e.g. by covalently linking amine reactive dyes with APTES.

Another thoroughly investigated core-shell system is metal nanoparticles covered in a PNIPA network. There are multiple possibilities to form polymeric shells; however, PNIPA offers direct functionality due to its temperature responsive behaviour. Stimuli-responsive polymers attract a lot of attention as they have displayed to show selectivity in catalytic reactions[94], variable optical properties[101, 102] and switchable sensor sensitivity at different temperatures[103]. The nature of this thermoresponsive behaviour is a phase transition from coil

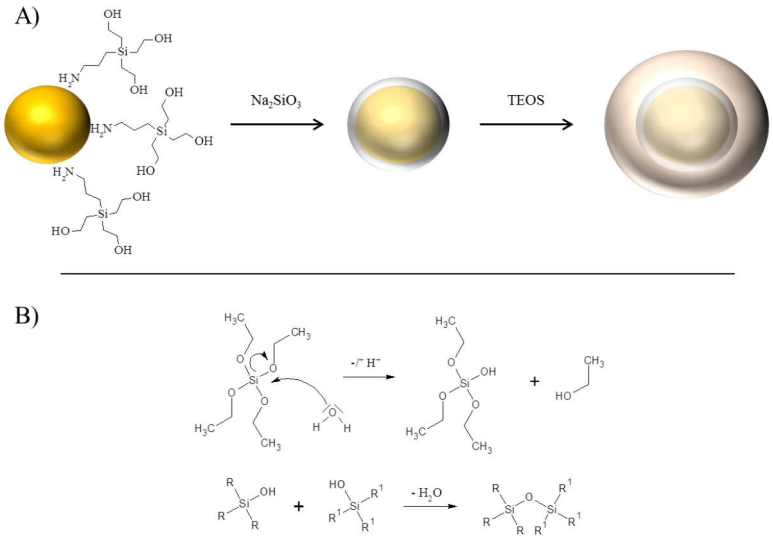

Figure 2.2: A) Modified Stöber process for silica coatings on metal nanoparticles. B) Reaction mechanism of hydrolyzation and condensation of TEOS that forms an amorphous silica network.

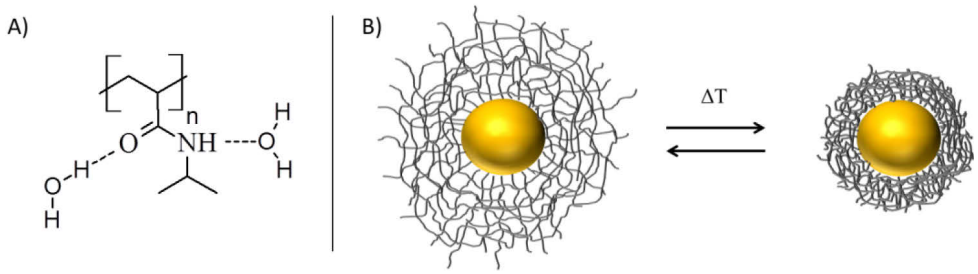

Figure 2.3: A) Chemical structure of PNIPA with amide groups that allow for hydrogen bonds with water below the LCST. Above the LCST hydrogen bonds are formed between the amide groups of different monomer-units. B) Swelling and shrinking behaviour of the PNIPA network below and above the LCST.

state to globule state where water gets excluded at the lower critical solution temperature (LCST). At low temperature water is a good solvent and forms hydrogen bonds with the amide groups of PNIPA. By increasing the temperature, water becomes a poor solvent and the amide groups of different monomer units form internal hydrogen bonds (Figure 2.3).[104, 105] There is a sharp transition in size between the swollen and collapsed state which alters also the hydrophobicity of the polymer network. The transition temperature of PNIPA is in a physiological important range (~ 30 °C), which generated immense interest for over 45 years since its discovery.[106] The synthesis of PNIPA shells on metal nanoparticles is done via radical seeded emulsion or precipitation polymerization that can be thermal or photo-initiated[95]. The polymerization can be assisted by grafting molecules on the metal nanoparticle surface that exhibit double bonds.[107] These core-shell systems show that functionality and stabilization can be achieved at the same time by using simple approaches. There are many other possible shell materials available that have been used for various applications.[108-110]

Carrier systems for metal nanoparticles

Metal nanoparticles may also be stabilized by carrier systems.[111] These can be larger colloidal particles, large surfaces on substrates,[112, 113] or monoliths[114, 115]. Metal nanoparticles are either grafted onto the surface after their synthesis or reduced *in-situ* at active surface centres by physisorption or chemisorption. Thiols commonly form strong covalent bonds with metal nanoparticles that have energies above 1 eV. Amines and carboxylates show weaker adsorption energies below 1 eV and the nanoparticles are less strong bound to the carrier system.[116, 117]

Colloidal carrier systems have a core particle that is functionalized with active centres as mentioned before. Common carrier systems are e.g. silica particles that have been grafted with silane reagents like APTES[118, 119] or thiols[120] on the surface. Polymeric colloidal carrier

systems usually consist of polyelectrolyte chains grafted on a solid polymer core[121, 122] or of a polymer network that is permeable ("microgel").[123-125] Their monomer units have active site centres which allow for the adsorption of metal nanoparticles directly or metal salts that can be reduced at these active sites.

Carrier systems are not only beneficial for their high stability, but also offer accessibility for reactions. As mentioned before, metal particles exhibit high catalytic activity. Furthermore, the metal nanoparticles can be modified; e.g. it was shown that by adding metal precursor salts and a mild reducing agent led to growth of the metal particles, which have been grafted on the carrier system. Eventually, a full metal shell around the carrier system was synthesized that exhibits new plasmonic properties.[126, 127]

A second tool that carrier systems can offer is morphological and chemical anisotropy. Chemical anisotropy, i.e. different functionality on one particle, is often referred as "Janus particle".[128] As an example, polymeric Janus dumbbell particles have been synthesized that consist of two connected spherical particles. The general route to produce such particles is to synthesize a cross-linked polymer sphere/shell by emulsion polymerization.[129, 130] From this sphere grows a second lobe via phase separation. The newly formed lobe can consist of a new polymer or exhibit a different surface that provides the chemical anisotropy, and hence multi-functionality.[129, 131, 132] With clever surface modifications different functional groups can be attached that provide nanoparticle stabilization and modification.[133] Furthermore, additional properties might be applicable due to the chemical anisotropy.

2.2 Plasmonic excitations in metals

As mentioned in the introduction, the optical properties of metal nanoparticles or films originate from collective electron oscillations, called plasmons. The free-electron gas at the Fermi-level starts to oscillate when it is subject to an electromagnetic plane wave. These charge-density waves oscillate against the positively charged background by the atomic cores of the metal.[114, 115] A simple classical, macroscopic model is able to provide an accurate and intuitive description of plasmons in metal nanoparticles. Using Maxwell's equations, plasmons are described as local polarizations of a metal nanoparticle.[47] The displacement field **D** responds to free charges and is related to the electric field **E**, which includes the polarization fields of the materials through a simple constitutive relation for an isotropic material via the frequency dependent dielectric permittivity ϵ:

$$\mathbf{D}(\omega) = \epsilon(\omega)\mathbf{E}(\omega). \tag{2.1}$$

The displacement field does not respond instantaneously to the applied electric field. Therefore, in the solution to Maxwell's equation ϵ is a function of the frequency ω, which is known as dispersion. Furthermore, the dispersion relation that connects the frequency ω and the wavevector **k** can be derived by:

$$\mathbf{k}^2 = \frac{\epsilon\omega^2}{c^2}. \tag{2.2}$$

From equation (2.1) it is now necessary to establish a model for the dielectric function $\epsilon(\omega)$ of the metal.

2.2.1 Bulk plasmons

The Drude model is the simplest model to calculate the dielectric response of a metal to an electromagnetic field. The free electrons at the Fermi-level are modelled as a gas of free, non-interacting electrons that relax through collisions with the lattice at a characteristic decay time τ. The Drude form of the dielectric function results as:

$$\epsilon(\omega) = \epsilon_0(\omega) - \frac{\epsilon_0(\omega)\omega_p^2}{\omega^2 + \frac{i\omega}{\tau}} \tag{2.3}$$

with the bulk plasmon frequency ω_P:

$$\omega_P = \sqrt{\frac{q^2 n}{\epsilon_0 m}} \tag{2.4}$$

where q is the elemental charge, m the electron mass and n the electron density. In the case of no damping with $\tau \to \infty$ and for $\omega = \omega_P$ the dielectric function $\epsilon(\omega_P)$ becomes zero and a collective longitudinal excitation mode is formed, with a purely depolarized field. These excitations are called bulk plasmons and appear in the limit of long wavelengths (low frequencies) and vanishing wavevectors k (cf. equation (2.2)). They cannot couple directly to light waves, because light is a transversal electromagnetic wave.

Matter that shows absorption properties has a complex refractive index $\overline{n} = n + i\kappa$ where n is the real part of the refractive index that indicates the phase velocity and κ is the imaginary part, called extinction coefficient, which determines the absorption. The refractive index is connected to the dielectric constant via the relation $\epsilon = \overline{n}^2$ with a real part ϵ_R and an imaginary part ϵ_I which accounts for losses (Ohmic damping) in the metal:

$$\epsilon_R = \epsilon_0 - \frac{\omega_P^2 \tau^2}{1 + \omega^2 \tau^2} \tag{2.5}$$

$$\epsilon_I = \frac{\omega_P^2 \tau}{\omega(1 + \omega^2 \tau^2)} \tag{2.6}$$

Figure 2.4A shows the experimental data of $\epsilon(\omega)$ for thin gold films that have been fitted with the resulting parameters and equations (2.5) and (2.6).[134] The Drude model shows good agreement with the experimental data for low frequencies (long wavelengths). Here, $\epsilon(\omega) < 0$, the dominant response comes from the Fermi-electrons and the material behaves metallic. For lower frequency $\omega \to 0$ the metallic screening of the external field becomes more and more perfect and the total field decreases. In the region of $1 - 2$ eV ϵ_I is small with well-defined plasmon modes. However, for higher energies interband and intraband transitions of d-band

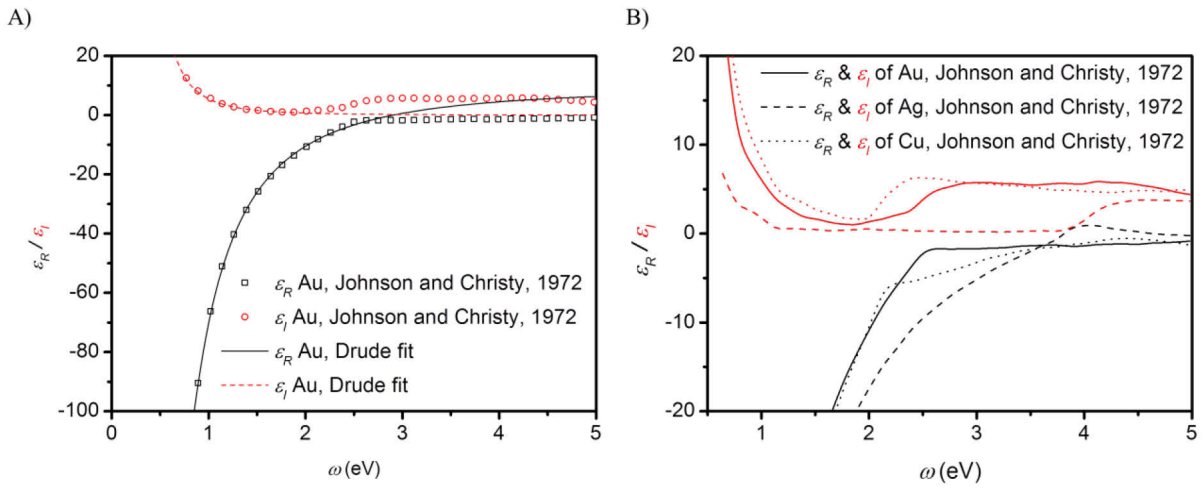

Figure 2.4: A) Empirical data of the real and imaginary parts of the dielectric constants of gold and its respective fits. B) Comparison of dielectric constants of different noble metals: gold (Au), silver (Ag) and copper (Cu).[134]

electrons occur. These transitions are not taken into account in the Drude model but contribute to the dielectric constant. This leads to a certain deviation of the actual values and a considerable increase in ϵ_I generates a substantial increase in Ohmic damping of the plasmon resonances.[47] Figure 2.4B compares the noble metals of gold, silver and copper. It can be seen that low damping (small ϵ_I) for silver appears in a considerably wider window than for other metals. Therefore, silver provides plasmon resonances with low losses throughout the NIR and most of the visible light region. Copper has only a very small window of low-loss plasmon resonances. Gold is placed in between with larger losses than silver, however, its chemical stability makes gold preferable in plasmonic applications. Additionally, differences in ϵ_R can be seen, which influences the frequencies where plasmon resonances occur. However, the dielectric values used in calculations are commonly derived from experiments.[135]

2.2.2 Surface plasmon polaritons

New plasmon modes occur when a bulk metal is terminated by a surface. These plasmon resonances propagate parallel to the interface and decay exponentially away from it into the metal and dielectric media. The charge density oscillations and the excitation fields are indivisible coupled and strongly localized to the surface. This hybridization of the material charge density waves with the electromagnetic waves is therefore called surface plasmon polariton (SPP).

For the derivation of these excitations Maxwell's equation has been solved independently for the dielectric medium and the metal. The surface is characterized by an interface with two surrounding media labelled 1 and 2 and their respective dielectric constants ϵ_1 and ϵ_2. The coordinate system is defined with z being perpendicular to the interface, which is

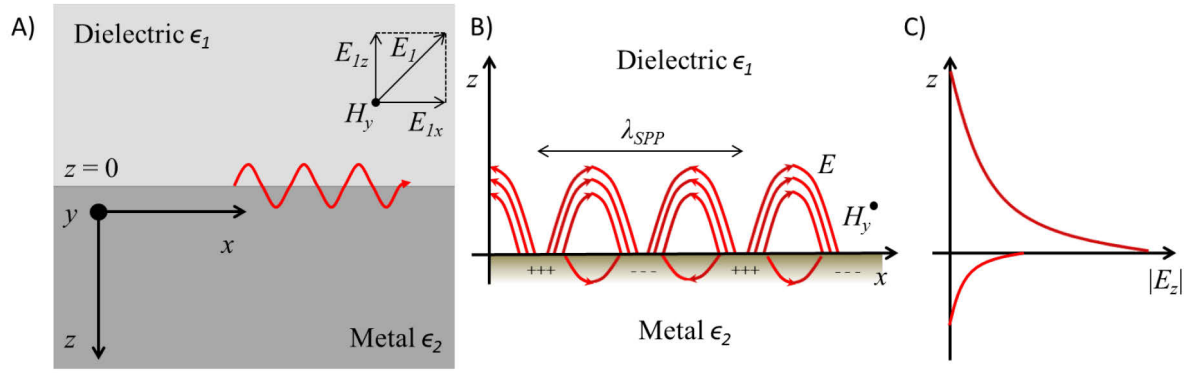

Figure 2.5: A) The left image shows the coordinate system of the interface between a dielectric and a metal. B) The middle panel illustrates the hybrid character of SPP at the interface. C) The right graph displays the evanescent electric field from the interface.[136]

located at $z = 0$, and the field propagating in the x direction (see Figure 2.5A). The phase of the field in each media must be equal at the interface with $k_{1x} = k_{2x} \equiv k_x$, with k_x being real. If k_{lz} is real the field is propagating in z direction and evanescent if k_{lz} is imaginary. For any frequency smaller than the surface plasmon frequency ω_S ($\omega \leq \omega_S$) follows that k_{1z} and k_{2z} are imaginary and the non-radiative waves are strongly localized to the interface with evanescent fields that decay away in the z directions (Figure 2.5B,C). These modes are called surface plasmons and one media must be metallic with $\epsilon_{R2} < 0$.

The wavevector k_x of the surface plasmon is always higher than the photon wavevector at all frequencies, which inhibits direct coupling of light to the surface plasmons. This mismatch in momentum can be overcome by coupling through a high refractive index prism (Figure 2.6) or grating.[11, 12, 47, 137] Here, the SPPs couple to the evanescent electromagnetic field generated upon the reflection of a light beam. In the case of prisms, for thin metal films, the Kretschmann configuration is advantageous. A metal film is directly evaporated on the prism and the SPPs generate on the opposite side of the prism via tunnelling effects. The wavevector increases in the optical dense medium and at a certain angle Θ the in-plane-component of the photon wavevector matches the SPP wavevector on an (optical less dense) air-metal surface. Under these conditions the reflectivity has a significant minimum because light can be coupled almost quantitatively to the SPPs. For thicker metal films, the tunnelling efficiency decreases. The Otto configuration can be used, where the photon tunnelling occurs at an air gap between the prism and the metal surface.

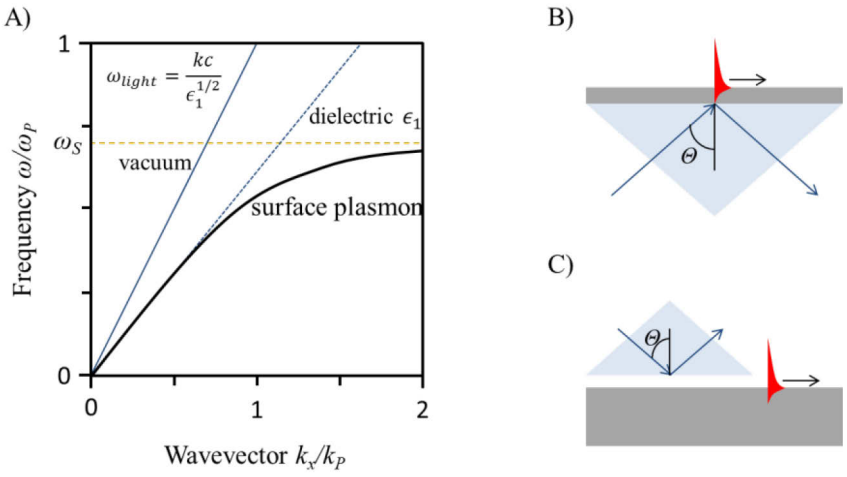

Figure 2.6: A) Dispersion relation of the surface plasmon at a metal-dielectric interface with k_P being the plasmon wavevector. B) Kretschmann and C) Otto configuration of coupling via a high refractive index prism.[137]

2.2.3 Localized surface plasmon resonances

For metal nanoparticles with diameter smaller than the incident wavelength the surface does not provide enough space for a propagating wave at the metal/dielectric interface that can be described by a wavevector *k*. Hence, plasmons in metal nanoparticles form standing waves that are strongly dependent on the nanoparticle size and shape. The lowest order mode under an external field can be described by a dipole mode. Negative charges accumulate on one side of the metal nanoparticle with positive charges on the opposite side by an applied external field (Figure 2.7). These polarized charges induce restoring forces that lead to oscillations. The restoring force depends on the amount and distribution of the accumulated charges and defines the frequency of the oscillations. Noble metal nanoparticles have a high electron density that causes strong local electric fields near the nanoparticle surfaces and support modes in the visible to NIR region which are useful for many applications.[36, 40, 138] In particular the shape has a big impact on the modes; a nanorod e.g. supports two modes with a longitudinal mode that has its poles at the tips of the nanorods and a transversal mode with a very different field distribution (Figure 2.7). It follows that these modes occur at different frequencies. All these frequencies, in principle, are discreet but are strongly broadened by the damping in the metal so that one should rather think of them as resonances. Therefore, they are more commonly called localized surface plasmon resonances (LSPR).

Spherical metal nanoparticles

To derive a simple model for the optical response of metal nanoparticles, several approximations must be made. The most important one is that the radius *a* of the metal nanoparticle is much smaller than the wavelength λ of the external driving field ($a \ll \lambda$). This quasistatic

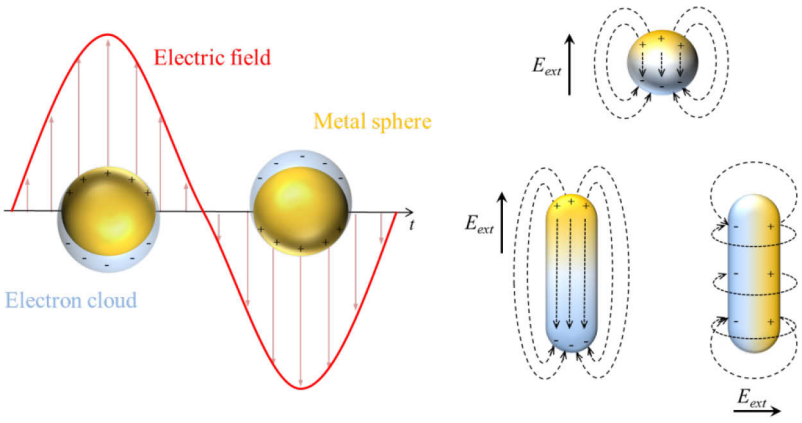

Figure 2.7: Schematic dipolar LSPR for a metal nanoparticle with oscillating free electron gas (left) and their indicated field lines (right). Nanorods provide two dipolar modes: a longitudinal (left) and transversal (right).[47]

approximation neglects the variation of the phase of the external driving field while it passes the metal nanoparticle. Hence, the external field can be seen as a constant field. Maxwell's equations can be solved for an electric potential Φ with $\mathbf{E} = -\nabla\Phi$ that is $\Phi = -Ez$ for an applied external field in z direction or $\Phi = -Er\cos\theta$ in polar coordinates. The metal nanoparticle acts like a dipole with a resonant frequency ω_1 and a dipole moment μ. The polarizability $\alpha \equiv \mu/E$ of the metal nanoparticle results from the electric potential:

$$\alpha = \frac{(\epsilon_{in} - \epsilon_{out})\epsilon_{out} a^3}{\epsilon_{in} + 2\epsilon_{out}} \tag{2.7}$$

Though an incident plane wave can only excite a single dipole mode, higher order modes do also exist. These resonances are independent from the particle size in the quasistatic approximation. However, when this approximation fails the size indeed has an influence on the modes and time-dependent solutions to Maxwell's equations are needed.

From α one can derive the absorption cross-section σ_{abs} and the scattering cross-section σ_{scat} directly. These cross-sections are defined by the rate of absorbed or scattered light divided by the incident light flux:

$$\sigma_{abs} = \frac{4\pi k}{\epsilon_{out}} \mathrm{Im}[\alpha] \tag{2.8}$$

$$\sigma_{scat} = \frac{8\pi\omega^4}{3c^4} |\alpha|^2 \tag{2.9}$$

with k as the wavevector in the medium. Insertion of equation (2.7) leads to:

$$\sigma_{abs} = 4\pi k a^3 \mathrm{Im}\left[\frac{\epsilon_{in} - \epsilon_{out}}{\epsilon_{in} + 2\epsilon_{out}}\right] \tag{2.10}$$

$$\sigma_{scat} = \frac{8}{3}\pi k^4 a^6 \left|\frac{\epsilon_{in} - \epsilon_{out}}{\epsilon_{in} + 2\epsilon_{out}}\right|^2. \tag{2.11}$$

From equation (2.10) and (2.11) three properties can be derived: (i) the cross-sections have their maximum at approximately $\epsilon_{in} = -2\epsilon_{out}$, (ii) the cross-sections vanish if $\epsilon_{in} \rightarrow \epsilon_{out}$ and (iii) the absorption scales with the volume $a^3 = V$, while the scattering scales with V^2. The reason for this different scaling is that scattering involves absorption and re-emission. Figure 2.8 shows some example spectra calculated from equations (2.10) and (2.11) with experimental values for the dielectric function of gold.[134] As mentioned in chapter 2.2.1, the dielectric function calculated by the Drude model cannot describe well enough the real values of gold

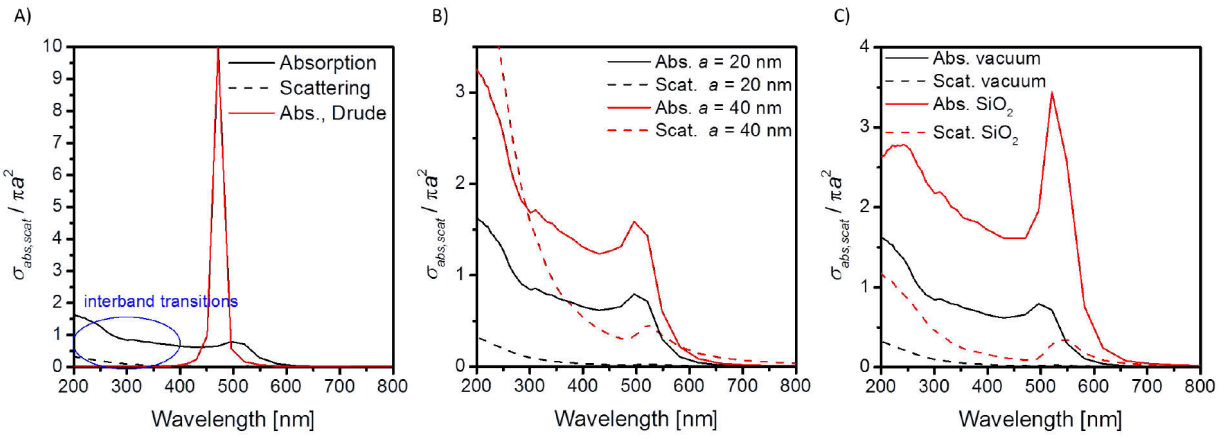

Figure 2.8: Absorption σ_{abs} and scattering σ_{scat} cross-sections of gold nanoparticles normalized to the geometric cross-section of the nanoparticle (πa^2). A) Comparison of absorption cross-section with different dielectric functions: black curve from experimental values (Johnson and Christy, 1972)[134] and red curve from the derived Drude model. B) Comparison of cross-sections with different nanoparticle radii $a = 20$ nm and $a = 40$ nm. C) Influence of a dielectric medium (silica, dielectric function from Malitson, 1965)[139].

for the high frequency region. The peak is present, but its magnitude is drastically overestimated (Figure 2.8A). The reason is the presence of d → sp interband transitions that strongly damps the LSPR, causing an increased broadening and absorptive dissipation.[140]

The scaling effect with the radius a ($\sigma_{abs} \sim V$, $\sigma_{scat} \sim V^2$) can be seen in Figure 2.8B with radii of $a = 20$ nm and $a = 40$ nm for gold. For small nanoparticles the absorption is dominant and the scattering can be neglected. However, for larger particles the scattering eventually will have a significant contribution. There is an increase in the absorption cross-section for the bigger nanoparticle; however, the increase of the scattering cross-section is far greater. Also the magnitude of absorption and scattering is interesting: For bigger nanoparticles both cross-sections become larger than their geometrical area. This is in particular true for the scattering cross-section of particles that are close to the size of $\lambda/2$ (though the quasistatic approximation becomes invalid for these regions). This is not surprising, as the normalized cross-sections ($\sigma_{abs,scat}/\pi a^2$) for absorption scales linearly with a, while the scattering scales with a^4.

The cross-sections of a gold nanoparticle in different dielectric media are shown in Figure 2.8C. The black curve is for a particle with $a = 20$ nm in vacuum ($\epsilon_{out} = 1$), while the red curve shows the same particle embedded in silica ($\epsilon_{out}(\omega) \sim 2.05 - 2.35$)[139]. A remarkable difference can be seen for these curves. Besides the magnitude of absorption/scattering the shape of the curves also varies. Such an impact of the dielectric environment has been exploited for sensors to detect local changes in the refractive index.[16, 17]

Non-spherical metal nanoparticles, e.g. a spheroid

For non-spherical systems analytical solutions are more difficult. One particle geometry that can be described more easily was introduced by Gans in 1912.[141] The surface of a spheroid can be described by a geometry factor L, which accounts for the shape and the response of a dipole and its polarizability can be written as:

$$\alpha = \frac{(\epsilon_{in} - \epsilon_{out})\epsilon_{out} abc}{3(\epsilon_{out} + L(\epsilon_{in} - \epsilon_{out}))}. \tag{2.12}$$

The polarizability becomes dependent upon the shape with L. For a metal nanoparticle, whose dielectric function is described by the Drude model without damping, α becomes:

$$\alpha = \frac{-\omega_1 abc}{\omega^2 - L\omega_P^2} \tag{2.13}$$

where ω_P is the bulk plasmon frequency and ω_1 is the resonance frequency for the dipolar mode at $\omega_P\sqrt{L}$. For a sphere $L = 1/3$ with $\omega_P\sqrt{L} = \omega_P\sqrt{3} = \omega_1$. By changing a, b or c the plasmon resonance will change. With $a = b$ a prolate spheroid forms which will become rod-like with increasing c and decreasing $L_z \rightarrow 0$. Hence, $\omega_{1,z}$ shifts to lower frequencies which can be seen as a longitudinal resonance with an applied field in z direction. The increase can be explained by reduced restoring forces between the charges at the end-sides of the rod. On the other hand, L_x and L_y increase as the rod becomes longer. This causes an increase of the frequency of the transversal resonance (Figure 2.9).[47]

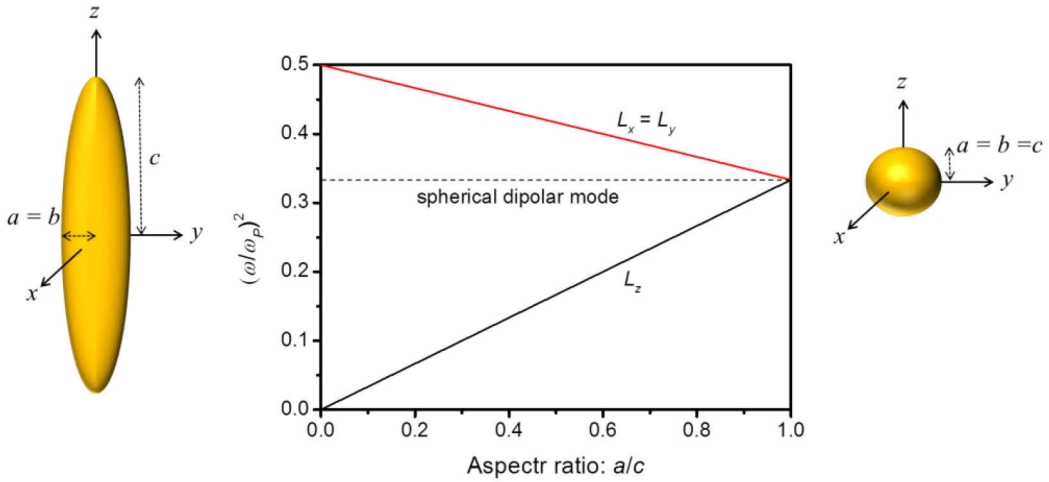

Figure 2.9: Relation between the shape and the frequency of a metal nanoparticle. A longitudinal and transversal resonance are formed for prolate spheroids according to the geometrical factor L.[47]

Similar to the equations (2.10) and (2.11) the average cross-sections for randomly oriented spheroids can be written with α_i, the polarizabilities along the three axes:

$$\sigma_{abs}^{avg} = \frac{4\pi k}{\epsilon_{out}} \mathrm{Im}\left[\frac{1}{3}\alpha_1 + \frac{1}{3}\alpha_2 + \frac{1}{3}\alpha_3\right] \tag{2.14}$$

$$\sigma_{scat}^{avg} = \frac{8\pi\omega^4}{3c^4} \mathrm{Im}\left(\frac{1}{3}|\alpha_1|^2 + \frac{1}{3}|\alpha_2|^2 + \frac{1}{3}|\alpha_3|^2\right). \tag{2.15}$$

The analytical methods that have been described before are very simple; for more complicated structures numerical methods are more accurate and computational approaches are necessary.

There has been a large amount of different numerical approaches, such as finite-difference time-domain[142, 143] and discrete dipole approximation[144, 145]. Today, many complex structures can be modelled with a high degree of accuracy which allows us to understand and predict their optical properties better.

2.3 The near-field and energy transfers near metal nanoparticles

Until now the far-field response (radiation) of metal nanoparticles has been the main focus of the discussion. The near-field response of metal nanoparticles is by no means less interesting and allows for intriguing applications. The near-field is an evanescent electromagnetic field within the nanoscale environment of the metal nanoparticle (cf. Figure 2.5C). Nanorods e.g. generate very high electric fields at the end cap sides due to the longitudinal dipolar resonances[146], which can be up to 3500-fold enhanced.[140]

A prominent example is the surface enhanced Raman scattering. At so called ”hot spots“ (the space between two metal particles with sharp tips) electromagnetic fields can be enhanced up to 10^{13}-fold, which allows for single molecule detection of the Raman signal.[15, 147] Other promising applications, which involve high electric fields or non-linear effects, are scanning near-field optical microscopy[20], photo-catalysis,[148, 149] and light-induced heat generation for controlled chemical or physical processes[48, 150] (e.g. thermal therapy in medicine[151]). In general, these effects occur due to enhanced absorption of light.[47]

2.3.1 Metal enhanced fluorescence and the Purcell effect

A well-investigated phenomenon is metal enhanced fluorescence, which is a result of enhanced absorption plus an increased radiative emission rate due to the Purcell effect.[152] The Purcell effect describes the enhanced spontaneous emission rate of an emitter by the Purcell factor $F_P = \Gamma_r^{cav}/\Gamma_r^{em}$, i.e. by the decay rate of the radiative emission near a cavity (a metal

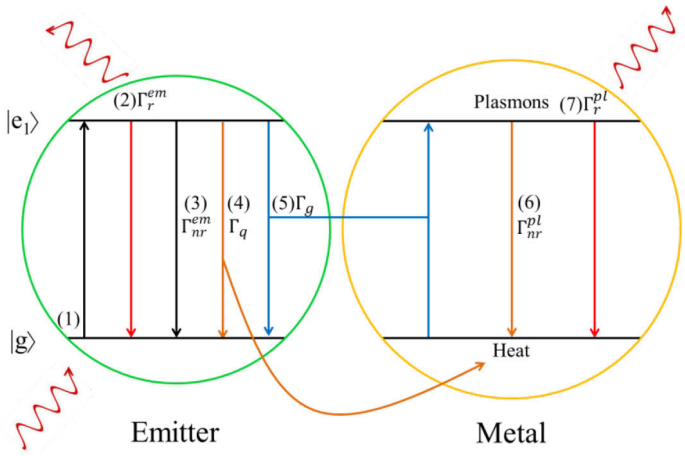

Figure 2.10: *Simplified* energy diagram with decay processes after (1) excitation of the emitter from the ground state to the excited state. (2) Radiative emission of the emitter. (3) Non-radiative emission of the emitter. (4) Quenching by the metal. (5) Non-radiative energy transfer with excited plasmons in the metal. (6) Non-radiative decay of plasmons and (7) radiative decay of the plasmons.

nanoparticle mode) Γ_r^{cav} compared to the emission rate in the free space Γ_r^{em} of the emitter. The remaining decay rates of the dye molecules (free emission Γ_r^{em} and non-radiative emission Γ_{nr}^{em}, Figure 2.10) are largely unaffected by the presence of a metal nanoparticle. With a metal nanoparticle in close vicinity other decay channels occur (Figure 2.10): (i) quenching by non-plasmonic excitations that result in heat Γ_q or (ii) non-radiative energy transfer that excites plasmons (Γ_g), which will then generate heat by non-radiative processes (Γ_{nr}^{pl}) or produce far-field radiation (Γ_r^{pl}).

The decay rates of non-radiative processes are several magnitudes of order faster than the decay rates of the radiative emission of the emitter, and hence occur almost quantitatively.[153] Even faster are the plasmonic decay rates Γ_{nr}^{pl} and Γ_r^{pl}, and their ratio depends on the dielectric function of the metal and the resonance frequency. In general, the radiative decay process becomes more prominent for larger particles.[47] The non-radiative decay rate commonly dominates for small particles. Furthermore, it must be kept in mind that multiple modes (cavities) with individual decay rates may be excited as well. Additionally, not shown in Figure 2.10, plasmons can excite an acceptor by non-radiative energy transfers, which is just the opposite of (5) (Γ_g) in Figure 2.10. The Purcell factor is dependent of the cavity and can be written as $F_P \sim Q/v_m$. The quality factor Q is proportional to the lifetime of a photon in the cavity and given by $\omega\tau$, with ω being the resonant frequency of the cavity and τ the decay time (cf. equation (2.3)). Though the quality factor Q of the different modes in metal nanoparticles are only moderate (10 – 100), the mode volumes v_m can be very small which allows for high Purcell factors.[48] At properly tuned conditions simple spherical gold

nanoparticles have achieved metal enhanced fluorescence factors of 10 or more.[23, 48, 154] For highly confined electromagnetic fields, e.g. at a gold bowtie antenna, even enhancement factors of 1340 have been achieved.[155]

All these interactions are greatly distant dependent due to the evanescent nature of the electric near-field.[23, 24, 147] Metal enhanced fluorescence shows reduced radiative decay rates of the fluorophore compared to the free fluorophore in the range of 0 – 20 nm from the metal surface. Additionally, the confined electric field enhances the absorption of light by the fluorophore (0 – 15 nm). However, the vicinity to a metal surface does not necessarily lead to higher intensities; at low distances (0 – 5 nm) quenching of the fluorescence occurs. These effects appear through coupling of the emitter and the metal nanoparticle, which excites certain modes that undergo damping and create eventually electron-hole pairs. Additionally, charge-transfer effects can occur at very small distances between emitter and metal, which results in total loss of the energy.[47] These non-plasmonic effects are mostly undesired for applications.

2.3.2 Surface plasmon amplification by stimulated emission of radiation

The principle of surface plasmon amplification by stimulated emission of radiation (spaser) was first proposed by Bergman and Stockman in 2003.[30] The literal similarity to the laser is not at random: The photons in a laser are replaced by surface plasmons in a spaser, while the resonant cavity is replaced by a metal nanoparticle that supports the surface plasmons. These surface plasmons are generated by an active gain medium, e.g. a semiconductor or molecules. The gain medium must be excited externally via strong electric or optical pumping and population inversion of the ground to excited states is achieved. Then, plasmonic oscillations in the metal nanoparticle stimulate the emission, which in turn generates more surface plasmons, stronger fields and eventually supplies the positive feedback for the spaser action. For effective energy transfers in this coupled system it is important that the gain medium spatially and spectrally overlaps with the metal nanoparticle. Stockman explained the similarity of spasers to lasers as:[156]

> *"The reason that SPs in a spaser can work analogously to photons in a laser is because their relevant physical properties are the same. First, SPs are bosons: they are vector excitations and have spin 1, just as photons do. Second, SPs are electrically neutral excitations. And third, SPs are the most collective material oscillations known in nature, which implies they are the most harmonic (that is, they interact very weakly with one another). As such SPs can undergo stimulated*

emission, accumulating in a single mode in large numbers, which is the physical foundation of both the laser and the spaser.“

The promises of such a coupled system are the miniaturization of a coherent light source and the high decay rates in the metal that would allow for ultrafast switching ($\Gamma_{nr}^{pl} = 1/\tau \sim 10 - 100$ fs). As discussed in the sections before, metal nanoparticles confine light into much smaller dimensions. For conventional lasers the diffraction limit holds true, which restricts the length L of a Fabry-Pérot cavity to $\lambda/2$. This limit can be overcome by using metal nanoparticles that can be as small as a few nanometres. The strong coupling of the gain medium to the metal nanoparticle means that the needed operational power could be very small. These properties would allow for an integration in nanoscopic structures with a spaser being a switch or even amplifier.[45, 157] Nevertheless, strong inherent losses in the metal need to be overcome. These losses can be mitigated by high gain, i.e. a high amount of emitter with efficient coupling or stronger pumping, and improvement of the metal (Q and ν_m, which is equivalent to the Purcell factor F_P).

As mentioned earlier, the losses in metal nanoparticles are high, especially for gold due to intraband transitions. Silver, being the better metal with lower losses, is easily oxidized under wet chemical synthesis, and hence often avoided. Losses in metal nanoparticles can be evaluated by the quality factor Q. For small decay rates ($\Gamma^{pl} \ll \omega$), Q can be written as:

$$Q = \omega\tau = \frac{\omega}{2\Gamma^{pl}} \tag{2.16}$$

Another definition for Q is often used as well:

$$Q = \frac{-\mathrm{Re}\varepsilon(\omega)}{\mathrm{Im}2\varepsilon(\omega)} \tag{2.17}$$

The Q-factors derived from these equations agree well for the red to infrared light where the Drude model can describe the dielectric function of the metal best. However, due to intraband transitions the Q-factor decreases drastically in the yellow – blue region of the visible light.[158] One way to improve the Q-factor for gold nanoparticles is to go to LSPR energies well below where intraband transitions occur. This can be e.g. achieved by using gold nanorods instead of spherical particles. Theory predicts Q-factors of ~40 for gold nanorods with a longitudinal LSPR at ~800 nm (vs. $Q \sim 10$ for nanospheres at 530 nm). Such an increase of Q results in approximately one order of magnitude less gain threshold.[159]

Due to the asymmetric shape, nanorod-based systems would be wavelength tuneable and, with a stable polarization along the longitudinal axis, polarization sensitive as well. This

is indeed yet another concern to keep in mind: any *l*-multipole mode of a spherical particle is 2*l*+1 degenerated. For the dipolar mode this means that the mode has three concurring polarizations making the spasing mode unstable. In reality, one polarization may be favoured eventually due to non-perfect symmetry of synthesized nanoparticles. Due to increasing feedback from one favoured polarization spasing can be induced.[158]

Not only various polarizations occur, but also several modes may be excited at a given spectral range. This competitive excitation is decreasing the likeliness of getting a positive spaser feedback and should be avoided. Though the dipolar mode is the most prominent mode for small metal nanoparticles, higher order modes could be advantageous due to higher *Q*-factors that occur for larger nanoparticles. However, larger nanoparticles suffer from radiative losses which cannot be neglected anymore. This can be circumvented by so called dark modes that have very low losses. These are difficult to excite from the far-field and not very prominent in the optical spectra (therefore called "dark"), however, can be stimulated within the near-field by excited emitters.[30, 160, 161]

Of particular interest is the gain medium as well. For quasistatic calculations, the emitter/gain is described by dipoles that are excited by an external field. A two level system is assumed with the dipoles being excited to a higher energetic state $|e_2\rangle$ that relaxes stimulated by plasmons to the ground state $|e_1\rangle$. Via non-radiative energy transfer to the metal nanoparticle new surface plasmons are generated. A spasing condition was derived by Stockman which includes the characteristics of the metal and the emitter/gain medium[157]:

$$\frac{d_{12}^2 Q N_c}{\hbar \Gamma_{12} \nu_m} \geq 1 \tag{2.18}$$

From equation (2.18) several conditions for spasing can be derived: (i) a high transition dipole moment d_{12} of the emitter, (ii) a large amount of emitters N_c, (iii) narrow spectral width of the emitter fluorescence (small polarization relaxation Γ_{12}) and (iv) good mode properties of the metal Q/ν_m are advantageous to achieve spasing.

The spasing condition in equation (2.18) coincidences with the loss-compensation of the metal derived by Stockman. For silver nanoparticles he calculated a necessary density for a full loss-compensation of $\rho = 2.9 \cdot 10^{19}$ cm^{-3} chromophores of randomly oriented dye molecules.[158] As gold exhibits higher losses, higher gain is needed, i.e. $\rho = 2.0 \cdot 10^{20}$ cm^{-3} chromophores. For semiconductor quantum dots (QDs) this concentration is impracticable and even highly concentrated samples could not provide full loss-compensation.[162] This involves usually larger structures that provide SPP. SPP amplification involving dye molecules was reported by several groups, however, no spasing signature was seen but rather

amplified spontaneous emission (ASE).[161, 163-167] The gain calculated for molecules ($g = \rho \cdot \sigma_{abs}$) at such high concentrations reaches quickly values > 1,000 cm^{-1}. Such gain values are realistic for semiconductor materials but impose high limitations for organic gain,[45, 49] e.g. self-quenching of dye molecules, energy transfers between the emitters or reduced quantum efficiencies and lifetimes. High dye concentrations can as well complicate the propagation of the pump energy to reach the metal surface. The high pump power needed also has to be taken into account, as damage to the metal or dye molecules can be induced.[49] These effects have not been considered by the theory, as it is hard to model. Some of these aspects will be discussed in the chapter 4.3.1.

2.4 Light trapping in thin-film solar cells

Light trapping enhances the effective path length through the absorber, and hence increases the efficiency of solar cells. For conventional thick solar cells light trapping was achieved by structuring the surface, using features of a few microns in size (ray tracing).[28] The limit of such light-trapping was shown to be an enhanced absorption by a factor of $4n^2$ (with n, the refractive index).[168] This is due to the high density of optical modes in e.g. silicon compared to air. The theory assumes equal distribution of light in the modes, and is therefore more likely scattered back within the silicon leading to an increased effective path length through the absorber.[28]

However, such structuring features are too large for thin-film solar cells which have an absorber thickness below one micron. Plasmonic solar cells have shown to be able to trap

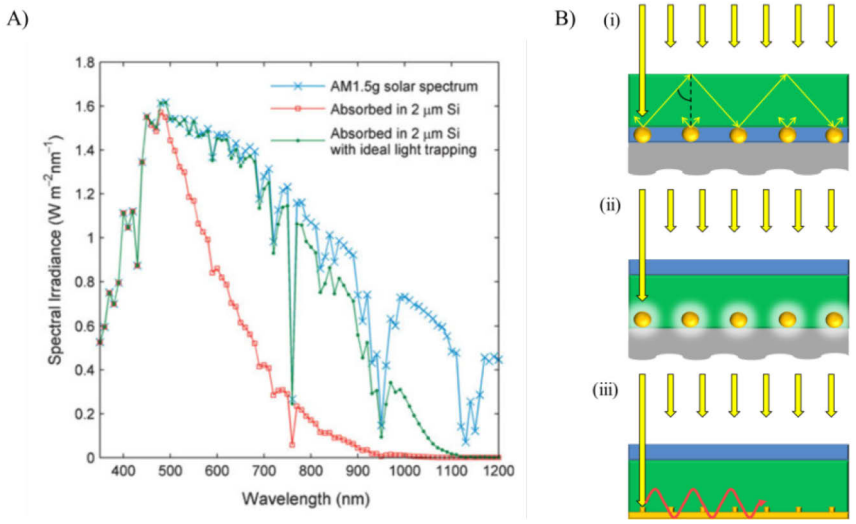

Figure 2.11: A) AM 1.5g solar spectrum and absorbed light by a 2 µm thick crystalline silicon film with and without light-trapping. (Reprinted from Ref. [28], copyright (2011) Cambridge University Press.) B) Light-trapping mechanisms: (i) light scattering, (ii) light confinement and enhanced absorption and (iii) SPP generation.

light and increase the solar cell performances by integration of metal nanostructures (Figure 2.11). Such plasmonic structures can induce light trapping via three different mechanisms: (i) light scattering at the metal nanoparticle, (ii) light confinement (LSPR) and (iii) light trapping via SPP generation (Figure 2.11). Thin-film solar cells that overcome the low absorption via longer path lengths through the absorber not only save costs compared to conventional thick solar cells. Reduction of the cell thickness decreases the dark current (I_{dark}), which is determined by the recombination rate in the solar cell. A decrease of I_{dark} leads to an increase of the open-circuit voltage (V_{oc}), the maximum voltage available from a solar cell, as $V_{oc} \sim \ln(I_{photo}/I_{dark})$. Here, I_{photo} is the photocurrent, but the open circuit voltage V_{oc} is much more reliant on I_{dark}, as it can vary many magnitudes of order. Therefore, the cell efficiency rises exponentially by decreasing the surface recombination rate, which is affected by the cell thickness. Furthermore, carrier recombination is reduced by shorter distances for carriers to be collected at the junction. This leads to a higher carrier density and higher photocurrent.[27] Other benefits are practical issues, e.g. do thin-film solar cells allow for flexible and more light-weight solar cells that can open new fields of applications.

2.4.1 Light scattering of plasmonic nanoparticles

Stuart and Hall have been the first to recognize that metal island films can enhance the absorption in silicon significantly.[169, 170] The enhancement originates from scattered light at the nanoparticles which will increase the effective path length in the absorber. For a homogenous medium, e.g. air, the scattered light will be symmetric in the forward and backward direction. This changes when the metal nanoparticle is in the vicinity of a dielectric with a higher dielectric constant (e.g. silica): light gets scattered preferentially into the absorber.[171, 172] Hence, the light will experience a longer path way through the absorber and has a high possibility to be reflected at the outer dielectric/absorber interface beyond a critical angle (16° for air/silica). If a reflective metal back-contact is present the light can be trapped efficiently. It then passes several times through the absorber, increasing the effective path length by a factor of several times larger than the real absorber thickness.

Consequently, scattering of light is desired while parasitic absorption should be avoided. Such absorption leads to Ohmic damping in the metal nanoparticle and the energy cannot be converted to form electron-hole pairs. In chapter 2.2.3 the scattering properties of metal nanoparticles have been discussed: larger nanoparticles scatter light much stronger than they absorb the light. As an example, a 150 nm silver particle has an albedo (fraction of light scattered to the far-field) of 95%. It was also shown that the scattering cross-section is several

times larger than the geometric area of the metal nanoparticle. Therefore, a 10% coverage of the substrate is sufficient to capture most of the incident light.[27] From Figure 2.11 it can be recognized that predominantly visible light is absorbed in thin-film solar cells. It would be beneficial if the light in the NIR region is scattered, where the solar cell absorbs the light less efficiently. Gold and silver metal nanoparticles, however, have plasmon resonances mainly in the visible region. Chapter 2.2.3 showed the effects of size, shape and dielectric environment on the LSPR of metal nanoparticles. This opens ways to red-shift the LSPR to the desired wavelength region to improve the solar cell performance. In particular the refractive index is a key figure here. By partially embedding the metal nanoparticles in high refractive index materials the LSPR can be shifted over a wide spectral range. Insulator materials are beneficial, as they prevent shunting or surface recombination due to the metal presence.

There are different fabrication methods to integrate metal nanoparticles into photonic structures. Probably the most common one is the annealing of thin metallic films that have been evaporated firstly onto the substrate.[169, 173, 174] This process is called dewetting and describes the rupture of thin films on the substrate to produce droplets. It is the opposite process of spreading and leads to the formation of a dense array of metal nanoparticles. Compared to other physical top-down methods, like nanolithography[175, 176] or metal deposition on an anodic aluminium mask[177], dewetting is simple and cheap. However, particle size distribution, array positions and surface coverage are difficult to control. Another method to integrate metal nanoparticles is the deposition of preformed colloidal metal nanoparticles. In chapter 2.1.1 it was discussed that wet colloidal chemistry has advanced tremendously in the past years and nowadays diverse possibilities of shapes and metals exist to match the needs for optical applications like plasmonic solar cells. Precise control over the morphology allows for the sensible tuning of the optical properties, which includes their scattering behaviour. Besides that, the approach separates the particle preparation from the distribution on the substrate. This allows for a very cheap approach and controlled tuning of the morphology *and* surface coverage. However, only a few groups have published reports of plasmonic solar cells by using colloidal metal nanoparticles.[178-182] Gold nanoparticles have been used in majority, again, due to their higher stability. Indeed, application of silver particles and their possible oxidation is an issue that needs to be addressed,[183] as will be shown in chapter 5.1.[59]

2.4.2 Light confinement using localized surface plasmon resonances

The high electric fields generated by metal nanoparticles, which strongly interact with the surrounding matter, can be used as well for photovoltaics. In chapter 2.3.1 it was explained that metal nanoparticles act as antenna and confine the incident light into small spots. This leads to an increased absorption in the absorber material. This works well in particular for small metal nanoparticles with a low albedo. The principle is very useful for absorber materials that have short carrier diffusion lengths, and hence, must be placed close to the collection junction area.[27]

Of great importance is an efficient energy transfer to the absorber material and minimization of the Ohmic losses in the metal. This can be achieved by using organic or direct-bandgap semiconductor absorbers that have an absorption rate larger than the plasmon decay rate. Increased efficiencies by using small metal nanoparticles has been shown for ultrathin-film organic solar cells,[184] dye-sensitized solar cells[185, 186] and inorganic CdSe/Si heterostructures.[187]

2.4.3 Light trapping via surface plasmon polariton generation

A third method of light trapping is to use SPP that can propagate, in particular in the NIR and IR region, very far with low losses (from 10 – 100 μm).[188] As seen in Figure 2.11, there is no, or very limited absorption in this region for thin-film solar cells. SPPs can be generated by structuring the metal surfaces, e.g. with gratings[189, 190] or by using a Kretschmann configuration.[191] The SPPs then propagate perpendicular to the incident light along the metal surface and the effective path length is increased many magnitudes of order. Due to the evanescent nature of SPPs the absorber thickness is allowed to be thin and the plasmonic coupling concept can be integrated in a natural way, as metal contacts are one standard element in solar cells.

For an effective light harvesting mechanism the absorption of SPPs must be stronger in the semiconductor than in the metal. Theoretical calculations have shown that the Si/Ag interface increases the absorption above 800 nm, but is still dominated by losses in the silver film in the visible and NIR region. However, for the same arrangement of a GaAs/Ag interface the absorbed light fraction in the semiconductor is high for the entire region between the SPP resonance (600 nm) and GaAs bandgap (870 nm).[27] Several reports on enhanced thin-film solar cell efficiencies based on SPP geometries have been published as well.[189-192]

3. Effects of size, shape and dielectric environment

3.1 Size effect on localized surface plasmon resonances of spherical gold nanoparticles

From the previous chapter 2.2.3 it became obvious that shape and the dielectric environment can have a drastic impact on the LSPR. The size has no effect on the position of the LSPR in the simple model described. Yet, experimental results show that the dipolar mode is indeed size-dependent. For small nanoparticles in the quasistatic approximation, the electron-surface scattering becomes important as the mean free path of the Fermi-electrons (tens of nanometres) is limited by the particle boundaries. Therefore, the damping coefficient τ of the dielectric constant $\epsilon(\omega)$ (equation (3.1)) becomes size dependent which alters the dielectric function of the metal[193]:

$$\tau(a) = \tau_0 + \frac{C v_F}{a} \tag{3.1}$$

where τ_0 is the bulk damping constant, v_F is the electron velocity at the Fermi-energy and C is a theory dependent parameter which introduces specifics of the scattering process.[194] Hence, the damping becomes smaller for larger particles which in turn leads to a reduced half-width of the LSPR peak.[193]

Until now only particles in the quasistatic limit have been considered. *Larger* particles can sustain higher order modes besides the dipolar mode. Such higher order modes exhibit

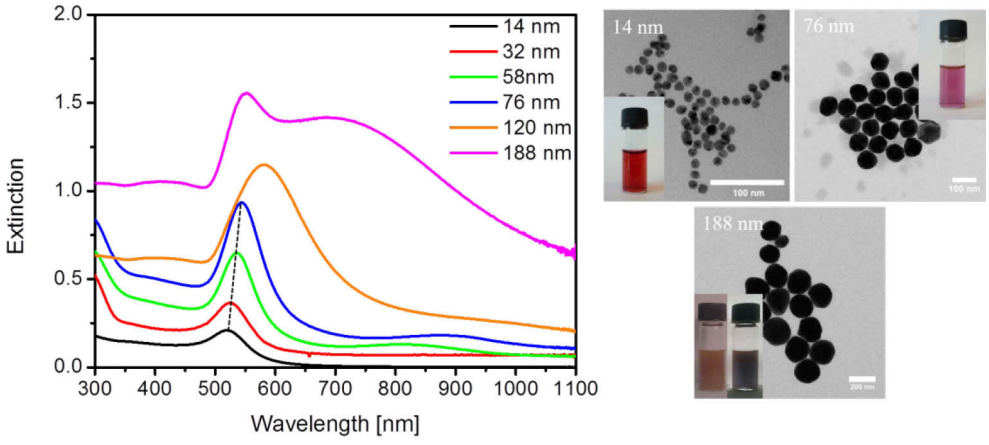

Figure 3.1: Extinction spectra of different sized gold colloid solutions. Some exemplary transmission electron microscopy images are shown on the right. Smaller gold nanoparticles are dominated by absorption of the dipole mode. Higher order modes appear for the 120 nm and 188 nm gold samples where scattering becomes more and more important.

LSPRs at higher frequencies, which cause a broadening of the extinction spectra.[146, 195] Furthermore, the polarization of the metal nanoparticle becomes inhomogeneous due to the large size of the nanoparticle compared to the incident wavelength of the external electromagnetic field. The broadening of the LSPR is then ascribed to retardation effects.[194]

An example for the size effect is given in Figure 3.1: spherical gold nanoparticles with diameter of 14 nm have been synthesized via the Turkevich method.[65] These gold nanoparticles have been dispersed in CTAB and subsequently grown larger up to the size of 188 nm via the mild reduction of the gold precursor $HAuCl_4$ with ascorbic acid.[196] This mild reducing agent reduces the Au(III) to Au(I) and prevents new gold nucleation. Consequently, the gold nanoparticles grow accordingly to the ratio of added gold precursor and gold seeds. Gold nanoparticles from 14 → 58 nm show a dipole mode that is shifted slightly to higher wavelengths and simultaneously becomes sharper due to lower electron-surface scattering. For larger nanoparticles higher modes appear which leads to a distinct broadening of the extinction spectra. The largest nanoparticles show a very broad dipole mode because of retardation effects. Furthermore, the nanoparticles shows strong scattering, which colours the solution orange when illuminated from the side. When illuminated from the back, the solution shows absorption colouring the solution blue (Figure 3.1 for 188 nm gold nanoparticles).

3.2 Effect of shape and aspect ratio of gold nanorods on the localized surface plasmon resonances

Different nanoparticle shapes can induce new LSPR modes with different optical properties as has been shown e.g. for cages[197], triangles[198], octahedral[199], decahedral[200] etc. Figure 3.2 shows the extinction spectra of 65 nm silver nanocubes and 50 nm silver nanospheres. The spectrum of the silver nanocubes shows clearly new LSPR features due to the shape

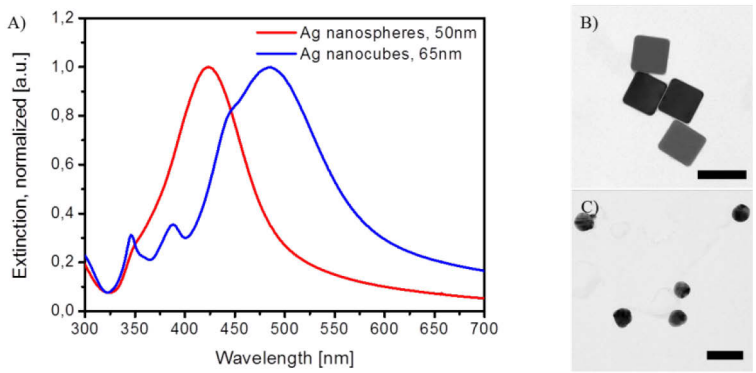

Figure 3.2: A) Extinction spectra of 65 nm silver nanocubes (B) and 50 nm silver nanospheres (C). The nanocube spectrum exhibits new LSPR in the blue and UV region. The scale bar in B and C represents 100 nm.

anisotropy, while the spherical nanoparticle exhibits only the isotropic dipolar LSPR peak and a quadrupolar mode as a shoulder at higher energies.

A prime example for the influence of shape are gold nanorods. Similarly to an ellipsoid, though nanorods are modelled more realistic by a cylinder with two hemispheres (cf. chapter 2.2.3), nanorods exhibit a longitudinal and transversal LSPR. The transversal LSPR of the gold nanorod is mostly independent of the aspect ratio and located at around $\lambda = 520$ nm. On the other hand, the longitudinal LSPR greatly responds to the aspect ratio. This can be understood quite intuitively when looking at the electric field lines of these two different dipole modes of the nanorod (cf. Figure 2.7 in chapter 2.2.3). As a result, the longitudinal LSPR shifts to lower wavelengths for smaller aspect ratios due to stronger restoring forces between the end cap sides. Figure 3.3 shows gold nanorods that have been oxidized slowly in an acidic hydrogen peroxide solution from the end cap sides. This results in shorter nanorods with a lower aspect ratio (3.9 → 1.6). As seen in Figure 3.3, the longitudinal LSPR is very sensitive to the oxidation process and changes significantly over time from 774 nm to 605 nm. The oxidation process can be well controlled, which makes the longitudinal LSPR individually adjustable. This LSPR tuning ability makes gold nanorods desirable for plasmonic applications. Furthermore, the longitudinal LSPR can be found at lower energies than the interband transitions in gold, which results in higher Q-factors.[159, 201] The half-width of the longitudinal peak also gives interesting information about the polydispersity; a narrow peak indicates a more monodisperse system.

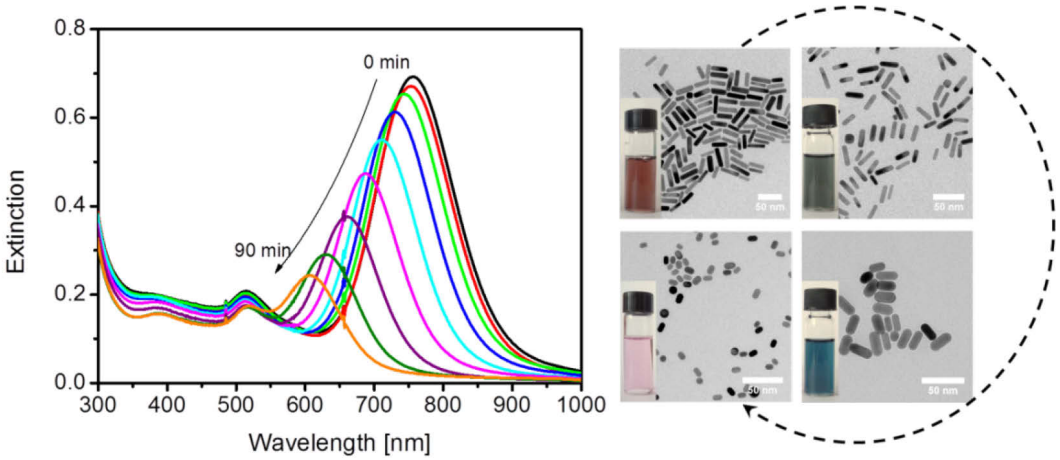

Figure 3.3: Extinction spectra of oxidized gold nanorods over time. The nanorods become shorter from their end cap sides, which leads to a blue shift of the longitudinal LSPR. On the right side are some exemplary transmission electron microscopy images. Due to the altered optical properties the colour of the colloidal solution changes as well.

3.3 Effect of the dielectric environment on the localized surface plasmon resonances

The effect of the dielectric environment can be also seen for gold nanorods, i.e. the longitudinal LSPR reacts very sensitive to its ambiance. Figure 3.4 shows gold nanorods that have been coated with a protective PNIPA shell and its temperature-dependent size was measured by dynamic light scattering. In chapter 2.1.2 the thermosensitive behaviour of PNIPA was explained. Here, the shell shrinks by approximately 15 nm. When the shell shrinks, the water is expelled from the microgel network and the refractive index is increased due to the higher density of polymer chains. This affects the dielectric environment closely to the gold nanorod surface directly via $\epsilon = \overline{n}^2$ and causes a red-shift and absorption-decrease of the longitudinal LSPR with increasing temperature. At the same time, the transversal dipole mode has increased absorption intensity with higher temperatures (Figure 3.4).

The effect of the dielectric change around a metal nanoparticle must be taken into account in particular for metal nanoparticles placed into high refractive index materials, e.g. silicon for plasmonic solar cells. The active LSPR that is desired for the plasmonic application can be red-shifted by many tens of nm this way.[202, 203] Therefore, even small changes in the refractive index, e.g. the PNIPA microgel collapse in Figure 3.4C or a silica coated shell (cf. chapter 4.1), can be measured sensitively. Naturally this effect has been exploited for refractive index sensing[16, 17].

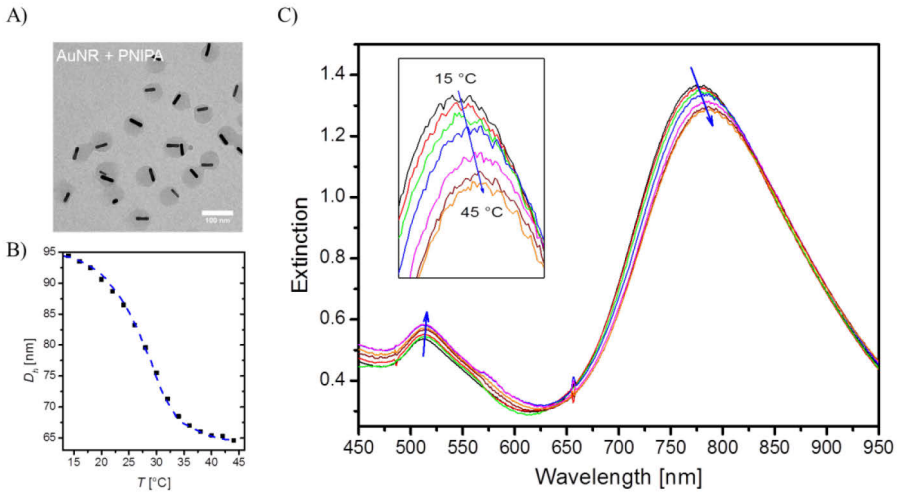

Figure 3.4: A) Transmission electron microscope image of gold nanorods with a thermosensitive PNIPA shell. B) Hydrodynamic radius measured by dynamic light scattering decreases with increasing temperature. C) LSPR shifts of the gold nanorods due to the changes in the refractive index near the particle surface.

4. Synthesis and investigation of nanoscopic hybrid systems to achieve spasing

The aim of this project was to fabricate the smallest system capable of providing coherent amplification of radiation. This shall be realized by spasing of nanoscopic hybrid structures based on the results of Noginov *et al.*[31] In his work, 14 nm gold nanoparticles have been synthesized and coated with a 15 nm silica shell. The silica shell was doped with approximately 2,700 Oregon Green 488 (OG-488) dye-molecules per gold nanoparticle. These structures have been subject to 5-ns pulses pumped at λ_{ex} = 488 nm in a 2 mm path length cuvette. At high pump-powers the spontaneous emission spectra changed to a narrow emission line at λ_{em} = 531 nm that was associated with spasing.

Firstly it was tried to verify these results. Secondly, single particles have been investigated to unambiguously prove that individual particles show spasing signature. However, none of these systems showed spasing features, even after the improvements of the synthesis or the setup used to optically pump the hybrid structures. Hence, we used other approaches based on layer-by-layer techniques or thin-film systems, i.e. gold nanoparticles embedded in a dye-polymer-matrix.

The hybrid dye-gold nanoparticles systems have been optically excited by one of two lasers. A Titanium-Sapphire (Ti:sapphire) laser that generates frequency-doubled laser light at around 485 nm in continuous wave mode or with a ~80 fs pulse at 80 MHz (cf. 8.3.4 and Figure 8.3) was used for all hybrid spherical gold nanoparticles with OG-488 molecules with up to 750 µW power. For other dye molecules a pulsed diode laser has been used that emits laser light at 532 nm with a ~100 fs pulse at 80 MHz and a power up to 450µW.

Moreover, a Neodyn YAG (Nd:YAG) laser was used with 25 ps pulses at 532 nm with very high pulse energies of up to 1 mJ/pulse. The repetition rate was extremely slow (1 – 50 Hz) to avoid fast bleaching and unrelaxed excited states before the new laser pulse hits the sample. These experiments have been conducted by Günter Kewes from Humboldt University Berlin.[204]

4.1 Approach and synthesis of active hybrid nanosystems

4.1.1 Gold-silica core-shell nanospheres with dye doped silica shells

Gold nanoparticles have been synthesized by the Turkevich method, which is the most common way to produce monodisperse gold nanoparticles in the size region of 8 – 20 nm.[65-67]

The citrate concentration has been adjusted to synthesize an average size of 14 nm gold nanoparticles. The surface of the gold cores has been modified by the organosilane (3-aminopropyl)triethoxysilane (APTES) that provides a primary amine and adsorbs on the surface. The remaining three ethoxy groups undergo hydrolyzation and condensation and form a thin silica shell around the gold core after adding additional sodium metasilicate by carefully controlling the pH.[97] The silica shell was then grown by a modified Stöber process[98] using another organosilane, tetraethoxysilane (TEOS), which undergoes the same reaction mechanism as APTES (Figure 2.2, chapter 2.1.2).[100] Hence, a small portion of APTES molecules can undergo co-condensation during the formation of the silica shell. The amine group in APTES can be used to covalently bind amine-reactive dye molecules with active groups like isothiocyanate (ITC) or *N*-hydroxysuccinimide esters (NHS). There is a broad range of commercially available amine-reactive dye molecules.

For efficient energy transfers the spatial and spectral overlap is of high importance. Spatial confinement of the dye molecules is given by the co-condensation of the APTES-dye conjugates in the silica shell. The spectral overlap depends mainly on the synthesized gold nanoparticle. The as-synthesized 14 nm gold nanospheres exhibit a LSPR at roughly 524 nm. After the silica coating the LSPR peak shifts to 528 nm due to the change of the dielectric environment (cf. chapter 3.3). A bright molecule with emission in this spectral range is fluorescein. Its fluorinated derivative is OG-488 and slightly more photo-stable. ITC modified OG-488 molecules have been covalently linked to APTES (Figure 4.1) and added to the Stöber solution. Two different samples have been prepared this way. One sample followed the work of Noginov *et al*. with a silica shell thickness of 26 nm (referred as AuNS-OG488-N). A second sample had a 7 nm emitter free silica shell around the nanoparticle, which acts as a spacer layer between the dye molecules and the gold core. Thereafter a 13 nm dye doped silica shell was grown. This sample was labelled as AuNS-OG488-S. As mentioned in chapter 2.3.1, undesired quenching processes occur at very close distances between the metal and the

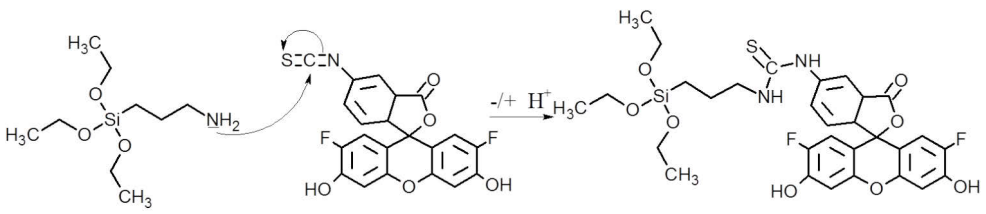

Figure 4.1: Reaction mechanism of OG-488-ITC and APTES to covalently link the dye to the organosilane. The compound can be co-condensated with TEOS and gets permanently embedded in the silica shell around the gold nanoparticle.

dye molecules that lead to direct losses. Theoretical calculations by Günter Kewes have shown that introduction of an emitter free spacer layer leads to a significant reduction of threshold pump-power by 3 orders of magnitude.[205] On the other hand, the minimum gain needed is increased by a factor of 5. Nonetheless, other effects like bleaching of molecules and heat generation can be reduced by using lower pump-powers.

Figure 4.2 shows combined UV/Vis absorption and fluorescence spectra of both samples with their respective TEM images. The black curve in the UV/Vis spectra shows the dipolar LSPR of spherical gold nanoparticles with a thin silica shell. The emission of OG-488 (orange curve) overlaps spectrally with the absorption of the gold nanospheres. The excitation spectrum of the APTES-OG-488 conjugate (blue curve) is shown as well with a peak maximum at 500 nm in ethanol. The absorption peak of the hybrid nanostructure AuNS-OG488-S is more broadened due to higher amount of OG-488 that was embedded in the silica shell.

The amount of dye molecules in the silica shell has been calculated by the difference of fluorescence intensity of dye molecules added to the Stöber solution and the supernatant after particle separation from the reaction mixture. The amount of gold particles was estimated under the assumption of complete reaction of the gold precursor to gold nanoparticles ($N_{NP} = c_{Au}V_{Au}M_{Au} / \rho_{Au}V_{NP}$). The resulting dye concentration per nanoparticle varied significantly between a few hundred to 2,000 emitters. Several aspects that influenced the amount of dye molecules have been identified, i.e. reactivity of the ITC group, purity of APTES and the solvent (DMSO) for covalently linking the dye to APTES and finally the reaction conditions during the co-condensation in the Stöber solution.

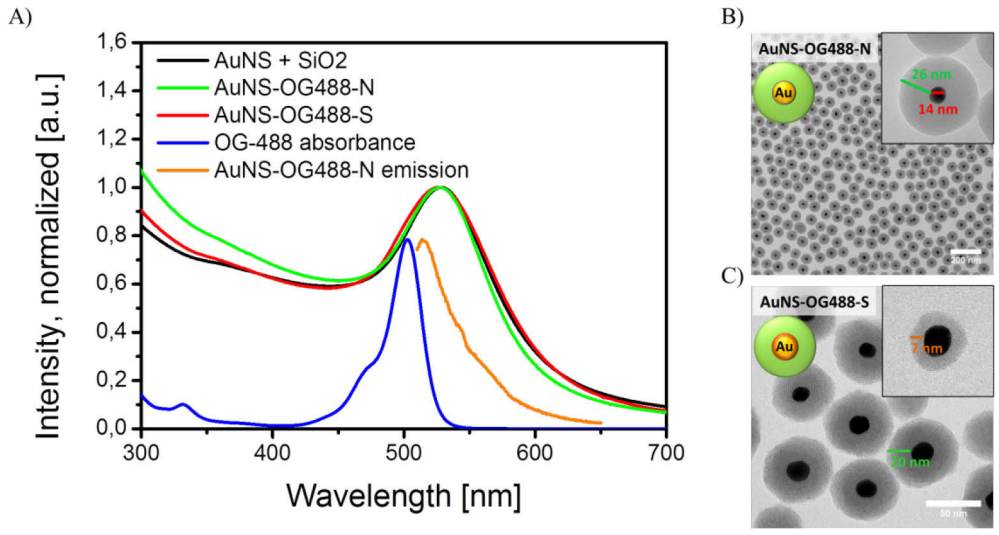

Figure 4.2: A) UV/Vis absorption spectra and fluorescence of hybrid gold nanospheres with OG-488 molecules embedded in a silica shell. B) TEM images of gold nanospheres without spacing layer (AuNS-OG488-N, green curve) and C) gold nanospheres with an emitter free 7 nm silica spacing layer (inset: AuNS+SiO_2, black curve) and a second dye-doped silica shell (AuNS-OG488-S, red curve).

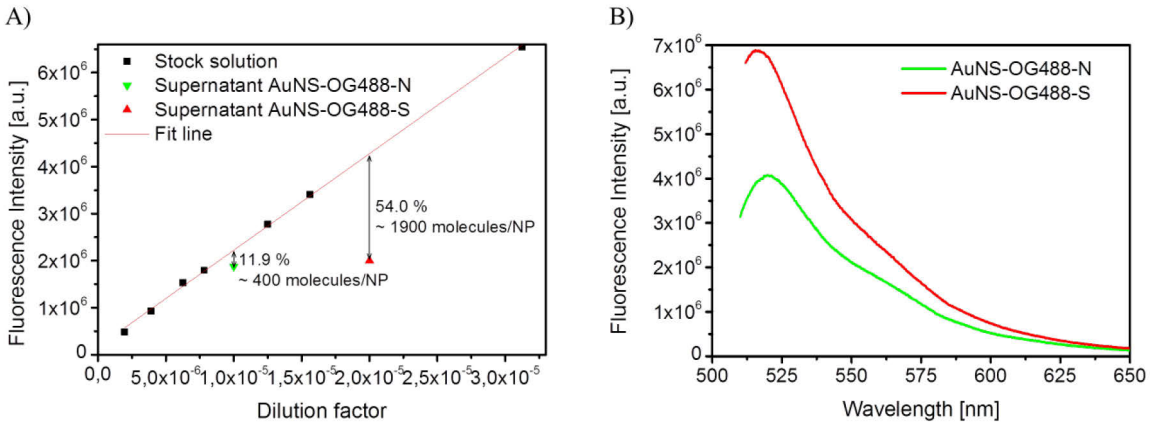

Figure 4.3: A) Fit for the estimation of the dye concentration via dilution of the stock dye-APTES conjugate solution. The fluorescence intensities of exemplary samples are shown as well. The supernatant of the sample AuNS-OG488-S usually showed a lower signal, indicating that more dye molecules were embedded in the silica shell. B) Respective fluorescence spectra of the hybrid nanostructures. The peaks are shifted by approximately 4 – 5 nm compared to the free dye-APTES conjugate.

In general, more dye molecules could be embedded in the silica shell by cleaning the nanoparticles prior the Stöber process. The sample with an emitter free spacing layer, AuNS-OG488-S, was centrifuged and cleaned prior further shell growth and had on average 5-times more dye molecules (Figure 4.3). The reason for that might be the removal of excess sodium metasilicate and APTES from the initial Stöber solution, which provides better incorporation of the dye conjugate in the shell. Still, the amount of dye molecules just barely provides enough emitters as calculated by Noginov *et al*. Higher amounts of the dye-APTES conjugate induced aggregation and unregularly shaped silica shells. The sample without a spacer layer could not be cleaned after coating the nanoparticles with APTES and sodium metasilicate as the sample became unstable after centrifugation. Interestingly, the spontaneous emission of the hybrid gold nanostructures is reduced by a factor of 3 for AuNS-OG488-N and a factor of 6 for AuNS-OG488-S from the calculated dye concentration inside the shell. The emission peak is shifted by 4 nm and 5 nm, respectively, compared to the free dye-APTES conjugate (Figure 4.3). These effects can be attributed to energy transfer or quenching by the gold nanospheres and will be further analysed in chapter 4.2.1.

4.1.2 Gold-silica core-shell nanorods with dye-doped silica shells

The inherent losses of gold at approximately 500 nm are a result from interband transitions as discussed in chapter 2.2.1. Even at 530 nm gold particles exhibit low *Q*-factors below 10.[206] One method to improve the *Q*-factor is to shift the resonance peak to larger wavelengths. This can be achieved by either using larger gold nanoparticles or varying the shape. Larger

nanoparticles are undesired due to enhanced radiative losses (Γ_r^{cav}). Hence, gold nanorods have been synthesized that exhibit tuneable LSPR abroad the whole visible range depending on their aspect ratio (cf. chapter 3.2). The wavelength of the optical pump setup (here the Nd:YAG laser at 532 nm) limits the implementation of NIR-active nanorods with high aspect ratios. Thus, gold nanorods of two different sizes have been synthesized that exhibit a longitudinal LSPR below 650 nm (black curves in Figure 4.4) and have *Q*-factors of 15 – 20.[201] The aspect ratios of these nanorods are very low but both absorption peaks (transversal at ~520 nm and longitudinal at ~570 nm / 620 nm) clearly appear. A thin silica shell of 8 nm has been coated prior dye-functionalization by addition of TEOS to the CTAB stabilized nanorods. The dye-functionalization has been analogous to the spherical nanoparticles with APTES conjugation and co-condensation of the dye-APTES conjugate and TEOS. The dye molecules exhibit emission at 554 nm for Alexa Fluor 532 (AF-532) and at 610 nm for Atto Rho 101 (AR-101). The excitation peak for the dyes is at 532 nm and 586 nm, respectively.

In contrast to OG-488, these dyes have a *N*-hydroxysuccinimide (NHS) ester as amine reactive group. This group is much more reactive than the ITC group, which makes the coupling but also degradation more likely. Careful handling, however, enabled almost quantitative dye-APTES conjugation and a high degree of dye molecules could be embedded in the silica shell. It was shown that gold nanorods synthesized by the standard method (cf. chapter 2.1.1) have about 15% yield of gold nanorods.[207] Thus, only rough estimates can be made to calculate the dye/nanorod ratio as was done for the spherical gold nanoparticles. For NHS coupled dye-APTES conjugates the dye/nanorod ratio has been as high as ~19,500.

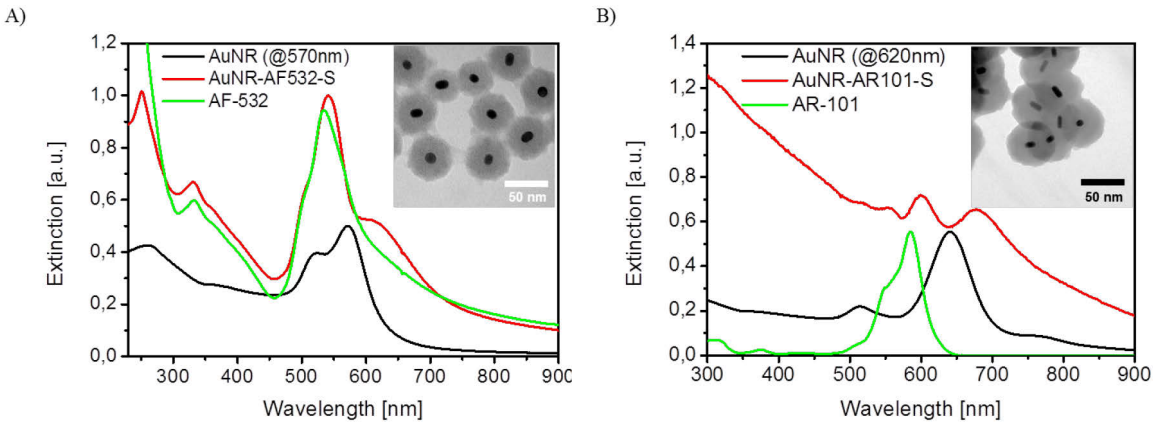

Figure 4.4: UV/Vis spectra of gold nanorods (black curve) that have been functionalized by A) AF-532 and B) AR-101. The red curve shows the hybrid samples AuNR-AF532-S and AuNR-AR101-S that have strong features of the embedded dye molecules (green curve) and from the longitudinal absorption peaks of the gold nanorods.

The high amounts of dye molecules are also clearly visible from the UV/Vis extinction spectra in Figure 4.4. In particular the sample AuNR-AF532-S (Figure 4.4A, red curve) shows strong absorption peaks from the dye (green curve) at 250 nm, 330 nm and 535 nm. The shoulder of the hybrid sample AuNR-AF532-S at 610 nm can be attributed to the longitudinal peak of the gold nanorods that has been shifted due to the higher refractive index surrounding the nanorod after the silica coating. The sample AuNR-AR101-S has been coated successfully as well; however, the sample is slightly aggregated and shows broad absorption. The absorption features of the dye at 590 nm and the nanorod at 680 nm appear as well.

4.1.3 Core-shell nanoparticles with dye-functionalized polymers adsorbed via layer-by-layer approach

Core-shell nanoparticles with dye molecules embedded in a silica shell have shown no spasing features. A possible reason can be the low amount of dye molecules in particular for spherical nanoparticles. Furthermore, theoretical models have shown that the distance dependency influences the spasing threshold tremendously. There is only limited control of the way how dye molecules are incorporated in the silica shell, in particular of the distance from the core. The volume further away of the core is much larger than close to it. Thus, more molecules will be located further away than what might be ideal.

A way to circumvent this problem is to use the layer-by-layer approach. Dye-functionalized polymers are adsorbed on the surface of a metal nanoparticle. Several active layers can be attached to increase the necessary amount of emitters. Furthermore, a silica spacing layer can be synthesized firstly, which allows for precise distance control. The gain medium consists of the same amine-reactive dye molecules which are covalently bound to an amine functionalized polymer. Unreacted dye molecules have been separated via dialysis before the dye-functionalized polymers were lyophilized for later use.

Gold nanoparticles have been synthesized and coated with a thin silica layer as in the previous sections. The silica surface provides silanol groups that are deprotonated at pH 7 and negatively charged. Cationic dye-functionalized poly(allylamine) hydrochloride (PAH) adsorbs as a thin layer on the silica surface via electrostatic interactions. More layers can be adsorbed via the layer-by-layer approach[24] by alternating adsorption of the anionic poly(acrylic acid) (PAA) and PAH. Zeta potential measurements have proven the alternating surface charges after each addition of different polyelectrolytes indicating that respective polyelectrolytes have been attached successfully (Figure 4.5B).

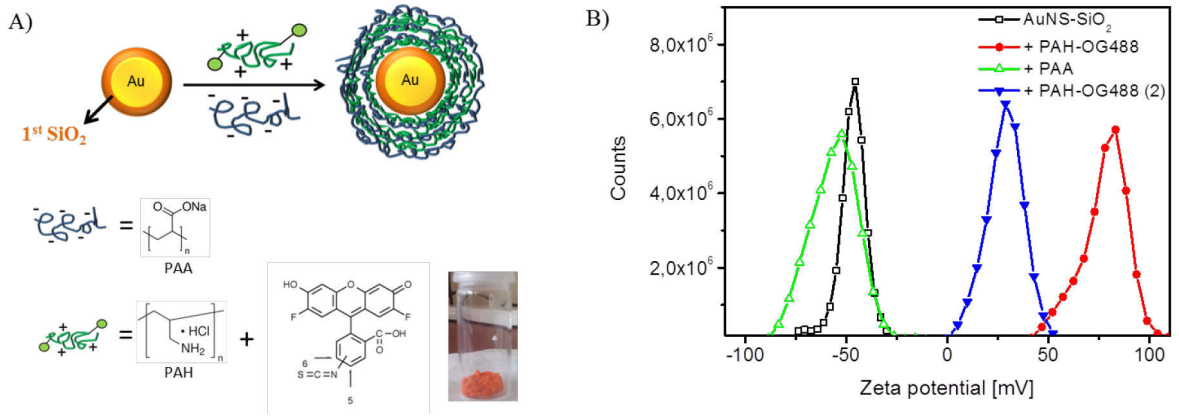

Figure 4.5: A) Layer-by-layer approach: a gold nanoparticle with an emitter free spacer silica coating adsorbs alternating positively charged, dye-functionalized PAH and negatively charged PAA. B) Zeta potential measurements verify successful adsorption of differently charged layers.

This has been also confirmed by UV/Vis spectroscopy of the hybrid gold nanospheres (AuNS-OG488-LBL) and nanorods (AuNR-AF532-LBL). Figure 4.6 shows distinct dye peaks in the absorption spectra of the hybrid gold nanoparticles. Due to the large excess of polymers added, an accurate quantitative analysis of the dye/nanoparticle ratio is impossible. The direct emission signal is impracticable as well due to quenching, energy transfer effects and non-linear behaviour at such high dye densities. However, comparison with the absorption spectra of the dye-doped silica shell (Figure 4.2A) indicates the amount of dye molecules adsorbed via the layer-by-layer approach on the gold nanoparticles must be much higher. Thus, the dye/nanoparticle ratio should be more than sufficient. A drawback that occurs for the layer-by-layer approach is the instability of the silica shell during the adsorption and repetitive washing procedure. The dense spherical shells are still intact; however, the

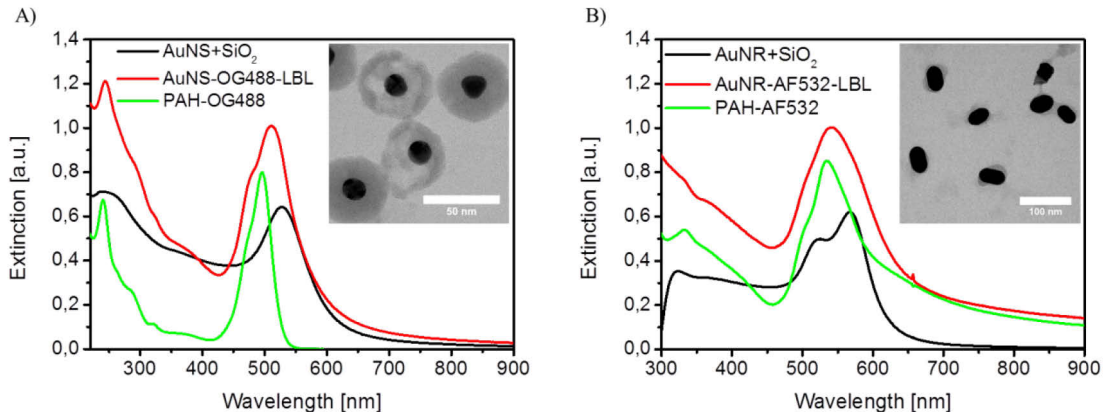

Figure 4.6: UV/Vis spectra of hybrid gold nanoparticles with dye molecules adsorbed via layer-by-layer onto A) gold nanospheres and B) gold nanorods. Strong dye absorption peaks are visible in the hybrid systems. The silica shell gets partly dissolved (TEM images in the inset).

mesoporous silica shell of the nanorod system, formed by the CTAB template, is more susceptible towards dissolution (Figure 4.6 inset).[208]

4.1.4 Gold-silica core-shell nanorods embedded in a dye-polymer film

A very different but simple approach for realization of a spaser was published by Meng *et al.* who organized a dense array of gold nanorods inside a dye-poly(vinyl alcohol) (PVA) matrix.[209] The dye concentrations used have been very high with film thicknesses around 200 nm. Besides regular spontaneous emission, amplified spontaneous emission (ASE) was observed. With gold nanoparticles embedded, a third emission peak appeared which was associated with a spaser signal.

Gold nanospheres and nanorods of different aspect ratios with a thin emitter free silica spacer layer have been produced according to the previous synthesis. To exclude a corporative effect and investigate single nanoparticles, the gold nanoparticles have been spin coated on a glass substrate with the core-shell particles well separated. Three different dye molecules (AF-532, rhodamine B (RhB) and rhodamine 6G (R6G)), emitting light between λ_{em} = 540 – 620 nm, have been dissolved in a viscous PVA solution. The aspect ratio of the gold nanorod and the size of the sphere were varied to match the LSPR absorption accordingly to the dye emission. Several silica shell thicknesses have been synthesized. The viscosity and dye concentrations have been varied to adjust the amount of emitters and film thickness.

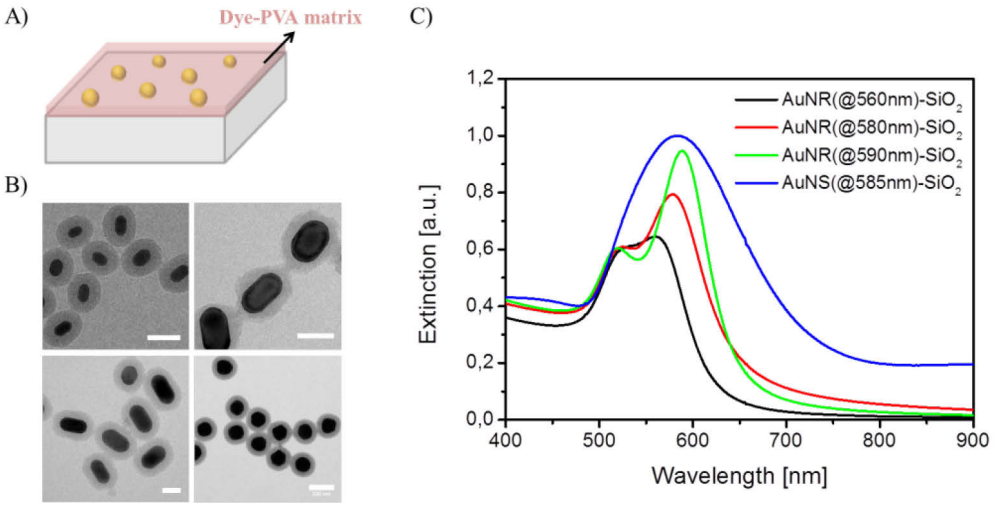

Figure 4.7: A) Scheme of simplified approach for a spaser design with gold nanoparticles in a dye-polymer matrix. B) Various nanoparticles have been synthesized with an emitter free spacer layer; the scale bar is 20 nm for nanorods and 200 nm for the spheres. C) UV/Vis spectra of these gold nanoparticles that match the emission of the dye molecules (λ_{em} = 540 – 620 nm) in the film (black: top left, red: top right, green bottom left and blue: bottom right TEM image in B).

4.1.5 Thermosensitive Gold-PNIPA core-shell structures with adsorbed cadmium telluride quantum dots

As proposed by Stockman[156], luminescent cadmium telluride (CdTe) quantum dots (QDs) have been also applied as a gain medium. Additionally, thermoresponsive properties to control the distance of the emitter particles to the gold surface was intended by synthesizing a PNIPA shell around the gold nanoparticle (cf. chapter 2.1.2 and 3.3). The gold nanoparticle surface was modified firstly by adsorption of N,N′-bis(acryloyl)cystamine (BAC) that provides two double bonds. Then, seeded precipitation polymerization of N-isopropylacrylamide (NIPA) led to a thin PNIPA shell around the gold nanoparticle. The shell is negatively charged due to the anionic initiator used and has a LCST of 27°C (Figure 4.9B). TEM images (Figure 4.8B) and the sharp peaks in the extinction spectra (Figure 4.8D, black line) show that the gold nanorods do not aggregate during this process.

The group of Professor Alexander Eychmüller from the Technical University Dresden provided 6 nm CdTe QDs that are stabilized by negatively charged 3-mercaptopropionic acid (MPA).[210] They exhibit emission in the range of 700 – 900 nm which coincidences very well with the absorption of the longitudinal LSPR of gold nanorods with an aspect ratio of 3.6. Figure 4.8D shows the photoluminescence (PL) of CdTe QDs of 6 nm in size (green curve). The small peak at 900 nm corresponds to the scattering peak of the second harmonic generated light by the monochromator (λ_{ex} = 450 nm). These QDs have been functionalized by a positive polyelectrolyte (PAH), which led to slight aggregates of double the size. The positively charged CdTe QDs now have been adsorbed on the PNIPA shell (Figure 4.8C) and the excess QDs have been separated by repetitive centrifugation from the gold nanorods.

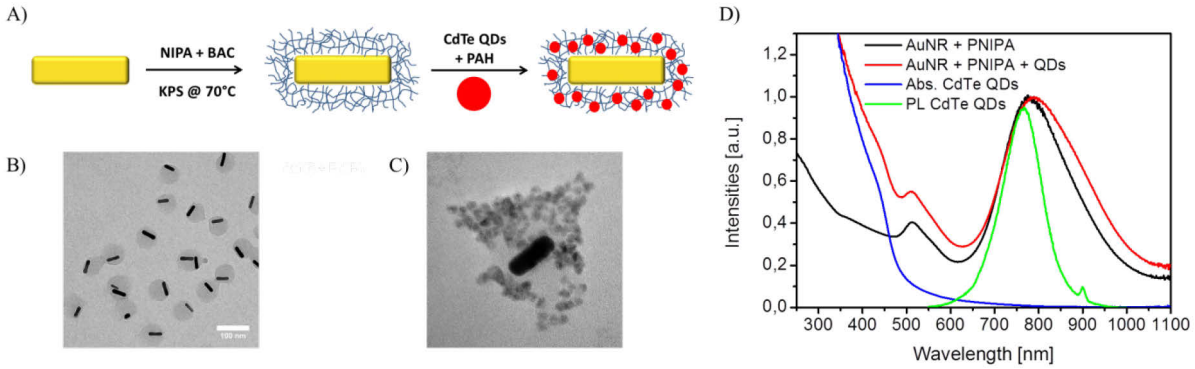

Figure 4.8: A) A thermosensitive PNIPA shell is synthesized around gold nanorods (TEM image in B), which allows for the adsorption of CdTe QDs (TEM image in C). D) The UV/Vis and fluorescence spectra show that the photoluminescence and absorption of CdTe QDs and the gold nanorods overlap spectrally and that the gold nanorods remain well separated after QDs functionalization.

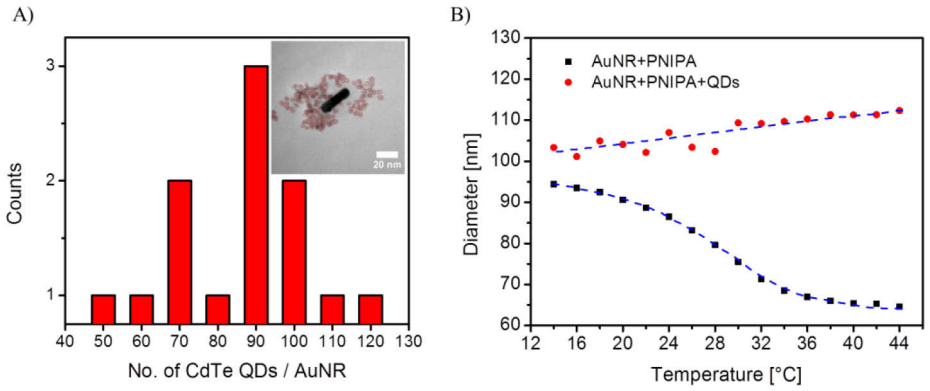

Figure 4.9: A) Number of CdTe QDs per gold nanorod, as counted from TEM images (exemplarily shown in the inset). B) The thermoresponsive behaviour of the microgel shell is lost after QDs adsorption.

All adsorption processes have been followed successfully by zeta potential measurements. This is also verified by UV/Vis spectroscopy: After adsorption of the CdTe QDs, the spectrum of the hybrid gold nanorods shows much stronger absorption in the blue and UV region due to the QDs. The distinct peaks of the gold nanorods at 513 nm and 790 nm are still present and their shape remain which indicates that the gold nanorods do not aggregate and are well separated due to the PNIPA microgel (Figure 4.8D). From several high magnification TEM images, 50 – 120 QDs can be counted for each gold nanorod (Figure 4.9A). Unfortunately, the strong interaction of the QDs with the PNIPA microgel leads to a modified temperature response and the phase transition is lost after QDs adsorption (Figure 4.9B).

4.2 Results of the pump-probe experiments

4.2.1 Core-shell nanoparticles (dye doped silica and layer-by-layer)

To verify energy transfers and modified excited state responses between the emitter molecules and the gold nanoparticle, lifetime measurements have been conducted. Gold nanospheres with dye doped silica shells have been casted on a glass substrate well separated from each other as verified by confocal fluorescence microscopy (Figure 4.10B). Additionally, the gold core of the same hybrid structure was dissolved with a potassium cyanate (KCN) solution (Figure 4.10A). These structures have been subject to a Ti:sapphire laser and compared with one another. Additionally, the suspended particles have been investigated and compared. Figure 4.11 shows the normalized lifetime measurements and their exponential fits. All data has been fitted with a bi-exponential decay and the results are summarized in Tab. 4.1.

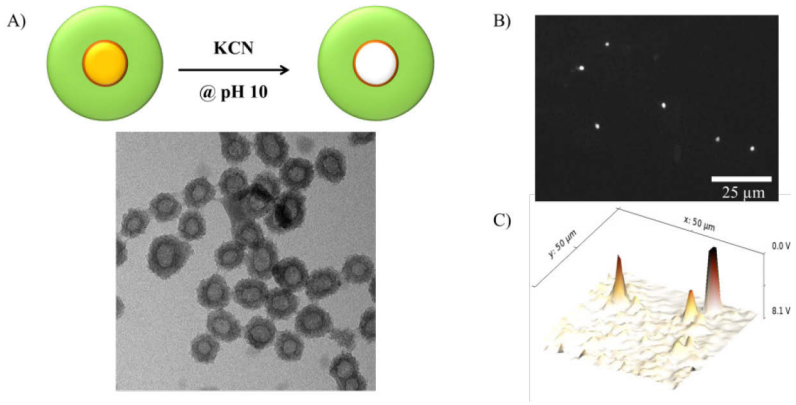

Figure 4.10: A) Scheme of gold removal of the hybrid dye-silica coated gold nanospheres and a respective TEM image. B) Confocal fluorescence microscope image of the sample AuNS-OG488-N and C) a scan of the confocal fluorescence microscope used at the Ti:sapphire laser setup (50x50 µm segment).

The suspended hybrid particles show stable decay rates regardless of the illumination time even at very high intensities. As mentioned earlier, this is due to diffusion of the nanoparticles in and out of the beam focus. The sample with gold cores has a decreased lifetime which indicates higher decay rates and new decay channels besides the radiative spontaneous emission of OG-488 dye molecules. Figure 4.11 shows two different decay rates, a fast one and a slow one for the hybrid nanoparticles with a gold core. The slow decay rate corresponds to the single decay rate of the KCN-etched hollow nanoparticles with a lifetime of $\tau_{slow} = 4.3$ ns. This is well in agreement of the spontaneous emission of free OG-488 molecules (4.1 ns[*]) and also what Noginov *et al.* have reported.[31] The fast decay rate is $\tau_{fast} = 1.7$ ns for hollow nanoparticles and $\tau_{fast} = 0.9$ ns for nanoparticles with a gold core. However, the amplitude for the fast decay rate of the hollow system can be neglected and its origin is dye-dye interactions.[211] As seen in Figure 4.11 this is clearly not the case for the hybrid gold nanoparticles and the fast decay rate can be attributed to the interaction with the gold nanospheres. Gold PL can be excluded, as these processes are much faster (< 1 ps).[212]

The shortest average decay rate by Noginov *et al.* has been down to $\tau_{average} = 1.6$ ns for their hybrid nanosystem. The sample AuNS-OG488-N has an average lifetime of $\tau_{average} = 2.65$ ns, which means that the contribution of spontaneous emission might be higher for the AuNS-OG488-N sample. However, when looking at single hybrid nanoparticles on a substrate a bleaching effect can be observed. At low intensities, the average lifetimes of nanoparticles with and without gold are similar and close to the values of the spontaneous emission of OG-488. At higher pump intensities (where spasing is to be expected) the lifetime

[*] ISS, Inc. Champaign, IL 61822; Lifetime Data of Selected Fluorophores (www.iss.com).

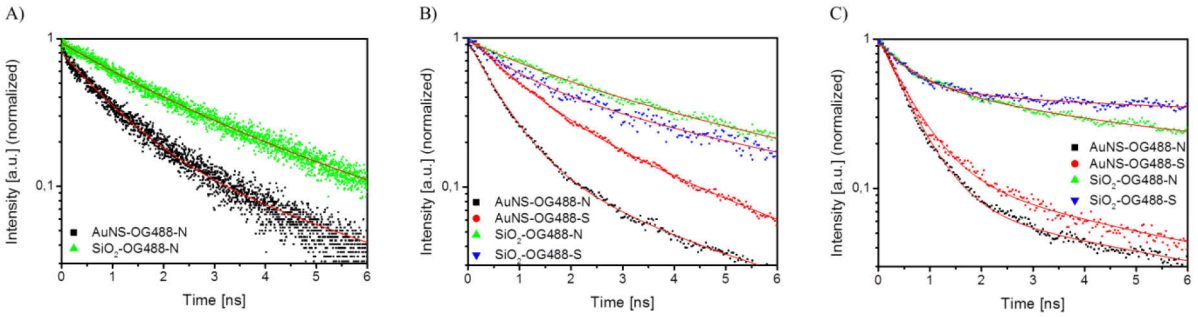

Figure 4.11: Lifetime measurements of A) suspended particles and particles casted onto a substrate (B + C). The hybrid gold nanospheres systems decay faster than their equivalent with the gold core leached by KCN. Furthermore, there is a pronounced bleaching effect for the hybrid systems on substrates: B) lifetime measurement after 10 s and C) after 180 s at 750 µW, respectively.

reduces quickly to $\tau_{average}$= 1.98 ns and $\tau_{average}$= 1.96 ns for the gold nanospheres systems with and without an emitter free spacing layer, respectively. The reduction of the average lifetime can be explained with higher stability of conjugated dye molecules: The dye molecules that interact with the gold core get bleached slower as they have a very fast deactivation channel, i.e. non-radiative energy transfer to generate plasmons (Γ_g). Dye molecules that are further away do not have such a decay channel and are more susceptible to photo-bleaching. Hence, more dye molecules interacting with the plasmons remain active, which leads to a reduction of the average lifetime. Such a stability increase was reported for a few biological systems before but has not been investigated on a single particle level.[213-217]

Furthermore, most systems have trapped the molecules in a shell which can hinder the diffusion of oxygen, which causes chemical modification of the highly reactive excited dye molecules via oxidation. It was e.g. shown that simple polymer particles that take up dye molecules also effectively protect the fluorophores.[218] For the hybrid gold nanospheres such protection from bleaching might be possible as well, however, the hollow hybrid nanoparticles without gold do not show such a decrease in lifetime, even at higher pump intensities. Their values remain constant and similar to the free spontaneous emission. This indicates that the reduction of the average lifetime is indeed due to higher photo-stability of fluorophores that interact with the plasmonic gold core.

The hollow sample SiO_2-OG488-S has a slightly decreased average lifetime compared to its equivalent without an emitter free shell. This effect originates from a higher amplitude of the fast decay rate, which is still low compared to the samples with gold cores. The reason for that can be explained by stronger self-quenching by the dye molecules as the fluorophore concentration in the silica shell is higher for the sample with an emitter free layer

Tab. 4.1: Average lifetime $\tau_{average}$ in nanoseconds of hybrid particle suspensions or of single particles on a substrate. The single hybrid gold nanospheres showed strong bleaching behaviour at high pump intensities.

Sample	AuNS-OG488-N (solution)[†]	SiO_2-OG488-N (solution)[†]	AuNS-OG488-N (substrate)	SiO_2-OG488-N (substrate)	AuNS-OG488-S (substrate)	SiO_2-OG488-S (substrate)
$\tau_{average}$ (10s@50µW)	-	-	3.87±0.75	4.57±1.27	3.38±1.14	3.34±0.83
$\tau_{average}$ (60s@50µW)	-	-	4.21±0.70	4.14±1.29	3.33±0.80	3.58±1.28
$\tau_{average}$ (180s@50µW)	-	-	4.22±0.91	4.44±1.59	3.49±0.89	3.55±1.03
$\tau_{average}$ (10s@750µW)	2.65±0.36	3.64±0.94	3.08±0.83	4.11±1.18	2.91±0.44	3.86±0.87
$\tau_{average}$ (60s@750µW)	-	-	1.95±0.60	4.01±0.87	2.44±0.38	3.83±0.46
$\tau_{average}$ (180s@750µW)	-	-	1.96±0.51	4.04±0.70	1.98±0.38	3.80±0.69

(cf. 4.1.1).[219] Further, the lifetime response of the photo-bleached hollow nanoparticles varies slightly, which can be addressed by quenching of active dye molecules with bleached (chemically modified) molecules.[211] The average lifetime, however, is not influenced by these effects.

4.2.2 Core-shell gold-silica nanoparticles in dye-PVA films

In the same way as for the dye-doped silica hybrid nanoparticles thin RhB-films with gold nanoparticles and varying spacer thickness have been investigated for their lifetimes with the pulsed diode laser at 532 nm (Figure 4.12). The results are summarized in Tab. 4.2, which show a similar bleaching effect over time as the core-shell structures in the previous section. Pure, thin and diluted RhB-films have an average lifetime of 1.25 ns, which is slightly lower than the literature values (1.68 ns[*]) and can be explained again by self-quenching.[219] Confocal fluorescence microscopy images have been made for all samples and verified that the gold particles are well separated (Figure 4.12C). Enhanced fluorescence near metal nanoparticles was found in particular for gold particles with a thicker silica shell via the Purcell effect. This is to be expected, as resonant gold particles can quench the fluorescence at low distances (cf. 2.3.1). In general gold nanoparticles reduce the average lifetime further, in particular for nanoparticles that have a thinner silica shell, which brings the dye molecules closer to the electric field generated by the nanoparticles. The lifetime decreases over time as has been

[†] No bleaching effect was visible for the suspended systems.

Tab. 4.2: Average lifetime $\tau_{average}$ in nanoseconds of dye molecules near gold nanospheres and nanorods with varying silica spacer thickness. The lifetimes decrease over time only for films with gold nanoparticles.

	RhB-film	AuNR-w/oSiO_2	AuNR-8nmSiO_2	AuNR-15nmSiO_2	AuNR-25nmSiO_2	AuNS-w/oSiO_2	AuNS-10nmSiO_2	AuNS-20nmSiO_2
$\tau_{average}$ (5s)	1.28±0.23	0.88±0.14	0.91±0.29	0.85±0.16	1.11±0.28	0.69±0.31	0.82±0.23	1.00±0.15
$\tau_{average}$ (60s)	1.16±0.35	0.84±0.28	0.84±0.22	0.79±0.12	0.95±0.42	0.68±0.19	0.79±0.18	0.82±0.23
$\tau_{average}$ (120s)	1.22±0.38	0.82±0.32	0.83±0.37	0.77±0.18	0.95±0.34	0.67±0.15	0.77±0.23	0.78±0.14
$\tau_{average}$ (300s)	1.33±0.41	0.80±0.31	0.82±0.27	0.79±0.24	0.93±0.37	0.65±0.18	0.77±0.24	0.73±0.28

seen for the core-shell gold nanoparticles for the same reasons, i.e. an enhanced photo-stability for dye molecules close to the metal nanoparticle. For the pure RhB-films such behaviour could not be observed (Tab. 4.2). Dipole LSPR-resonant 120 nm gold nanospheres show the strongest metal-dye interactions and spacer dependency, while the gold nanorods exhibit similar decay times. The reason for that might be the mesoporous silica shell of gold nanorods that allows for dye molecule diffusion into the silica shell. Due to the different synthesis conditions, the diffusion of molecules is much more hindered in the more dense silica shell for the gold nanospheres. Further, it is to be expected that the lifetime of RhB molecules close to the gold nanoparticles is in reality even more decreased because also dye molecules that are not in the near-field of the particle have been also excited. However, these molecules contribute to the average lifetimes that have been measured, too. Similar values have been reported for gold-silica core-shell nanoparticles with adsorbed RhB molecules.[220]

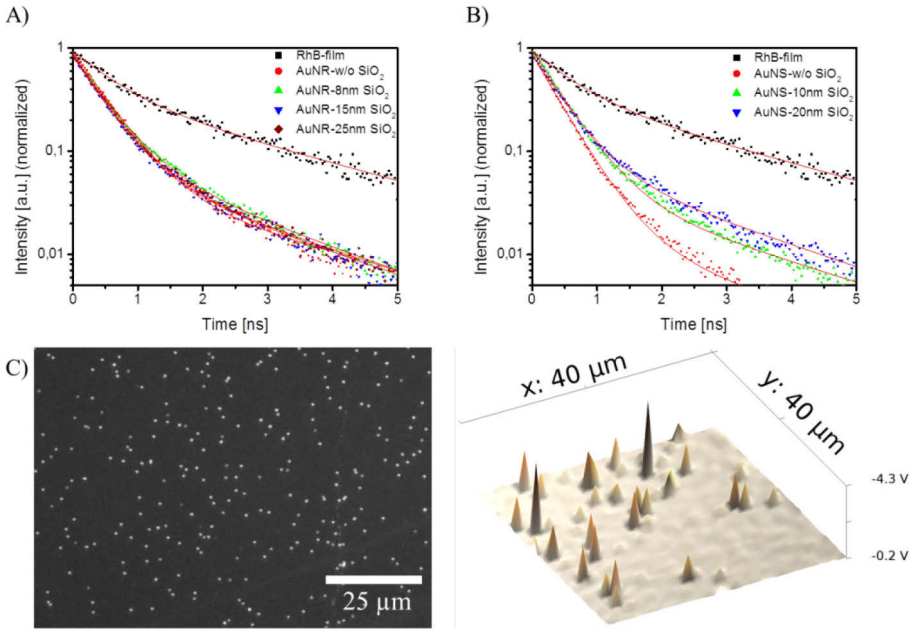

Figure 4.12: Lifetime measurements of A) gold nanorods and B) gold nanospheres with varying silica spacer thicknesses (after 5 s at 450 µW). A pronounced effect is in particular seen for gold nanospheres without a spacer layer. C) Confocal fluorescence microscope image of gold nanospheres coated with a 20 nm silica shell on the left and a corresponding emission scan of a 40x40 µm segment taken with the Ti:sapphire laser setup.

4.2.3 Gold-PNIPA nanorods with adsorbed CdTe QDs

CdTe QDs have been adsorbed on the PNIPA shell of gold nanorods. The PAH modified QDs show a new PL spectra that varies from the CdTe QDs stabilized by MPA. Besides the emission peak at 800 nm, a rather broad emission peak around 680 nm appears (Figure 4.13). It is known that CdTe QDs are very sensitive to their environment (solvent, capping agent, etc.) and the PAH might influence the surface state of the QDs.[221-223] Another, more likely, possibility is the partial degradation of the CdTe QDs due to oxidation. The PAH modification was conducted under ambient conditions and ultra-sonication. In particular for aqueous solutions (with oxygen present) such oxidative processes have been reported that result in a blue shift and losses in quantum yield.[224, 225] Furthermore, high dilution in ultra-pure water is known to dissolve ions from the surface in a matter of a few days due to the lack of stabilizing ligands in solution.[226] The photoluminescence of PAH modified QDs decreases with increasing temperature, which can be explained by non-radiative processes, i.e. thermal escape induced by multi-phonon absorption.[227, 228]

After adsorption on gold nanorods the PL decreases in the spectral range of 650 – 850 nm. Overall the integrated PL signal decreases by almost 55% in this area. This wavelength region coincidences well with the absorption by the longitudinal LSPR of the gold nanorods. Hence, strong quenching or non-radiative energy transfer from the QDs to the gold nanorods is very likely. This has been further verified by lifetime measurements. The lifetime measurements of MPA-caped QDs and PAH modified QDs are slightly increased for the PAH modified QDs but mostly independent of the temperature. The lifetime has been fitted by a threefold-exponential decay with one major contribution by a lifetime of approximately 30 ns. This indicates that trap states are involved in the recombination.[229, 230] Due to degradation of CdTe QDs the surface states might lead to stronger trapping of the excitons that causes the enhanced lifetime of excited states.[231] The other major contribution to the lifetime measured for these QDs is the very fast band-edge or Auger recombination.

Tab. 4.3: Lifetime measurements (in nanoseconds) of QDs with and without gold nanorods. The ratio of the fast decay rate (I_{fast} / I_{slow}) increases strongly when the QDs are in close vicinity to the gold nanorods.

sample	$\tau_{average}$	τ_{fast}	I_{fast}	τ_{slow}	I_{slow}
AuNR+QDs @ RT	20.7±2.9	0.30±0.01	0.90±0.02	25.5±2.4	0.06±0.002
AuNR+QDs @ 50°C	21.3±3.9	0.31±0.01	0.91±0.01	26.8±3.3	0.05±0.002
QDs stock @ RT	27.4±1.4	0.26±0.01	0.40±0.01	28.5±1.1	0.43±0.002
QDs+PAH @ RT	33.3±4.4	0.31±0.01	0.48±0.01	35.0±3.7	0.36±0.004
QDs+PAH @ 50°C	30.7±2.6	0.29±0.02	0.47±0.01	32.0±2.2	0.39±0.004

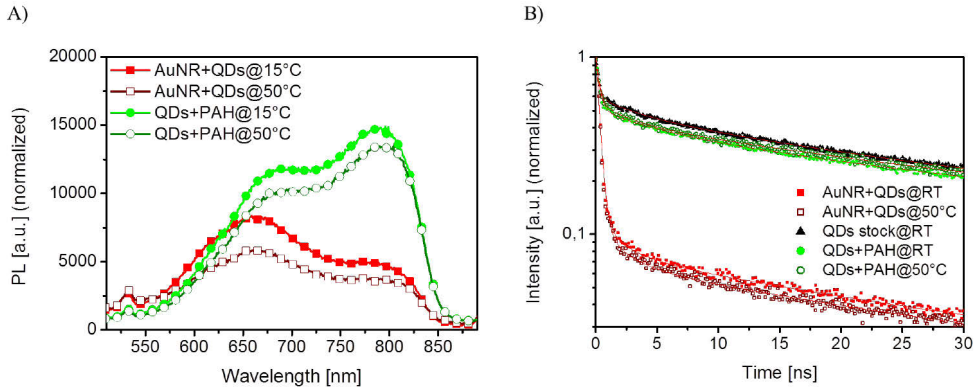

Figure 4.13: A) Normalized PL (λ_{ex} = 450 nm) spectra of QDs modified with PAH (green curve, circles) and adsorbed on gold nanorods (red curve, squares) at room temperature (solid symbols) and at 50 °C (hollow symbols). The PL is quenched by the longitudinal LSPR of the gold nanorods. B) Lifetime measurements of QDs with and without gold nanorods. Gold nanorods decrease the lifetime of the QDs via non-radiative energy transfers (λ_{ex} = 485 nm).

This changes when the QDs are in close vicinity to the gold nanorods. LeBlanc *et al.* have investigated CdSe QDs near a metal film and have reported of a very similar behaviour. The total emission in their experiments has been decreased by ~50% with a twofold decrease in lifetime. They concluded that Auger recombination is not responsible for the increased fast decay rate, but non-radiative energy transfer and plasmon-coupled emission from QDs excitons.[232] This explains as well the decrease in total emission shown in Figure 4.13, as shorter lifetimes usually increases the PL intensity.[233, 234] Further, the modified lifetime response (~0.3 ns) is in very good agreement of literature values, where gold nanoparticles have been coated with CdS QDs.[212] As shown in Figure 4.9, the thermoresponsive behaviour was lost after CdTe QDs adsorption. Hence, no difference in the temperature response has been found for the quantum efficiency or lifetime for QDs adsorbed on the hybrid gold-PNIPA nanorods.

4.3 Discussion of the missing spasing signals

None of the systems has shown spasing features, i.e. sharp peaks with reduced lifetime responses and non-linear behaviour. Initially a pulsed laser (Ti:sapphire or diode) has been used to pump the gain medium of the hybrid nanostructures at 485 nm or 532 nm, respectively (cf. the pump-probe experiments in 4.2). The core-shell gold-silica particles used did not show any peaks aside from the spontaneous emission. Neither liquid samples in a quartz cuvette, nor spin coated samples showed sharp peaks that resemble the reports by Noginov *et al.*[31] Furthermore, spin coated samples showed quick bleaching at high pump rates, while

particles suspended in ethanol can diffuse in and out of the laser focus and are more stable. The high repetition rates at 80 MHz of the Ti:sapphire and laser diode complicated the single particle investigation due to the fast bleaching processes. Hence, a 10 Hz low repetition rate Nd:YAG laser with emission at 532 nm was used to investigate the hybrid structures that have been spin coated on substrates. These results have been obtained by Günter Kewes from Humboldt University Berlin.[204]

4.3.1 Core-shell nanoparticles (dye-doped silica and layer-by-layer)

Individual hybrid core-shell nanospheres and nanorods synthesized with the gain medium embedded in the silica shell or via the layer-by-layer approach showed weak spontaneous emission. Upon increasing the pump power of the Nd:YAG laser and focusing the beam a sharp peak emerged in the spectra (Figure 4.14). This peak, however, originates from the ionization of the substrate which shows luminescence, similar to a technique called laser-induced breakdown spectroscopy (LIBS).[235] For suspended particles and reference samples without particles such a peak has been observed for high pump intensities of the Ti:sapphire laser as well.

Theoretical calculations in the paper of Noginov *et al.* resulted in a necessary gain of 2,000 molecules to achieve spasing for spherical gold nanoparticles at 525 nm. However, there are several ideal assumptions that exclude effects like photo-bleaching, self-quenching and the distance dependence of the dye molecules in the near-field. These aspects cannot be neglected as shown by the pump-probe experiments and the theory model that showed improvement by several orders of magnitude when a spacer layer is introduced. Furthermore, degenerated modes and competitive multipolar modes exist that can influence the amount of actually needed gain values.

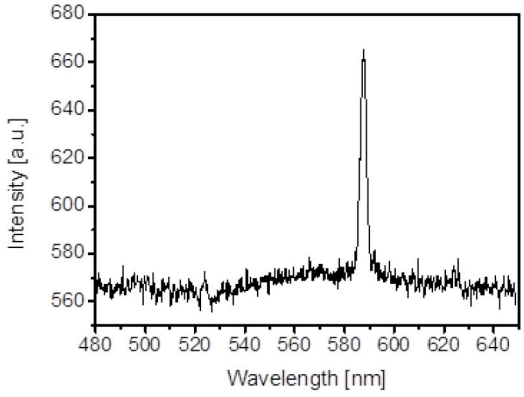

Figure 4.14: Laser-like peak that resembles the spaser peak shown by Noginov *et al.*[31] The observed peak likely stems from glass ablation. Weak emission of fluorescent core-shell gold nanoparticles can be seen. Reprinted with permission from Ref. [204].

The model derived by Günter Kewes allowed for calculation of the minimum gain values needed to achieve spasing at certain frequencies.[204] Even by improvement of the spaser architecture and neglecting the mentioned non-ideal behaviour, minimum gain values of about 30,000 cm^{-1} are necessary at the resonant wavelength. In the case of Noginov *et al.* gain values of 16,000 cm^{-1} have been calculated for 2,700 embedded molecules.[204] As mentioned in chapter 2.3.2 such high gain values are unrealistic and self-quenching definitely occurs. This has been observed as well in the pump-probe experiments. After calculating the needed pump powers the heat generated in the metal nanoparticle (via losses) can be derived. For such high pump powers the gold core would actually melt. Even under assumption of the spaser running at the threshold conditions with a perfectly efficient gain medium the conditions for spasing are too unrealistic.[204]

Noginov *et al.* have measured in their report five points and a small kink has been construed as a spaser threshold. Furthermore, all measurements were made in solution with an ensemble of billions of nanoparticles and random lasing or other effects cannot be excluded. The density of molecules calculated ($\rho = N_{molecules} / V_{shell} = 6.3 \cdot 10^{19}$ cm^{-3}), i.e if all emitters are excited, is still less than a half of what Stockman has calculated as well.[158] After development of the model the literature report from 2009 (that needs yet to be reproduced) becomes very doubtful. Though the amount of dye molecules in our systems for the spherical particles is hardly enough, the nanorod system and the layer-by-layer approach should provide sufficient gain for spasing. However, the high pump intensities needed, photo-bleaching and self-quenching as well as possible damage to the gold core likely inhibit spasing. To put it simply: Gold as plasmonic material exhibits too high losses to be compensated via organic gain material, in particular at these wavelengths.

4.3.2 Core-shell gold-silica nanoparticles in dye-PVA films

Similar to Meng *et al.*, samples have been prepared and investigated with the low repetition rate (10 Hz) and high power Nd:YAG laser as well. However, the conclusion gained deviates from the results in their reports.[209] Our emission spectra have shown a high sensitivity towards the position of the sample and film thickness, which has had a greater effect than the gold nanoparticle incorporation. Random lasing, i.e. multiple sharp peaks, has been seen for highly concentrated samples (Figure 4.15). The reasons for these are inclusions or small crystals of dye molecules that did not distribute homogeneously. These inclusions build small micron-sized resonators that evoke laser features and could be avoided by heating the dye-PVA solutions or reducing the dye concentration before spin coating.[204]

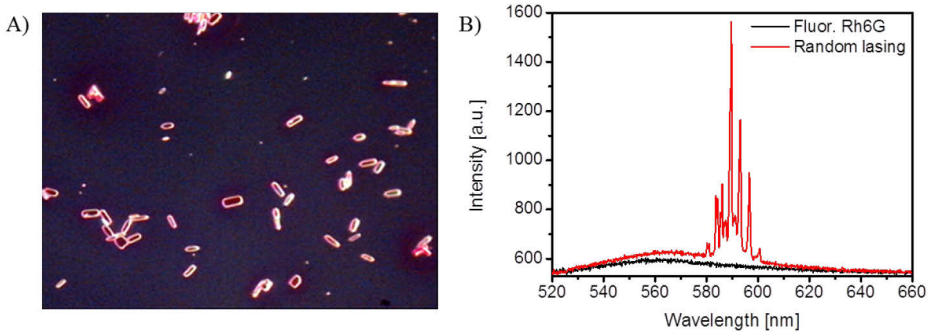

Figure 4.15: A) Optical microscopy image of dye inclusions at very high dye concentrations. B) Comparison of spontaneous emission of R6G and random lasing of the same dye caused by the inclusions that act as small resonators. Reprinted with permission from Ref. [204].

Like in the publication of Meng *et al.*, amplified spontaneous emission (ASE) peaks have been found for rather thick dye-PVA films (Figure 4.16). ASE is spontaneous emission that has been amplified by stimulated emission and is non-coherent.[236] The ASE peaks are largely independent of the gold nanoparticles being present or not. Instead, the film thickness heavily influenced the peak position and intensity of these ASE peaks and they disappeared for very thin films.[204]

It is remarkable that the films prepared by Meng *et al.* have been 200 nm thick. This should lead to a strong background signal of spontaneous emission of the dye molecules that are out of reach from the near-field of the plasmonic gold nanorods. Rather than spasing signals, the observed broad peaks can be attributed to ordinary ASE peaks. Thick dye-doped films and large pumped areas (1.6 mm laser spot size) are common for investigations on wave-guiding and studies on organic dye molecules.[236, 237] Meng *et al.* have observed ASE peaks as well for dye films without any gold nanoparticles. Wave-guiding effects are surely to be influenced by embedding the gold nanorods in a thick dye film.[238] Laser-like peaks and threshold behaviour has been also observed earlier by Popov *et al.* under the same conditions.[239] The conclusion of our experiments that are similar to the way how Meng *et al.* approached their results, suggest that not spasing was seen but rather some sort of wave-guiding and ASE effects.[204]

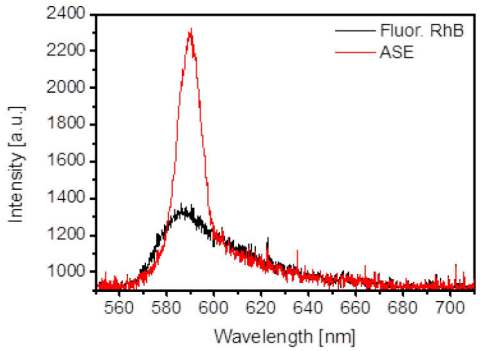

Figure 4.16: Spontaneous emission and amplified spontaneous emission (ASE) of RhB. ASE peaks have been observed at high pump powers for large film thicknesses. Reprinted with permission from Ref. [204].

4.3.3 Gold-PNIPA nanorods with adsorbed CdTe QDs

To calculate the gain values reached for CdTe QDs adsorbed on gold nanorods the density of QDs is multiplied with the absorption cross-section ($g = \rho \cdot \sigma_{abs}$). The emitter density of CdTe QDs is relatively low compared to the dye-molecules due to their larger size ($\rho = 2.0 \cdot 10^{17}$ cm^{-3}, for $N_{QD} = 100$ and $r_{shell} = 50$ nm). However, the absorption cross section of QDs is orders larger in the range of $\sigma_{abs} = 1 \cdot 10^{-14}$ cm^2 as reported elsewhere.[240-242] This leads to an approximate gain factor of 2,000 cm^{-1}. Even though the quality factor of gold in the NIR region is around 40 and hence about four-times larger (cf. 2.3.2), the gain seems to be still insufficient to achieve spasing. Besides the low amount of QDs adsorbed on the PNIPA shell, the likely oxidation on the surface and the modified PL after PAH modification may contribute to the absence of spasing signatures as well.

4.4 Outlook for true nanoscopic spaser systems

As discussed in the last section the inherent losses of gold inhibit spasing on the nanoscale. One approach could be to find chemically stable dye molecules in the NIR where gold exhibits lower losses. However, many dye molecules are not very stable at higher pH values needed for the sol-gel chemistry to embed them in a silica shell. The second approach is to change the plasmonic material. Silver has much lower losses and sufficient gain might be reached at values below 1,000 cm^{-1} with organic dye molecules.[204] Another interesting approach might be a fully dielectric laser that provides low-loss modes. Silicon e.g. is a suitable material that has high quality factors and low non-radiative decay rates.[206] Furthermore, its natural oxidative layer provides a native spacer layer and good functionalization ability.

5. Light-trapping via plasmonic metal nanoparticles

In chapter 2.4.1 the application of plasmonic nanoparticles in solar cells as centres for scattered light and the light trapping mechanism was introduced. Most thin film solar cells show good and efficient absorption properties in the UV to yellow light region, but poor absorption at higher wavelengths. Implementation of metal nanoparticles can enhance the absorption in this wavelength region if these metal nanoparticles scatter the light efficiently. Parasitic absorption by the metal nanoparticle must be avoided under any circumstances when using this light trapping mechanism. As discussed in chapter 2.2.3 and 3.1 the albedo (the ratio of scattered light to absorbed light) increases significantly with the particle size. Moreover, the dipole LSPR shifts towards larger wavelengths which is beneficial, as small silver and gold nanoparticles have their LSPR peaks at undesired lower wavelengths (400 – 530 nm). In particular silver nanoparticles are favourable due to their high scattering ability and low parasitic absorption for nanoparticles larger than 50 nm in size.[243]

Figure 5.1 shows some calculated spectra for spherical silver and gold nanoparticles with different diameters (50 nm, 90 nm and 160 nm) in water. The spectra have been calculated with the program MiePlot V4.4.01‡, which is based on the classic BHMIE algorithm for Mie scattering from a sphere as published by Bohren and Huffmann.[171] Complex refractive indices were used as published by Segelstein[244] for water and by Johnson and Christy for silver and gold (cf. 2.2.1).[134] The spectra show the cross-sections of the extinction and its corresponding scattered and absorbed fractions. Silver in general exhibits LSPR at lower wavelengths than gold. For 50 nm sized silver nanoparticles the major contribution is the scattered fraction, while gold nanoparticles mainly absorb the light. For nanoparticles of 90 nm in diameter the scattering becomes more pronounced for gold and both, silver and gold, exhibit dipole and quadrupole LSPR modes. Larger nanoparticles, e.g.

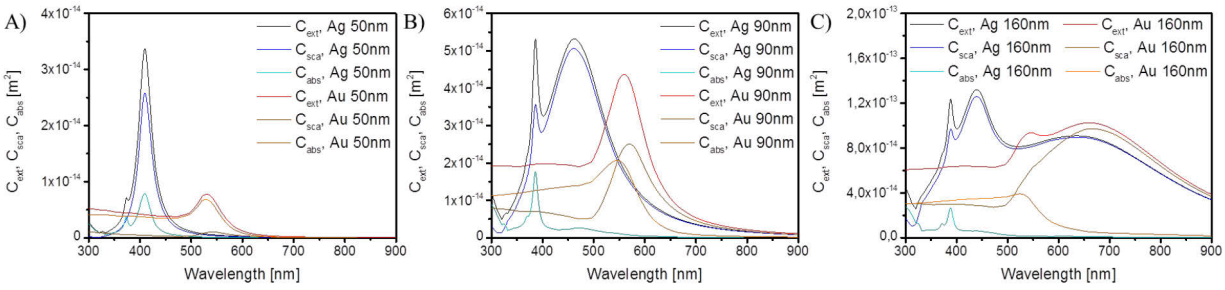

Figure 5.1: Calculated extinction cross-sections in water of silver (blue lines) and gold (red lines) at different diameters: A) 50 nm, B) 90 nm and C) 160 nm. Additionally the spectra show the scattered and absorbed fractions. Calculations were done by the program MiePlot V4.4.01.

‡ http://www.philiplaven.com/mieplot.htm

160 nm in diameter, show in majority scattering with a very broad dipole mode due to retardation effects (cf. 3.1) and higher order modes. As discussed in chapter 2.2.1, gold exhibits intraband transitions that lead to absorptive losses below 550 nm.

As Figure 5.1 has shown, silver nanoparticles are superior over gold nanoparticles regarding their plasmonic properties. In chapter 2.4.1 different fabrication methods have been discussed and the benefits of colloidal nanoparticle synthesis have been explained, i.e. high control over nanoparticle morphology and density. However, a common concern is the parasitic absorption of nanoparticles, not only by Ohmic losses within the metal nanoparticle, but also by direct absorption of tarnished metal nanoparticles. This was for example shown by Yang *et al.*: They investigated the fate of silver nanoparticles integrated in a solar cell and found that the efficiency drops over the time due to silver degradation.[183] This is an open issue in the field of plasmonics and understanding or avoiding these losses is of great importance. The work shown in chapter 5.1 has been published by the author and were partly reprinted with permission from the publisher.[59]

5.1 Scattering enhancement by annealing of silver nanoparticles

5.1.1 Preparation and characterization of silver nanoparticle films for light trapping

As shown in Figure 2.11A of chapter 2.4, the solar light is poorly absorbed in solar cell absorbers above a wavelength of 600 nm. Figure 5.1 shows that silver nanoparticles with a diameter of 160 nm show broadband scattering in the wavelength region of interest and are suitable for the application in plasmonic solar cells. The synthesis of monodisperse quasi-spherical silver nanoparticles above 100 nm in diameter still remains a challenge. The reduction of silver ions often leads to polydisperse samples (cf. 2.1.1). Good control over shape and size of the silver nanoparticles can be attained by slowing down the reaction and multi-step growth. Steinigeweg and Schlücker developed a wet chemical approach in ethylene

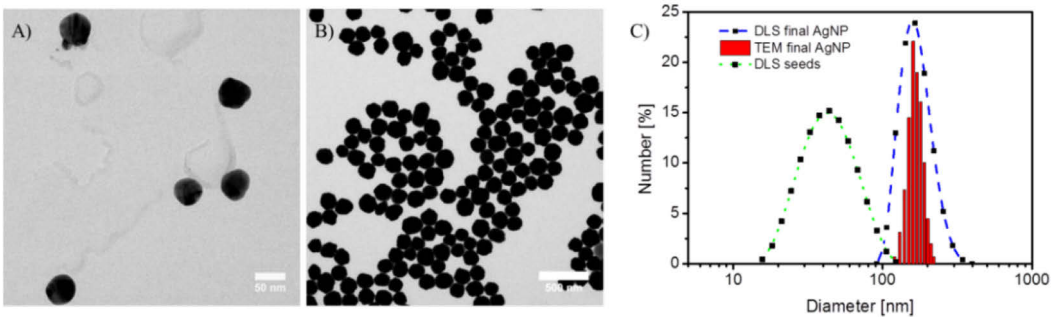

Figure 5.2: TEM images of A) 50 nm silver seeds and B) 164 nm silver nanoparticles. C) Size distribution of silver seeds and the as-prepared silver nanoparticles derived from DLS and TEM measurements. Reprinted from Ott *et al.* [59], © IOP Publishing (2014).

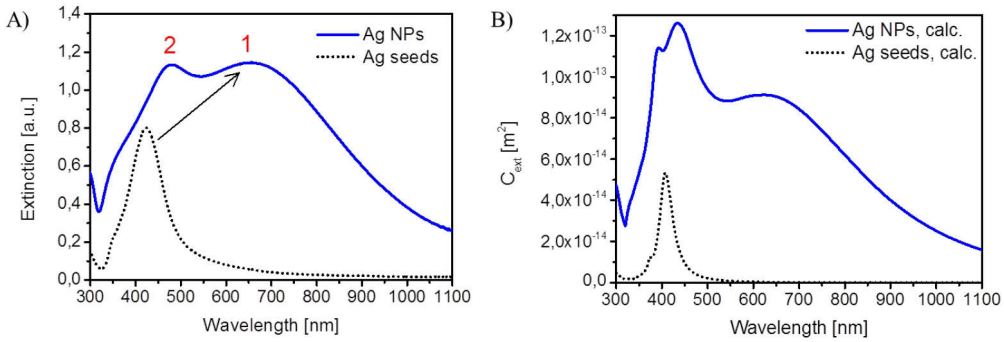

Figure 5.3: A) Extinction spectra of silver seeds (dotted line) and as-prepared silver nanoparticles (line). The dipole mode (1) shifts to lower energies and broadens, while a quadrupole mode (2) appears. B) Calculated extinction spectra of 50 nm and 164 nm silver particles with 9% size deviation.

glycol to produce small monodisperse silver nanoparticles.[69] By adjusting the ratio of seeds to additional silver precursor the silver nanoparticles can be grown to the desired size. Quasi-spherical silver nanoparticles have been obtained via proper modification of this approach. In a first step, 50 nm silver seeds have been synthesized, which have been further grown to 164±15 nm sized silver nanoparticles in a second step by addition of the necessary amount of diamine silver complex (Figure 5.2). Scale-up by a factor of 10 did not have an influence on the quality of the silver nanoparticles, which is mandatory for industrial applications.

The extinction spectra of silver nanoparticles in water are shown in Figure 5.3 and compared with the calculated spectra of silver nanoparticles that have the same diameter with a 9% size standard deviation (as derived from TEM images). There is an obvious red shift and broadening of the dipole LSPR from 420 nm to 640 nm after the nanoparticle growth. Additionally, the quadrupolar LSPR of the as-prepared silver nanoparticles becomes apparent. The calculated spectra show very good correlation of the peak positions with the experimental data. The quadrupole mode peak at 450 nm is slightly overestimated in the calculated spectra. Furthermore, the octupole mode at 400 nm is not distinguishable from the quadrupole mode in the experimental data. According to Figure 5.1C the as-prepared silver nanoparticles should exhibit a huge albedo with a strongly scattering dipolar and quadrupolar mode. Deposition of the as-prepared silver nanoparticles on glass slides allows to measure the scattered (diffuse reflectance and transmittance, $R_{diff} + T_{diff}$) and absorbed light fraction.

The silver nanoparticles have been spin-coated on corning glass (CG) at low speed (500 rpm) to achieve high particle density. Hence, silver nanoparticles were dispersed in ethanol for better spreading during the spin-coating process. No surface modification is needed, as silver particles are sterically stabilized by a polymer (PVP) which has been

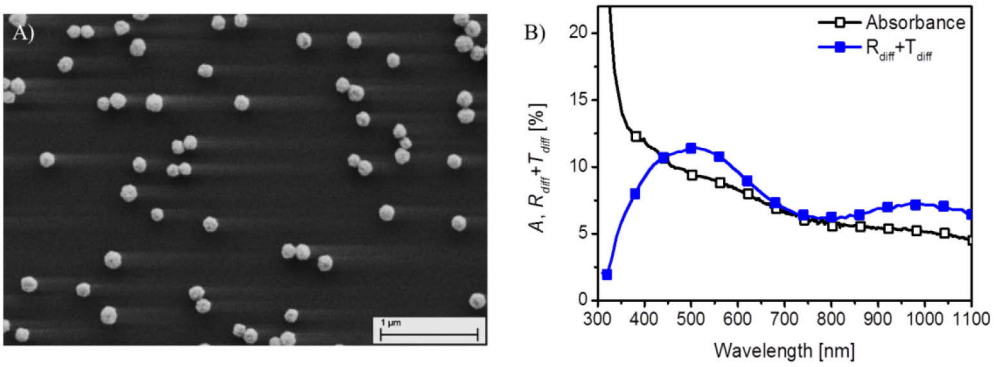

Figure 5.4: A) SEM image of as-prepared silver nanoparticles spin-coated on CG glass. B) Absorbance and (R_{diff} + T_{diff}) spectra measured for the as-prepared silver nanoparticles on CG glass. The absorbed and scattered light fractions contribute equally over a large range of the spectrum.

adsorbed during the synthesis of the silver nanoparticle. This polymer makes the silver nanoparticles excellently redispersable and prevents agglomeration effectively. Figure 5.4A shows an exemplary silver nanoparticle film on CG glass after spin-coating. Image analysis of several SEM images results in a typical coverage of 7.5%. The silver nanoparticles were equally distributed over the whole substrate (5x5 cm) and large agglomerates were absent.

After the spin-coating the absorbance (A) and (R_{diff} + T_{diff}) have been measured for the silver film (Figure 5.4B). The as-prepared silver nanoparticles exhibit equally large absorbed and scattered light fractions over a large spectral range of around 10%. For nanoparticles of such size the scattering should dominate over the absorption. Furthermore, the particle coverage is within the optimal range. Large silver nanoparticles in this size range should have cross sections that are approximately six times larger than their geometrical area (cf. 2.2.3).[243] Hence, a surface coverage of 16.7% is sufficient for maximum scattering efficiencies.

5.1.2 Annealing of silver nanoparticle films

The high parasitic absorption of the as-prepared silver nanoparticles has been unexpected. Possible reasons can be structural and morphological impurities or contaminations like the stabilizing polymers from the synthesis. Annealing can solve these issues and the silver nanoparticle films were heated in a nitrogen atmosphere at 200 °C, 300 °C and 440 °C for 1 – 2 h, respectively. The optical spectra of the resulting nanoparticle films have been measured afterwards and are shown in Figure 5.5. Moreover, SEM images of the silver nanoparticle films have been recorded (Figure 5.6).

The 200 °C annealed sample shows a slight decrease in absorbance and increase in (R_{diff} + T_{diff}) compared to the as-prepared film. The silver nanoparticles remain single

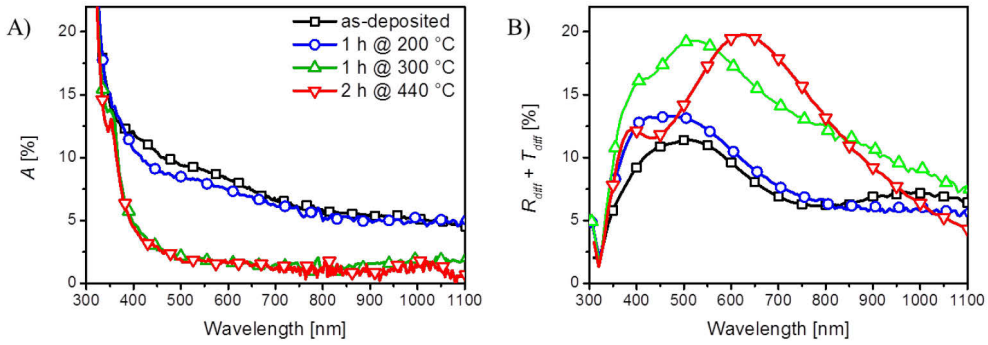

Figure 5.5: A) Absorbance *A* (left) and B) sum of diffuse reflectance and diffuse transmittance ($R_{diff} + T_{diff}$) (right) of silver nanoparticles on CG after annealing at different temperatures. Reprinted from Ott *et al.* [59], © IOP Publishing (2014).

particles, however, some of them are adjoined by each other. Metal nanoparticles in close vicinity couple their LSPR, which causes a broadening in particular for the scattered light of the dipole LSPR.[84, 85] The broadband scattering of the as-prepared and 200 °C annealed sample at higher wavelengths can be attributed to coupling effects. However, this does not completely explain the broadband absorption of the silver nanoparticles. Thermo gravimetric analysis in argon atmosphere has shown that the majority of the total weight loss occurred at 200 °C (Figure 5.7). This can be associated with water desorption and polymer oxidation. Hence, it can be concluded that adsorbed polymers that stabilize the silver nanoparticles do not have an influence on the optical properties.

After annealing at 300 °C for 1 h the optical spectra in Figure 5.5 change remarkably. The absorbance reduces drastically below 2% at wavelengths higher than 500 nm while the

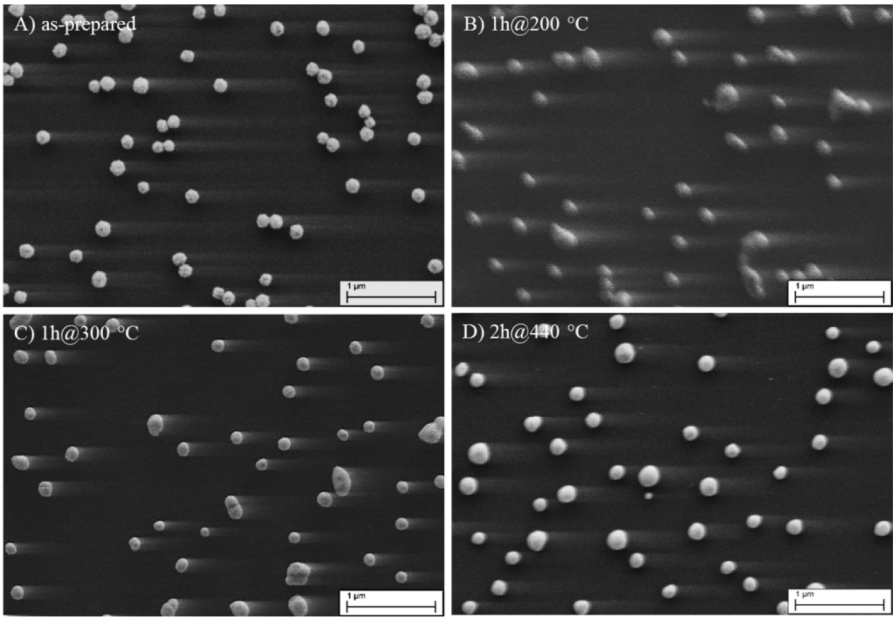

Figure 5.6: SEM images of annealed silver nanoparticles at different temperatures: A) no annealing, B) 1 h at 200 °C, C) 1 h at 300 °C and D) 2 h at 440 °C. Reprinted from Ott *et al.* [59], © IOP Publishing (2014).

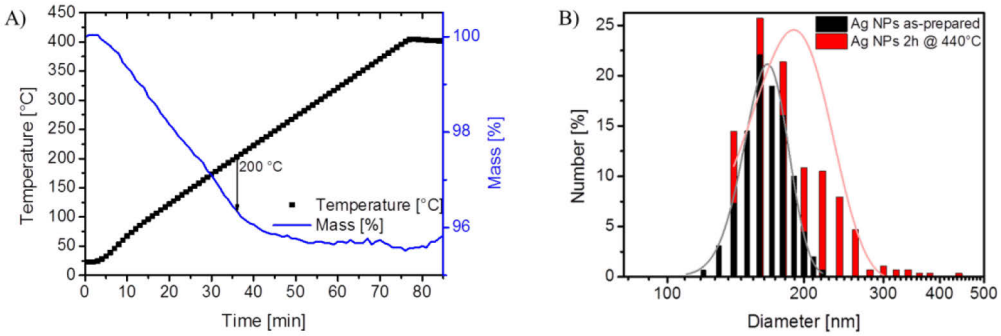

Figure 5.7: A) TGA measurement in argon atmosphere. At 200 °C after 35 min 85% of the total weight loss occurred due to decomposition/desorption of water and stabilizing polymers from the silver nanoparticles. The total weight loss is 4.5%. B) Size distribution of as-prepared silver nanoparticles and after annealing for 2 h at 440 °C. Reprinted from Ott *et al.* [59], © IOP Publishing (2014).

scattered light fraction is enhanced up to 20%. This is accompanied by the appearance of a much more pronounced dipole LSPR peak at 530 nm. The LSPR peak on the substrate is shifted towards higher energies compared to the extinction spectra in solution. This is due to the lower refractive index of air and is consistent with calculations. Neighbouring silver nanoparticles start to coalesce with each other forming single anisotropic particles (Figure 5.6C). It is known that silver nanoparticles exhibit high mobility at elevated temperatures and can coalesce at temperatures far below their melting point.[245-248]

Annealing at the highest applied temperature (440 °C) leads to the formation of isotropic silver nanoparticles due to the reduction of the free surface energy. The nanoparticles that were adjoined after the spin-coating have coalesced and grown to a single silver nanoparticle (Figure 5.6D). As a result the average particle size has increased from 164±15 nm to 190±46 nm with a broader size distribution as shown in Figure 5.7B. Hence, the dipole peak of the light scattered fraction shifts to higher wavelengths around 620 nm. The isotropic shape of the newly formed silver nanoparticles results in a more pronounced peak shape. Furthermore, the single nanoparticles do not couple anymore which reduces the broadband scattering of light in the NIR to IR region. The small absorption peak at 360 nm in Figure 5.5A shows the higher order mode, presumably the octupole mode. The increase in size of the silver nanoparticles leads to a reduction of the surface coverage from 7.5% to 5%. At this silver nanoparticle density the peak at 620 nm has a light scattered fraction of 20%. This value perfectly agrees with the calculations in Figure 5.3B: The dipole peak of a single silver nanoparticle has a cross-section of approximately 10^5 nm^2. This corresponds to four times the geometric area of a single particle and a 5% silver nanoparticle coverage should exhibit a light scattering fraction of 20%. Similar results were obtained by dewetted silver films.[249-252]

5.1.3 Identification of the scattering enhancement process

The morphology change in size and distribution describes well the different peak positions and curve shapes. However, the step-like transition from poorly scattering to highly efficient scattering silver nanoparticles at 300 °C remains unresolved. High magnification TEM and SEM images before and after the annealing process reveal the surface morphology. The as-prepared silver nanoparticles exhibit a rough raspberry-like surface (Figure 5.8A+B) that becomes smooth after the annealing process (Figure 5.8C). As mentioned earlier, the silver nanoparticles reduce at elevated temperatures their free surface energy, which will lead to such a smooth surface. However, such a surface morphology change is unlikely to be the key reason for the reduction in absorbance or increase in scattering. Chen *et al.* have synthesized lumpy silver nanoparticles that scatter light more effectively than smooth silver nanoparticles of similar size.[178] Further, Trügler *et al.* have investigated the absorption and scattering properties of gold nanorods with different surface roughness. They have not seen a significant influence of the surface roughness onto the optically active LSPR.[248]

The surface oxidation state of silver nanoparticles was investigated by X-ray photoelectron spectroscopy (XPS). Every measurement shows the generic binding energy (E_B) shift of 6.0 eV between the $3d_{5/2}$ and $3d_{3/2}$ peaks of silver due to spin-orbit splitting. Each peak has been fitted independently and the results are summarized in Tab. 5.1 and shown in Figure 5.9. The intensity fluctuations in Figure 5.9 are due to abrasion while sample mounting. The as-prepared silver nanoparticles exhibit two surface states that can be attributed to a weak metallic silver peak at E_B = 368.6/374.6 eV and a strong silver oxide (Ag_2O) peak at lower E_B = 367.4/373.4 eV.[247, 253] XPS is a surface sensitive method and the appearance of a pure metallic peak suggests that only a thin Ag_2O layer is formed. This is not very surprising because the colloidal silver particles have been synthesized under ambient conditions and silver is known to oxidize easily on its surface.[247, 254-256] The Ag_2O fraction decreases

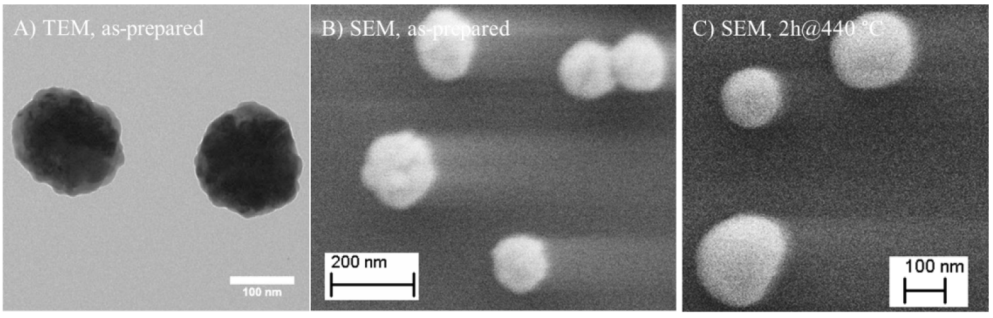

Figure 5.8: High magnification electron microscopy images of as-prepared silver nanoparticles (A+B) and annealed silver nanoparticles at 440 °C for 2 h. Reprinted from Ott *et al.* [59], © IOP Publishing (2014).

Tab. 5.1: E_B of Ag 3d peaks of silver nanoparticles, annealed at different temperatures. The integrated peak areas are shown in brackets. Reprinted from Ott *et al.* [59], © IOP Publishing (2014).

		AgNPs as-prepared	AgNPs 200 °C, 1 h	AgNPs 300 °C, 1 h	AgNPs 440 °C, 2 h
E_B Ag $3d_{5/2}$	Ag_2O	367.4 (86.4%)	367.6 (18.4%)		
Peaks [eV]	Metallic Ag	368.6 (13.6%)	368.1 (81.6%)	368.1 (100%)	368.1 (100%)
E_B Ag $3d_{3/2}$	Ag_2O	373.4 (87.0%)	373.5 (19.1%)		
Peaks [eV]	Metallic Ag	374.6 (13.0%)	374.1 (80.9%)	374.1 (100%)	374.1 (100%)

significantly after annealing at 200 °C and metallic silver becomes the dominant peak. The annealed silver nanoparticle films at 300 °C and above show no Ag_2O peaks, which indicates that the thin Ag_2O layer has been removed completely upon heating (c and d in Figure 5.9). This observation agrees well with the literature that has reported the full Ag_2O decomposition to metallic silver at temperatures above 300 °C.[247, 253, 257]

A surface layer of Ag_2O can have big influences on the overall peak intensity and shape of the optical spectrum of silver particles.[254, 256, 258, 259] Experiments have shown that the absorption at higher wavelengths has been increased due to a Ag_2O shell.[245, 247] The impact of a Ag_2O layer on the near field of a silver nanoparticle was proven by Han *et al.* They have shown that even a sub-monolayer of Ag_2O can decrease the enhancement factor in SERS dramatically, which is very sensible towards the generated local electric fields.[258] Moreover,

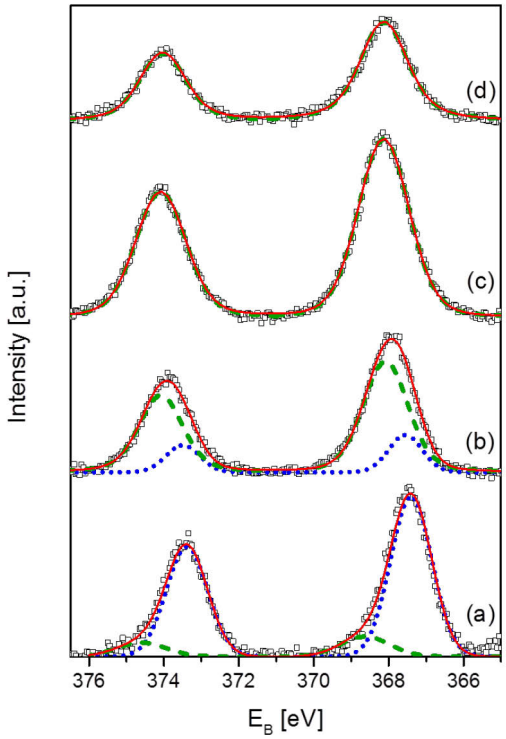

Figure 5.9: XPS spectra of the $3d_{5/2}$ and $3d_{3/2}$ peaks of silver after different annealing temperatures: (a) as-prepared, (b) 1 h at 200 °C, (c) 1 h at 300 °C and (d) 2 h at 440 °C. The open squares are the measured points, while the red straight line marks the cumulative fit. The blue dotted line is the fit curve of Ag_2O and the green dashed line the fit curve of metallic silver. Reprinted from Ott *et al.* [59], © IOP Publishing (2014).

Ag_2O layers have an influence on the solar cell efficiencies, which was shown experimentally and in theory. Calculations of Akimov and Koh demonstrated that efficiency enhancements of solar cells via silver nanoparticles can be quickly negated if there is a Ag_2O shell present. The effect has been explained by stronger parasitic absorption of the Ag_2O.[260] Furthermore, silver films that exhibit a thin oxide layer have shown to decrease the scattering compared to the pure metallic silver films.[261] Yang *et al.* have found also that silver nanoparticles embedded in a solar cell get tarnished over time, which leads to degradation of the silver nanoparticles and eventually of the solar cell.[183] Hence, removal of the Ag_2O shell is crucial to maintain low parasitic absorption. The concurrent decrease in absorption, increase in scattering and removal of Ag_2O at 300 °C match this finding very well. Therefore, the step-like transition of the increased scattering behaviour of the silver nanoparticle films is attributed to the Ag_2O decomposition.

Further interest exists in the particle structure itself, as XPS can only analyse the nanoparticle surface. Accordingly, X-ray diffraction (XRD) of each sample has been measured. Figure 5.10 shows diffraction peaks at $2\theta = 38.2°$ and $2\theta = 44.3°$ that correspond to metallic face centred-cubic (fcc) silver. No diffraction peaks for Ag_2O have been found, which proves that indeed only a thin oxide layer on the surface of the silver nanoparticles exists. The XRD measurements further give information about the crystallinity of the silver nanoparticles. As seen in Figure 5.10, the silver (111) peak at $2\theta = 38.2°$ becomes sharper with higher annealing temperature. Moreover, the silver (200) peak at $2\theta = 44.3°$ appears and becomes more prominent.[246, 257, 262]

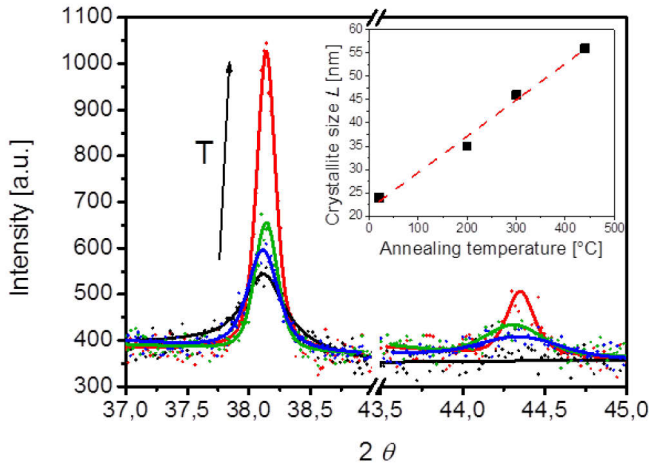

Figure 5.10: XRD measurements of silver nanoparticle films annealed at different temperatures: as-prepared (black), 1 h at 200 °C (blue), 1 h at 300 °C (green) and 2 h at 440 °C (red). The peaks correspond to fcc silver with (111) at $2\theta = 38.2°$ and (200) at $2\theta = 44.3°$. The inset shows a linear dependency of the crystallite size, which has been derived from the Scherrer equation. Reprinted from Ott *et al.* [59], © IOP Publishing (2014).

The crystallite size L of silver nanoparticles can be calculated via the Scherrer equation:

$$\Delta = \frac{K\lambda}{L\cos\theta} \tag{5.1}$$

where K is a shape factor with a standard value assuming 0.9 and Δ is the FWHM in radians of a certain peak at a given Bragg angle 2θ. The inset of Figure 5.10 demonstrates that with increasing annealing temperatures the crystallite sizes increase in a linear dependency. This is caused by a higher mobility of silver atoms at higher temperatures and leads to restructuring inside the silver nanoparticles.[263, 264] The restructuring mechanism and crystallite growth can be attributed to grain boundary diffusion of the silver atoms.[245, 263] Larger crystallites will eventually lead to less grain boundaries, which enlarges the electron mean free path length and thereby reduces the Ohmic damping in the metal. This can enhance the plasmonic scattering efficiency and has been shown for polycrystalline films and dewetted samples.[173, 263, 264] However, the linear increase in crystallite size does not explain well the step-like transition from high absorption/low scattering to low absorption/high scattering at temperatures above 200 °C. Thus, it is more likely that the decomposition of the native Ag_2O shell has a bigger influence on the improved optical properties of the silver nanoparticle films than the crystallinity of the silver nanoparticles.

5.1.4 Silver nanoparticle incorporation in an amorphous silica absorber

To elucidate the light trapping ability of the at 440 °C annealed silver nanoparticles a 230 nm thin amorphous silicon (a-Si) film has been evaporated on top of the silver nanoparticle film. This film has been compared with a 230 nm thin a-Si film on bare CG glass. The presence of

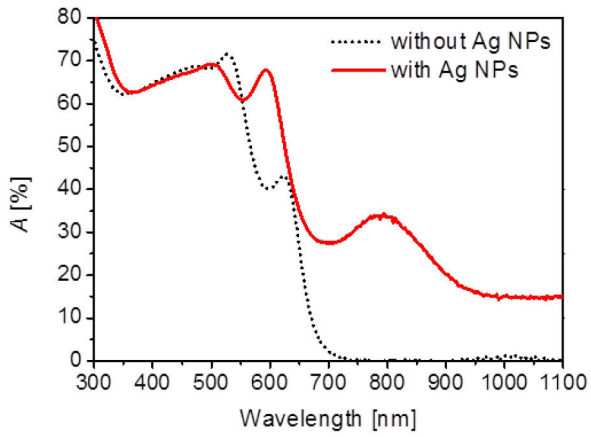

Figure 5.11: Absorbance by a 230 nm thin a-Si film with (straight line) and without (dotted line) silver nanoparticles on CG substrate. The silver nanoparticle films shows strong light trapping and increased absorption, in particular in the NIR and IR region. Reprinted from Ott *et al.* [59], © IOP Publishing (2014).

silver nanoparticles increases the absorbance strongly below energies of the band edge of a-Si (650 nm). This indicates excellent light trapping properties of the silver nanoparticle film. The trapped light is absorbed in the silver nanoparticles, CG glass or at defects of the thin a-Si film. Furthermore, a pronounced peak at 790 nm is generated, which is likely the dipole LSPR peak that has been red-shifted due to the increased refractive index of silicon. The silver nanoparticle film with 5% surface coverage shows light trapping of 20 – 30% in the IR region and might be enhanced further if the particle density is adjusted properly.

5.2 Plasmonic enhancement of perovskite solar cells by gold nanorods

Annealing at high temperature can be in some cases impractical, e.g. if the absorber material is unstable (like perovskites) and the sell architecture does not allow for pre-treatment. Perovskites in general have the crystal structure ABX_3 and the most common perovskite absorber material is currently methylammonium lead trihalide ($CH_3NH_3PbX_3$, X = I^-, Br^-, Cl^-). Perovskite solar cells have experienced a boosted interest in the community. The first cell that has implemented perovskites as sensitizer material reported an efficiency of 3.8% in 2009.[265] In only 5 years the efficiency could be enhanced up to 19.3%, which makes the perovskite solar cells the fastest advancing solar cell technology.[266] This is due to several advantages that perovskite solar cells offer: (i) the materials that are used are earth abundant; (ii) the exciton binding energy is very low at room temperature (~2 meV), which enables easy charge separation to free electrons and holes;[267] (iii) the recombination is strongly suppressed[268] and (iv) the electron-hole diffusion length exceeds 1 µm.[269] The bandgap is dependent on the organic and halide ligands and can be tuned between 1.48 – 2.23 eV.[270] This corresponds approximately to light at a wavelength of 800 nm and there is still improvement for lower energy bandgap perovskite materials that can absorb light in the NIR region.

5.2.1 Properties of the gold nanorods

Plasmonic light trapping might enhance the solar cell efficiency further. The previous section has shown that silver nanoparticles have drawbacks regarding their chemical stability. Hence, tuneable gold nanorods have been synthesized and implemented in the perovskite solar cell. The nanoparticles synthesized need to be active in the red wavelength region and should be sufficiently large to avoid parasitic absorption of light. By adjusting the ratio of growth solution to gold seeds, 94±12 nm x 63±9 nm large gold nanorods have been prepared. Direct

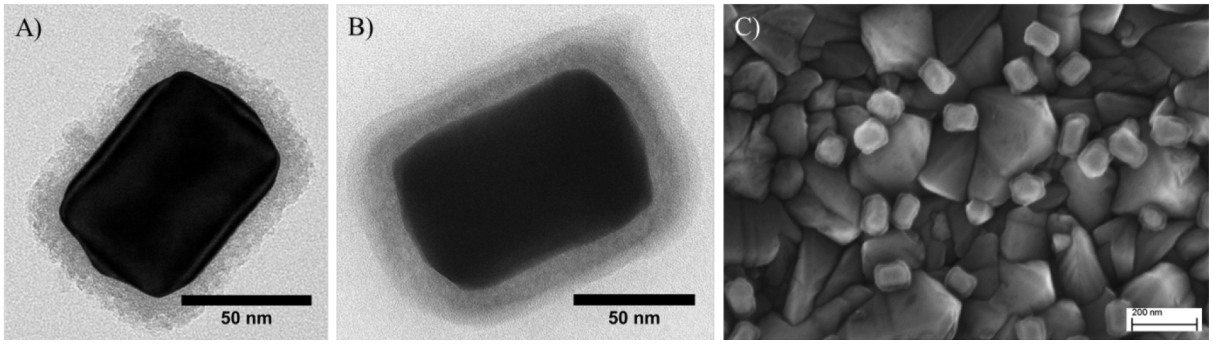

Figure 5.12: TEM images of a gold nanorod with the first mesoporous silica shell (A) and a second dense silica shell (B). The size of nanorods is 94±12 nm x 63±9 nm with a 15 nm silica shell as derived from TEM images. C) SEM image of gold nanorods distributed homogeneously on a FTO substrate via spin coating. The particle density on the substrate is 11.8%.

contact of the gold nanoparticles with the perovskite must be avoided as they can form recombination centres in the absorber layer and reduce the performance of the solar cell. Therefore, the gold nanorods have been coated with a silica shell as mentioned in chapter 4.1.2. Single silica coating results in a mesoporous silica shell due to the soft template CTAB that stabilizes initially the gold nanorods in solution. This mesoporous shell cannot protect effectively the gold nanorods yet. It has been shown that at elevated temperatures gold can leach through the small channels in the silica shell. For example, 30% of gold has been leached from porous core-shell nanoparticles after 15 h at 80 °C.[271] To avoid gold leaching, a second dense silica shell has been synthesized under Stöber conditions (cf. 4.1.1). The silica shell has been 15±1 nm thick (Figure 5.12B) and provided sufficient protection from gold leaching as could be shown by XPS analysis (Figure 5.13). Gold nanoparticles have been spin-coated onto a substrate and were covered by an absorber that was 450 nm thick. Upon heating no gold has been leached until an annealing temperature of 440 °C. For samples that have been annealed 30 min at 610 °C gold peaks became apparent in the XPS at a binding energy $E_B(\mathrm{Au4f_{7/2}}) = 84.0$ eV and $E_B(\mathrm{Au4f_{5/2}}) = 87.7$ eV.[272] Hence, gold nanoparticles coated

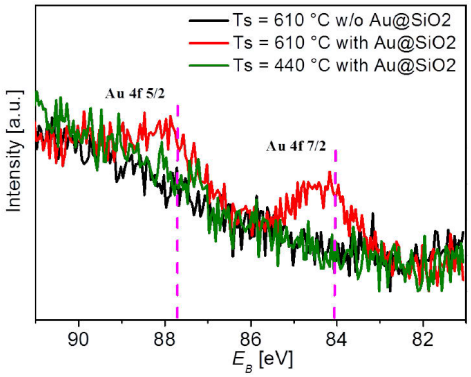

Figure 5.13: XPS of gold nanorods covered with a double silica shell and a 450 nm thick absorber. No gold peaks have been observed until annealing for 30 min at 610 °C with typical binding energies E_B for gold.[272]

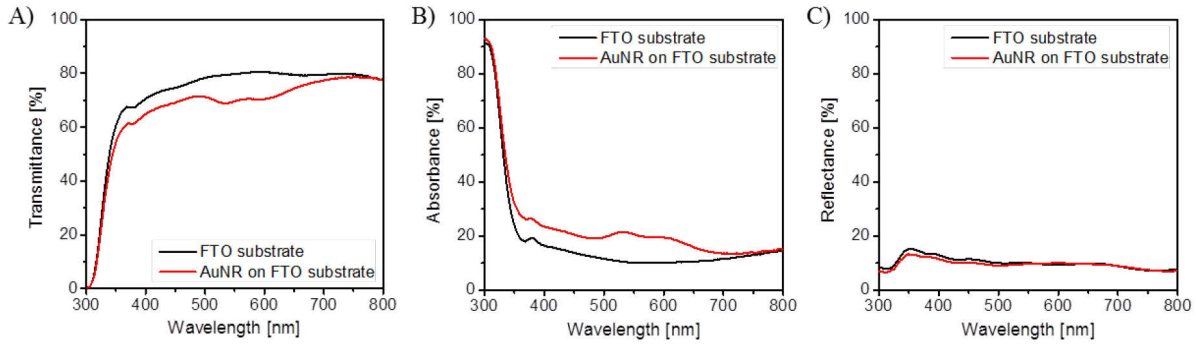

Figure 5.14: Optical properties of the FTO substrate with and without gold nanorods (11.8% coverage). A) Transmittance, B) absorbance and C) reflectance (backward scattering).

with a double-silica shell are substantially more stable versus gold leaching than a single mesoporous silica shell.

The gold nanorods have been spin-coated onto a fluorine-doped tin oxide (FTO) substrate and the optical properties have been measured. Figure 5.14A,B shows that the LSPR peaks are at $\lambda_t = 533$ nm and $\lambda_l = 612$ nm. The wavelength region of interest for plasmonic effects in perovskite solar cells is 550 – 800 nm. Via incorporation in the solar cell the refractive index will be larger and should shift the LSPR peaks to the appropriate position (cf. 3.3). As has been mentioned before, parasitic absorption should be avoided. The transmittance has been decreased slightly by 5 – 10% at a coverage of gold nanorods of 11.8%, as has been derived from SEM images (Figure 5.12C). More importantly, the nanoparticles should not scatter the incident light backwards (away from the absorber). Figure 5.14C shows that the backward scattering has not been increased after spin-coating of the gold nanorods onto the FTO substrate.

5.2.2 Solar cell design and performance

The solar cell preparation and the investigation of its performance have been executed by Yang Liu from Helmholtz Zentrum Berlin. Figure 5.15 shows the principle design of the single junction perovskite solar cell. The substrate consists of transparent glass with a conductive layer of FTO. A titanium dioxide (TiO_2) layer has been coated via spray pyrolysis on top which acted as an electron transport layer and as a hole blocking layer to separate the charges. Then the gold nanoparticles have been spin-coated. The active perovskite absorber layer has been deposited via a solution-based method similar to Jeon *et al.*[273] Spiro-OMeTAD ($C_{81}H_{68}N_4O_8$) has an extended conjugated π-electron-system and was spin-coated onto the absorber layer, which was used as a hole transporting layer. Finally, gold has been thermally evaporated on top as a back contact electrode.

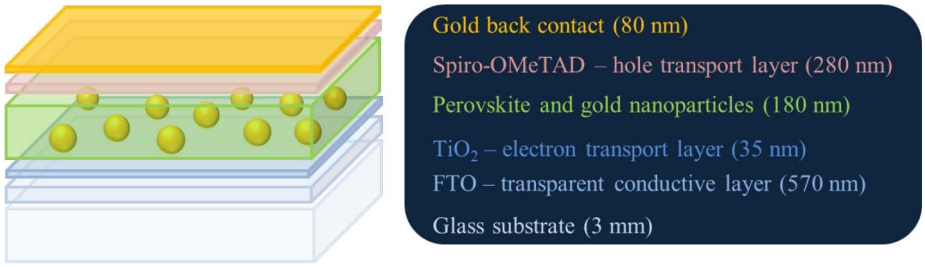

Figure 5.15: Design of a single junction perovskite solar cell with embedded gold nanoparticles in the absorber layer.

As has been shown in Figure 5.14B and C, the substrate with the gold nanoparticles shows low absorption and reflection. After spin-coating of the perovskite layer the absorption has been increased significantly (Figure 5.16A). Further, it has been shown that the incorporation of the gold nanoparticles increases the absorption in the range of 550 – 1000 nm. This is because of the LSPR that have been red-shifted due to the increased refractive index (~2.4 – 2.7).[274] In this wavelength region the increase in absorption is 5 – 8%, which is equivalent to the increase in absorption on the pure FTO after gold nanoparticle deposition (Figure 5.14B).

After the preparation of the solar cell the external quantum efficiency (EQE) has been measured, which is the ratio of the collected number of carriers to the number of photons of a given energy incident on the solar cell. It can be seen in Figure 5.16B that the EQE has been increased over the whole spectral range by 5 – 10%. This is in particular true for the plasmonic active region with a new shape in the EQE curve. Hence, the gold nanorods are able to increase the generation of carriers in the solar cell. It is unclear why the EQE curve is also increased in the UV and blue light region. This could be an effect of light trapping via structuring effects that are non-plasmonic nature but caused by the gold nanorods, which

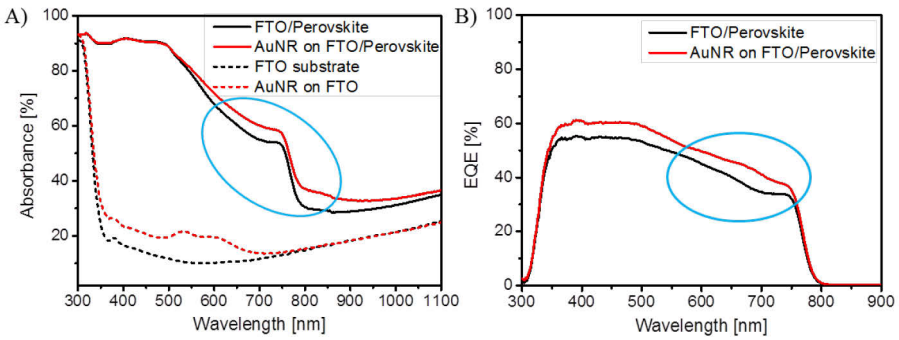

Figure 5.16: A) LSPR absorption of the gold nanorods occurs at a wavelength of 550 – 900 nm with a sharp step at 800 nm that corresponds to the band gap of perovskite. B) The solar cell with gold nanorods shows an enhanced EQE over the whole spectral range with the strongest effect and new curve shape at the plasmonic active wavelength region.

Tab. 5.2: Comparison of the parameters of the reference cell and the solar cell with gold nanorods. In particular the short-circuit current has been increased after implementation of the gold nanorods.

	Perovskite (average)	Perovskite (best[§])	Perovskite + AuNR (average)	Perovskite + AuNR (best[§])
V_{OC} [V]	0.96	0.97	0.95	0.96
I_{SC} [mA·cm^{-2}]	7.3	7.2	10.4	10.8
FF [%]	58.9	64.9	59.7	61.0
η [%]	4.2	4.5	5.8	6.3

pattern the absorber layer (cf. 2.4). As has been mentioned in the beginning, perovskites have a bandgap at ~800 nm. Therefore, no carriers are generated at lower photon energies. The absorption at higher wavelengths in Figure 5.16A (> 800 nm) is likely due to the first layers of FTO/TiO_2/gold nanorods.

The EQE of the prepared solar cells does not account for such reflected and absorbed light (i.e. "external"). The internal quantum efficiency (IQE), hence, might be much higher and may approaches close to 100%. The efficiency of the solar cell is defined as:

$$\eta = \frac{P_{max}}{P_{in}} = \frac{V_{OC} I_{SC} FF}{P_{in}} \tag{5.2}$$

with P_{max} the maximum power generated by the solar cell, P_{in} the input power of the light source, V_{OC} the open-circuit voltage, I_{SC} the short-circuit current and *FF* the fill factor. The values that determine P_{max} can be obtained from the *I-V* curve (cf. 8.3.6, Tab. 5.2) and the efficiencies have been calculated for the reference solar cell and the solar cell with gold nanorods embedded in the perovskite absorber. The average efficiency of the perovskite solar cell has been increased from 4.2% to 5.8% after implementation of the gold nanorods. The best solar cell[§] that has been fabricated here achieved an efficiency of 6.3%. The open-circuit voltage V_{OC} that determines the highest voltage possible and the fill factor *FF* that is influenced among others by the effect of series resistance are constant for both types of solar cells. The increase in efficiency stems solely from the increase of the short-circuit current, which is a measure of light generated carriers. Therefore, gold nanorods have indeed helped to increase the effective light harvesting in the perovskite absorber material without negative effects like shunting. The experiments show that further enhancement of the performance can be obtained by the implementation of plasmonic metal nanoparticles in perovskite solar cells.

[§] The "best" solar cell is referred as the solar cell that showed the highest efficiency η.

5.3 Outlook for metal nanoparticles for light-trapping in solar cells

Light trapping with plasmonic metal nanoparticles can increase the light harvesting dramatically. This has been shown for large silver nanoparticles generically and for gold nanorods in an actual device. Plasmonic solar cells show great potential, however, morphology and chemical composition need to be considered carefully as it became evident for silver nanoparticles. Annealing of silver nanoparticles can be impracticable if e.g. the solar cell becomes altered, which the case for many absorber materials is. Furthermore, silver nanoparticles may also become tarnished over time.[183] Though silver is superior regarding its optical properties, gold nanorods have shown to be a good alternative that are able to increase the light harvesting as well. In particular, gold nanoparticles offer high chemical stability and control over shape. Gold nanorods e.g. have tuneable LSPRs over a broad spectral range via their aspect ratio.

In addition, it could be shown that the wet chemical approach offers several advantages. Metal nanoparticles can be protected and isolated from the absorber by coating with silica. Expensive top-down processes on the other hand would need a new insulating layer to avoid direct contact, which causes additional light absorption and reflection. A separated production process allows for high control over size and shape and over surface coverage via spin-coating, which make the wet chemical approach promising for applications in thin film photovoltaics.

6. Anisotropic Janus-dumbbells as carrier system for plasmonic metal nanoparticles

In chapter 2.1.2 stabilization of metal nanoparticles was reviewed and carrier systems have been introduced. Here, an anisotropic carrier system is introduced that has additionally Janus properties, i.e. a particle that has at least two varying physical or chemical properties on its surface. The carrier system shows high diversity and switchable tuning of its chemical nature and applicability.

The anisotropy and Janus properties are introduced by phase separation during the polymerization of spherical polystyrene particles to dumbbell-shaped particles. The Janus character allows for modification of a single lobe only. The particles exhibit new properties and dipolar or amphiphilic character. Furthermore, the modified surface allows for *in-situ* metal nanoparticle deposition, e.g. gold or platinum. Gold nanoparticles could be subsequently grown to a semi-shell with altered plasmonic properties via size and coupling effects. By altering the phase separation step the Janus properties have vanished and the carrier system has been completely decorated with gold nanoparticles. Platinum nanoparticles that react with hydrogen peroxide were investigated on self-propelling features.

6.1 Synthesis, modification and characterization of Janus dumbbells

Dumbbell shaped nanoparticles have been prepared by the phase-separation technique of Park *et al.* that produces large amounts of highly monodisperse colloids.[130] Figure 6.1 shows schematically the general approach to synthesize Janus dumbbells and its modification process. In a first step spherical core-shell particles are synthesized via seeded emulsion polymerization. These particles have a hydrophobic polystyrene (PS) core and a hybrid copolymer shell consisting of PS and 3-methacryloxypropyltrimethoxysilane (MPS). The inner PS core is not cross-linked, which allows for swelling of the core with additional styrene monomers by phase-separation. The swelling is restricted due to the outer copolymer layer (PS-MPS), which will lead eventually to a bulge with continuous styrene polymerization in this bulge. By adjusting the proper amount of monomer, Janus dumbbell-shaped particles were formed, having the initial hybrid PS-MPS copolymer on one lobe and a pure PS part on the newly formed lobe. These particles itself have Janus type character (step three in Figure 6.1) and can be further functionalized with e.g. metal nanoparticles as was shown before.[133, 275]

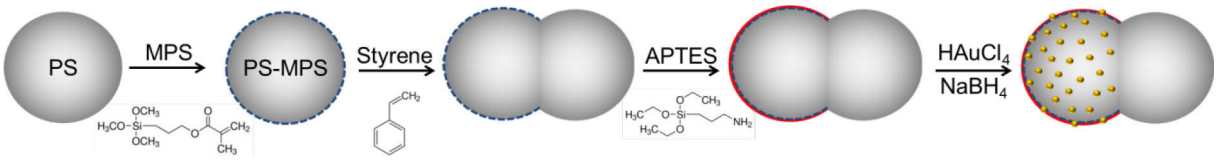

Figure 6.1: Scheme of synthesis approach of Janus dumbbells and its modification, e.g. amine functionalization and *in-situ* grafting of gold nanoparticles.

Before the dumbbell shaped particles have been investigated, the spherical hybrid PS-MPS particles were characterized. The copolymer layer exhibits negative charges due to free silanol groups provided by the MPS that can undergo hydrolyzation and condensation of the three remaining methoxy groups similar to TEOS and APTES. These PS-MPS particles have a negative zeta potential in a large range of pH values (Figure 6.2A). Due to the free silanol groups silane chemistry is possible and allows for surface modifications, e.g. amine functionalization via the silane reagent APTES. After amine functionalization the zeta potential shows much stronger pH dependency with values ranging from -70 mV for high pH to +60 mV at low pH values. This concludes that a large majority of the silanol groups has successfully reacted with the APTES reagent. Free primary amine groups have been grafted on the surface that become protonated at low pH values (Figure 6.2A). As seen in Figure 6.2B, the particles become highly unstable at pH around 7, which leads to non-reversible aggregation due to the lack of sufficient repulsive electrostatic charges (cf. chapter 2.1.2).

A similar behaviour has been observed for dumbbell shaped particles. The newly formed PS lobe is stabilized with small amounts of styrene sulfonate, while the former PS-MPS lobe possesses silanol groups from the MPS copolymer after hydrolysis in water. The PS-MPS-PS dumbbells are therefore negatively charged (Figure 6.3B). After amine functionalization via the silane reagent APTES the modified dumbbells show a stronger zeta potential pH dependency as well. The amine groups that are protonated at lower pH values

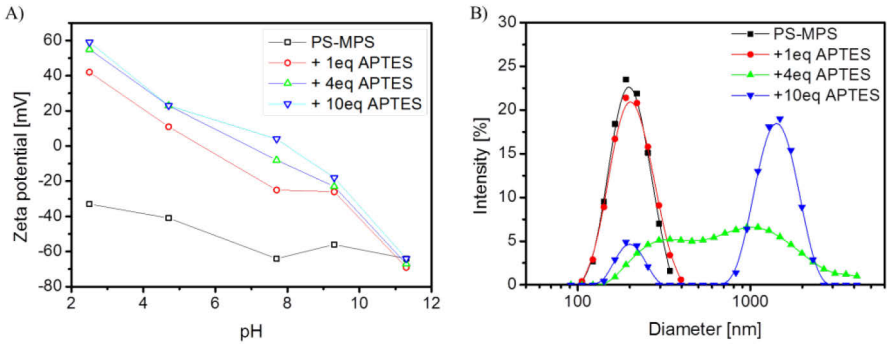

Figure 6.2: A) Zeta potential graph of spherical PS-MPS particles and the amine functionalized particles via APTES reagent. The modified particles show much stronger pH dependency. B) Size analysis of spherical PS-MPS and APTES functionalized particles at pH 2.3. More APTES reagent leads to stronger aggregation.

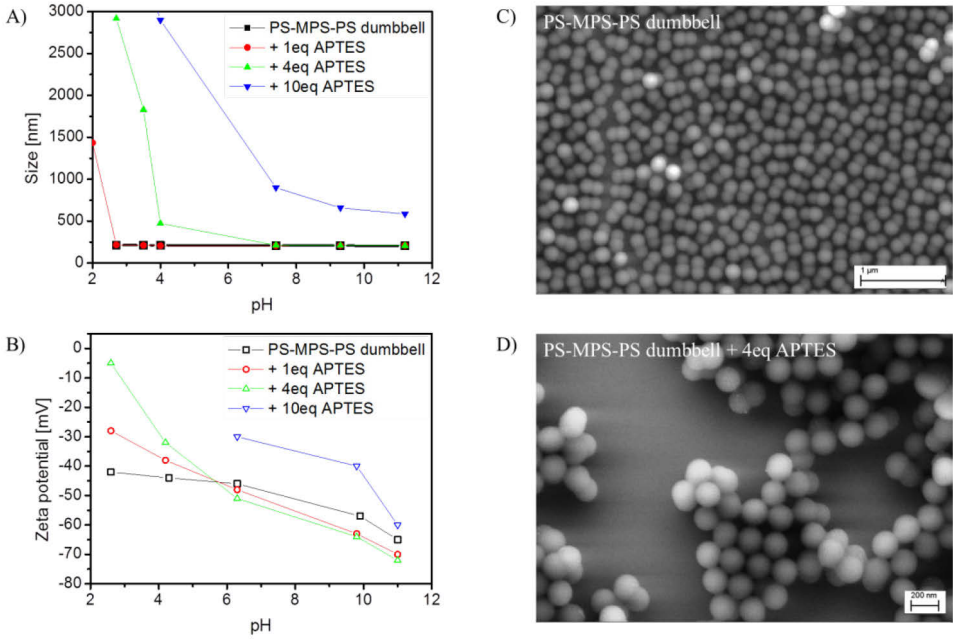

Figure 6.3: A) Size and B) zeta potential measurements[**] via DLS that show the aggregation behaviour of dumbbells functionalized with different amounts of APTES with changing pH. SEM images show as well the aggregation of dumbbells functionalized with an amine group (D) compared to pure PS-MPS-PS dumbbells (C).

reduce the absolute value of the zeta potential leading to aggregation much earlier. As expected, by using more APTES, aggregation is induced at even higher pH values. However, the zeta potential never reaches positive values as only half of the particle surface can be covered with amine groups. This is a strong indication of the Janus character present on this colloidal system. The aggregation due to the dipolar character of the Janus dumbbells can be also seen in SEM images. A monolayer film of dumbbell shaped particles was formed at a 1-butanol / water interface (pH 7) following a literature report.[276] Prior amine functionalization the particles are lying flat on the substrate whereas the amine-functionalized particles easily aggregate on the substrate, mostly standing upright (Figure 6.3C and D).

6.2 Metal nanoparticle deposition

Metal nanoparticles can be well stabilized and have an affinity towards amine reagents. Gold nanoparticles have been generated by the reduction of the precursor $HAuCl_4$ using different reducing agents, i.e. sodium borohydride ($NaBH_4$) or L-ascorbic acid (AA). At first the spherical system has been used to optimize the reaction conditions for the gold nanoparticle reduction. Excess gold nanoparticles have been separated via centrifugation after the grafting step. In the first approach gold nanoparticles have been synthesized via $NaBH_4$ reduction and

[**] Zeta potentials could not be measured for the sample with 10 equivalent APTES at pH below 6 due to the aggregation in the cell.

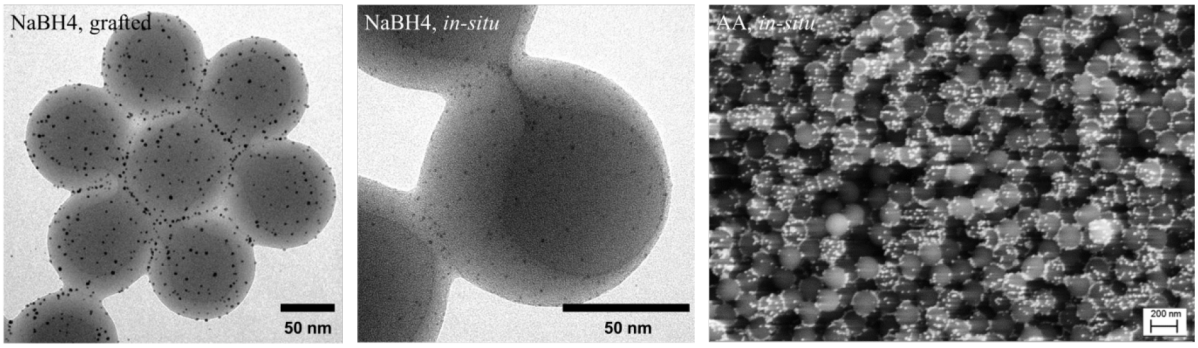

Figure 6.4: TEM images and SEM image (right) of spherical amine functionalized PS-MPS carrier systems with gold nanoparticles: $NaBH_4$ reduced gold nanoparticles that have been grafted after nanoparticle synthesis (right), *in-situ* reduction of the gold precursor by $NaBH_4$ (middle) and *in-situ* reduction by AA (right).

then grafted in a second step onto the PS-MPS particles functionalized with APTES. A second approach is the *in-situ* reduction of $HAuCl_4$ in the presence of the carrier system. From TEM images in Figure 6.4A+B the influence of the presence of the carrier system is shown. The average size of gold nanoparticles without the PS-MPS particles is 6 nm, whereas the *in-situ* reaction results in 2 nm gold nanoparticles. Smaller nanoparticles, in particular in this size range, have a much larger surface free energy. This indicates that the presence of the amine functionalized PS-MPS particles stabilizes the gold particles more effectively. This becomes even clearer when reducing the gold precursor with AA. Without the carrier system the metal nanoparticles form large aggregates and precipitate quickly. In the presence of the spherical PS-MPS particles 20 nm sized gold nanoparticles are attached to the carrier system and have been well stabilized (Figure 6.4 right). It is worth mentioning that no nanoparticles have been grafted on the pure PS-MPS particles (no amine functionalization).

As shown in Figure 6.1, the dumbbell carrier system should only exhibit amine functionalization on one lobe. Due to the affinity towards the metal nanoparticles only this lobe should be grafted with the metal nanoparticles. Gold and platinum particles have been

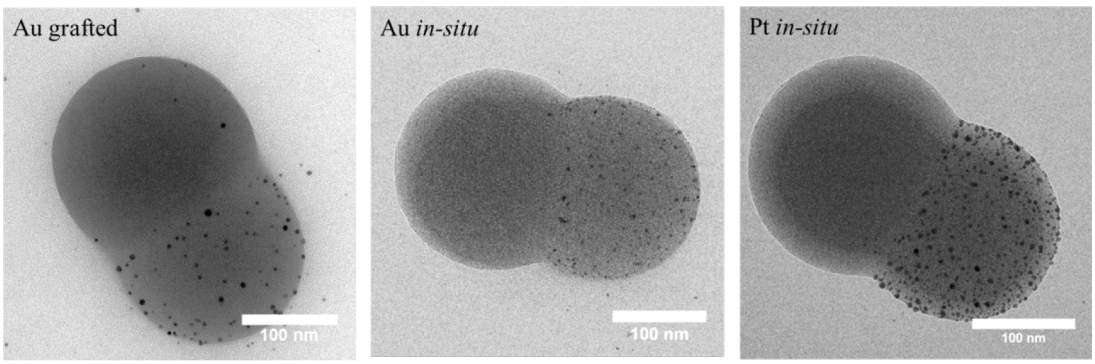

Figure 6.5: TEM images of amine functionalized dumbbell shaped PS-MPS-PS particles with gold (left and middle) and platinum (right) nanoparticles grafted on one lobe only due to the Janus character.

generated via the reduction of $HAuCl_4$ or K_2PtCl_4, respectively, *in-situ* by $NaBH_4$ with the amine functionalized PS-MPS-PS dumbbells present. Indeed, only one side of the dumbbell shaped particles shows metal nanoparticle decoration (Figure 6.5). Again, no metal nanoparticles have been grafted on the dumbbell shaped particles before amine functionalization. Gold nanoparticles have been additionally synthesized prior grafting via the reduction of $HAuCl_4$ by $NaBH_4$ and adsorbed on the carrier system. The nanoparticle sizes follow the same trend as for the spherical system, i.e. 5 nm for the subsequently grafted gold nanoparticles and 2 nm for the *in-situ* reduced gold nanoparticles. *In-situ* reduced platinum nanoparticles exhibit an average diameter of 6 nm.

6.3 Gold nanoparticle growth to semi-spherical and capsule shaped shells

As seen in Figure 6.4, the nanoparticle size distribution is more homogenous, dense and more equally distributed for the *in-situ* reduced metal nanoparticles. Therefore, these particle systems were selected for further growth of the gold nanoparticles. For the growth of gold shells the reaction conditions must be carefully adjusted to inhibit gold seed formation and slow growth on the pre-existing gold nanoparticles. One method is the reduction of $HAuCl_4$ from Au(III) to Au(I) by formaldehyde in potassium carbonate solution. Subsequently, the colourless Au(I) ions get reduced on the gold nanoparticle surface only, which allows for controlled gold nanoparticle growth. Similarly, micron-sized dimer particles have been functionalized with a metal semi-shell before.[133, 275]

The gold nanoparticles grew stepwise by repetitive addition of the growth solution and cleaning from 2 nm to 6 nm, 14 nm and finally 25 nm. As seen in Figure 6.6, the gold nanoparticles remain isolated until the last growth step. The 25 nm sized gold nanoparticles are connected and form a semi-shell around the amine functionalized lobe. However, there are still holes present in this shell which is because of the low amount of initial gold seeds. The presumably reason is that the amount of the copolymer MPS is too low. The mass ratio of

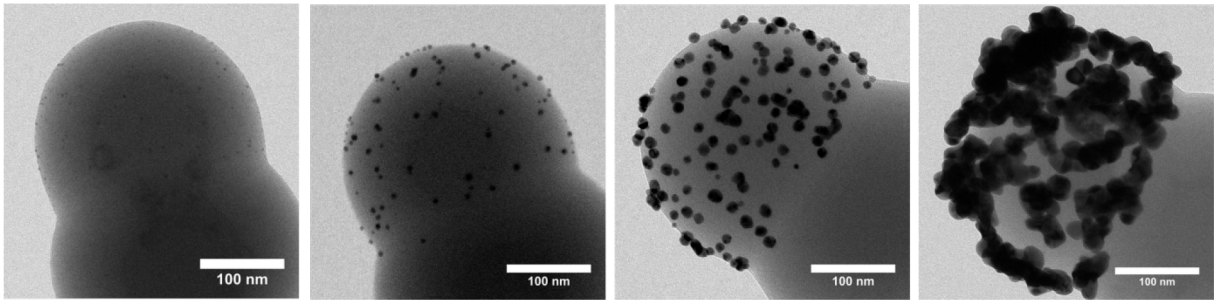

Figure 6.6: Subsequent growth of gold nanoparticles from left to right with 2 nm, 6 nm, 14 nm and 25 nm gold nanoparticles. No secondary particles are generated and a holey semi-shell is formed for the largest gold nanoparticles.

MPS : styrene in the copolymer shell is 1 : 10. Hence, only a small portion of free silanol groups and deductively amine groups are formed. The low amount of amine groups results in too few nucleation sites for gold seeds to grow a homogenous semi-shell.

Consequently dumbbell particles with higher MPS : styrene ratio (1 : 3) have been synthesized and functionalized with APTES. Figure 6.7 shows the resulting PS-MPS-PS particles with *in-situ* grafted gold nanoparticles and their growth. Much more gold nanoparticles have been decorated on the carrier system indeed; however, the overall result has been somewhat unexpected. The consequence of using more MPS is a stiffer shell. The copolymer layer consists of a higher fraction of silica due to hydrolyzation and condensation of the remaining methoxy groups of the MPS. The swelling and polymerization of additional styrene most likely leads to a less pronounced bulge, forming rather capsules than dumbbell shaped particles. Furthermore, the stiffness of the copolymer layer must have prevented to effectively burst open on one side of the spherical particle. This results in a stretched PS-MPS surface of the newly formed capsule and the amine functionalization and gold nanoparticle decoration occurs on the whole particle. Nonetheless, one lobe of the capsule shaped particles exhibits more gold nanoparticles than the other one. This can be seen in particular for the third growth step in Figure 6.7. In summary the increase of the amount of MPS used for the copolymer layer forms capsule shaped particles that allow for a more dense amine and gold nanoparticle decoration. The gold nanoparticles have been grown stepwise from initially 2 nm to 5 nm, 9 nm and 15 nm that lead eventually to a full gold nanoshell.

The particles have been investigated on their optical properties. Due to strong scattering of the carrier system extinction spectra (UV/Vis) are impractical. The particles have been deposited onto a glass substrate and the transmission and reflectance were measured by an integrating sphere (cf. 8.3.1, Figure 8.1). The LSPR of gold nanoshells are very sensitive towards the inner core diameter and the shell thickness.[277] A larger carrier system leads to a red-shift of the LSPR and higher order modes can appear. This behaviour is similar to gold

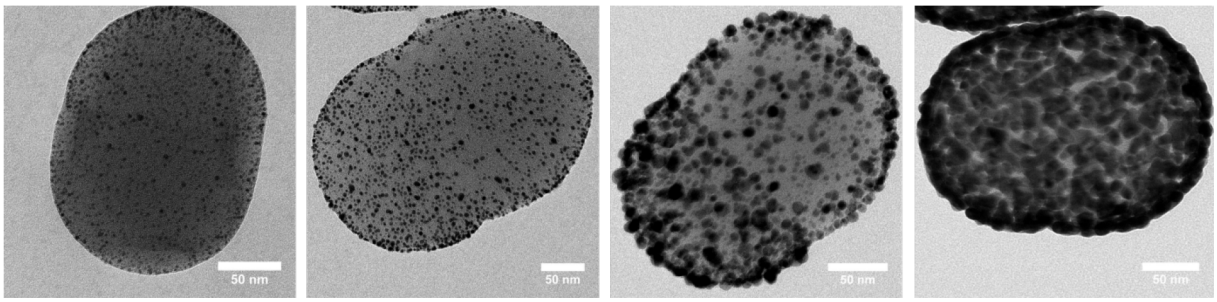

Figure 6.7: Subsequent growth of gold nanoparticles from left to right with 2 nm, 5 nm, 9 nm and 15 nm gold nanoparticles. The largest gold nanoparticles form a full gold shell around the capsule shaped carrier system.

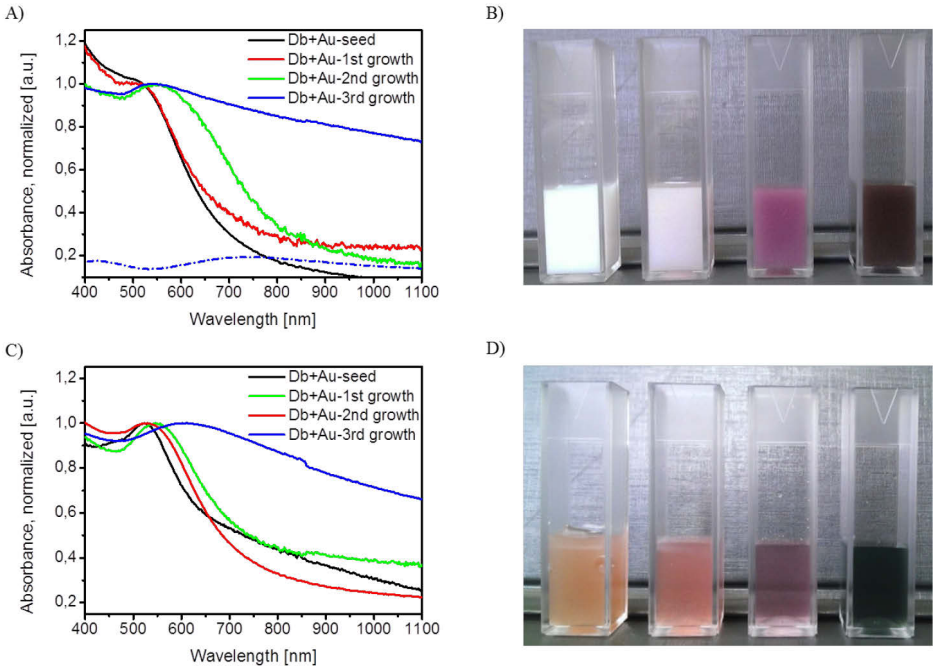

Figure 6.8: Normalized absorbance spectra of A) semi-shell gold nanoparticles and C) gold capsules. The solutions become stronger coloured and more bluish with respective gold nanoparticle growth as can be seen from the photographs (B and D).

core nanoparticles (cf. 3.1). Contrary, a thicker nanoshell leads to a blue-shift of the LSPR with broadening. This has been verified by Mie calculations and experiments.[278] High control of the surface morphology with elaborated surface chemistry has shown that LSPR of gold nanoshells can be expected between 500 – 1000 nm. However, even slight inhomogeneity or ruptures in the nanoshell lead to broadening of the peaks.[278]

A gold semi-shell should provide the same LSPR features as a conventional gold nanoshell, i.e. two LSPR modes for sufficiently large nanoshells. However, models have described that the LSPR of a gold semi-shell are dependent on the polarization of the incident light.[279] Certain LSPR modes are resonant only in one polarization axis, which resembles the behaviour of gold nanorods e.g.[280] Complete gold nanoshells around anisotropic capsule shaped particles on the other hand should red-shift the LSPR of gold nanoshells to the NIR region, as has been shown in experiments.[281] This wavelength region is in particular interesting for plasmonic bio-medical applications.

The normalized absorbance spectra of the semi-shell dumbbells (Figure 6.6) are shown in Figure 6.8A. The initial 2 nm sized nanoparticles exhibit only weak absorption with a peak at ~520 nm. As expected, further growth results in a red-shift of the gold nanoparticle absorption to 525 nm and 555 nm for the 6 nm and 14 nm sized gold nanoparticles, respectively. Upon further growth of the gold nanoparticles and shell formation, the LSPR of the gold nanoparticles have started to couple.[84, 85] This resulted in a very broadband

absorption with little features. The absorption peak at 555 nm remains and a shallow and broad scattering peak from 600 – 900 nm appears (dashed blue line in Figure 6.8A). The semi-shell grown here lacks of sufficient gold nucleation sides, which resulted in an incomplete shell. Furthermore, the gold shell became too thick (25 nm) to provide sharp peaks. Hence, the quality of the grown semi-shells seems to be too poor for distinct LSPR peaks. There are many experimental reports that show similar broadband extinction spectra of gold nanoshells[282-286] and only a few groups have achieved high quality nanoshells with distinct optical features.[277, 281]

The normalized extinction spectra of the gold capsule are shown in Figure 6.8C. The optical properties follow the same trend as the semi-shell nanoparticles. The absorption spectra and colour of the solution (Figure 6.8D), however, are more pronounced due to the larger amount of gold nanoparticles present. The small gold seeds exhibit a LSPR peak at 520 nm. Further growth to 5 nm and 9 nm gold nanoparticles leads to an expected red-shift of the LSPR to 525 nm and 545 nm, respectively. Upon shell formation (15 nm thick) broadband absorption can be observed with a peak centred around 610 nm. Further growth of the capsule shaped gold shell could improve the quality of the optical properties. This would likely lead to a stronger scattering fraction. It was shown that scattering becomes significant for a gold shell thickness that is larger than 20 nm.[277]

6.4 Functionalization of the polymeric lobe

As was shown in the previous sections, the functionalization of the PS-MPS copolymer lobe of the dumbbell shaped particles can be easily done via a vast variety of commercially available silane reagents. This section will show that the newly formed polymer lobe can be functionalized as well. As a first example dye molecules (fluorescein O-methacrylate, FMA) have been copolymerized with styrene during the swelling and polymerization process. Furthermore, the PS-MPS lobe has been amine functionalized again with APTES and covalently coupled with an amine reactive dye that exhibits emission in a different spectral

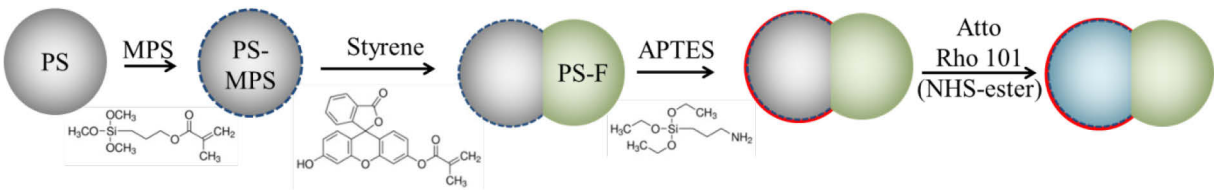

Figure 6.9: *Schematic* approach to synthesize dumbbell shaped particles with two fluorescent labels: fluorescein is copolymerized in the newly grown lobe, whereas AR-101 has been reacted with the amine functionalized lobe.

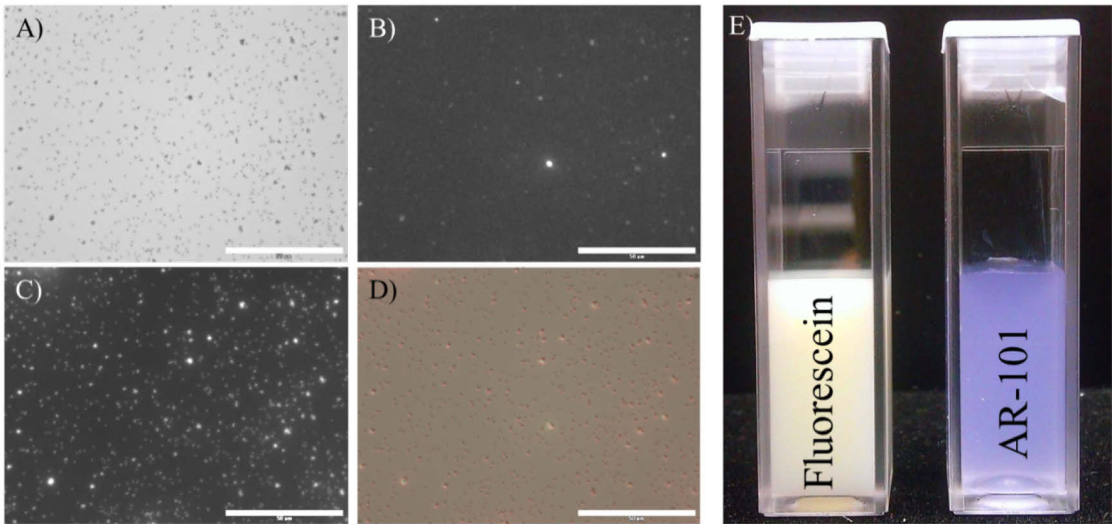

Figure 6.10: Fluorescent dumbbell shaped particles under the microscope (scale bar is 50 µm): A) bright field image, B) fluorescence image corresponding to FMA, C) fluorescence image corresponding to AR-101 and D) superposition of A-C (coloured). E) Photo of dumbbell shaped particles with FMA copolymerized (left) and after AR-101 functionalization (right).

range (AR-101, cf. 4.1.2). Figure 6.9 shows the schematic approach. After dialysis, excess dye molecules have been removed. The dye modification allows for tracking of the dumbbell shaped particles via fluorescence microscopy and shows perfect superposition with the bright field images. Figure 6.10 shows the bright field and fluorescence images that have been recorded with two different excitation filters, i.e. 460 – 490 nm for the excitation of FMA (Figure 6.10B) and 530 – 550 nm for AR-101 (Figure 6.10C).

These fluorescence images show that the AR-101 dye is brighter than FMA. Hence, absorption and fluorescence spectra were recorded, which are shown in Figure 6.11. The absorption and emission spectra of the pure FMA copolymerized dumbbell particles have changed from its monomer (equivalent to OG-488, cf. 4.1.1). FMA normally exhibits a sharp absorption peak at 490 nm with a small shoulder at 460 nm. In Figure 6.11A (black curve) this shoulder shows much stronger absorption. Meanwhile, the fluorescence spectrum has changed significantly (Figure 6.11A, red curve). This behaviour is typical for dimer- or *H*-aggregate formation of linearly stacked dye molecule aggregates.[287-290] It is not surprising that inside the polymer core the dye molecules might form dimers or *H*-aggregates, as FMA is more polar than styrene and very high dye concentrations have been used, which have been confined in the small space of the polymer lobe. Dimer- and *H*-aggregate formation is also known for quenching of the fluorescence due to rapid internal conversion into lower energy exciton states.[290] For comparison, FMA has been dispersed in toluene and sonicated.

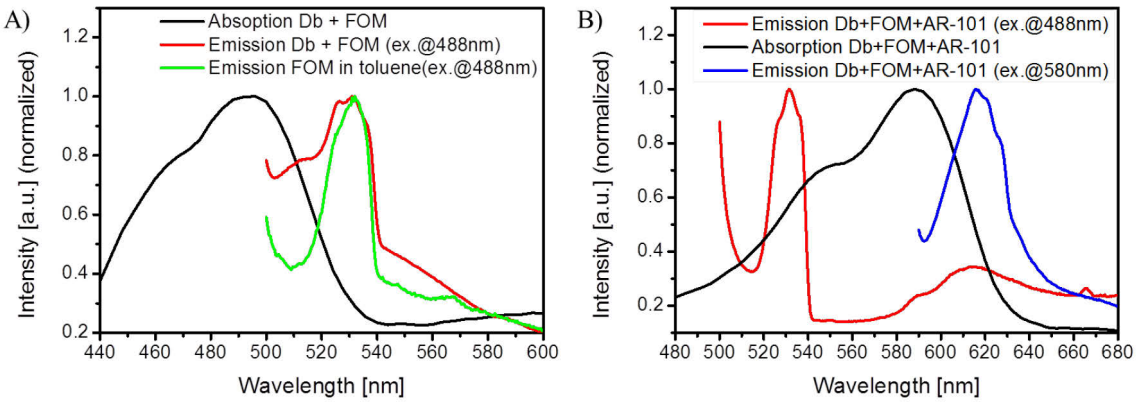

Figure 6.11: A) Absorption and emission spectra of dumbbell shaped particles copolymerized with FMA. The spectra show uncommon broad absorption and sharp fluorescence peaks. B) Absorption and emission spectra of dumbbell shaped particles copolymerized with FMA and functionalized with AR-101. The fluorescence of FMA (red line, excitation at 488 nm) is quenched in the area where AR-101 absorbs. Furthermore, the emission of AR-101 dye appears indicating energy transfer between the two dyes.

Toluene hardly dissolves the dye molecules, which very likely are in an aggregated form present. The fluorescence spectrum of such a solution (Figure 6.11A, green curve) resembles that of the FMA copolymerized dumbbell shaped particles.

Furthermore, the fluorescence of the FMA dye molecules is partly quenched by the AR-101 dye molecules, due to spectral overlap of FMA emission and AR-101 absorption (Figure 6.11B). This is observed for the dumbbell shaped particles with both dye molecules that have been excited at 488 nm. In the absorption region of AR-101 (540 – 590 nm) the fluorescence decreases drastically and weak fluorescence of AR-101 appears (Figure 6.11B, red curve). This could be also verified by lifetime measurements. The dumbbell shaped particles with FMA molecules show a mono-exponential decay with a lifetime of $\tau_{Dp\text{-}F} = 4.16 \pm 0.12$ ns that

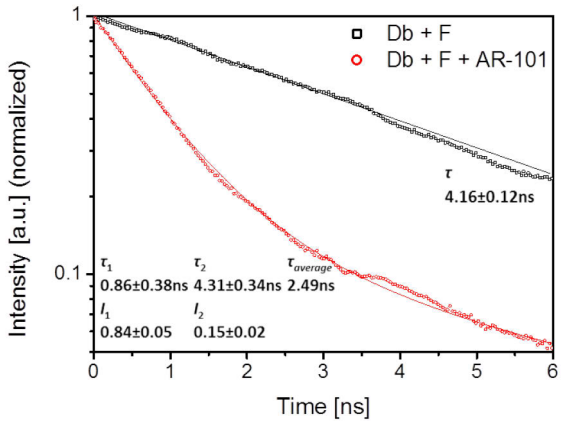

Figure 6.12: Lifetime measurements of dumbbell shaped particles copolymerized with FMA (black squares) and after AR-101 functionalization (red circles). The bi-exponential decay and the reduction of the lifetime prove the energy transfer between the dyes.

matches very well the reported value of 4.1 ns[††] (experimental setup in chapter 8.3.4). The reported lifetime of the dye AR-101 has a similar value with 4.2 ns[‡‡]. However, the dumbbell shaped particles with both dye molecules (FMA and AR-101) have a bi-exponential lifetime response when excited at 488 nm. The slow lifetime τ_{slow} = 4.31±0.34 ns corresponds to the spontaneous emission of the respective dyes and a fast lifetime τ_{fast} = 0.86±0.04 ns indicates a resonant energy transfer between the two dyes.[291] This was surprising as the dye molecules are supposed to be well separated. It leads to the suggestion that some FMA dye molecules must be in close vicinity (~10 nm) to the AR-101 molecules that can be only present on the PS-MPS lobe.[291] Hence, the phase-separation process does not strictly involve the newly formed polymer lobe only. This is also supported by the finding from the previous section, which involved the formation of capsule shaped particles at a higher MPS ratio.

The FMA labelled dumbbell particles show furthermore interesting emulsifier properties. Aqueous dumbbell particle solutions have been added into 1-butanol solution. Upon short ultra-sonication small micro-droplets have been formed in the size range of 5 – 70 µm with two possible shapes (Figure 6.13). Either spherical cluster have been formed or strongly biconcave formed clusters that appear to be almost hollow inside. Bright field and fluorescence images taken in solution further confirmed what has been observed in SEM images (Figure 6.13B+C).

This section so far has proven that dye molecules (and possibly other monomers) can be copolymerized with styrene during the formation of the new dumbbell lobe. It has been reported that the phase-separation step can be also executed with other hydrophobic monomers as long as these monomers are able to swell the hydrophilic PS core.[131] Hence, as a

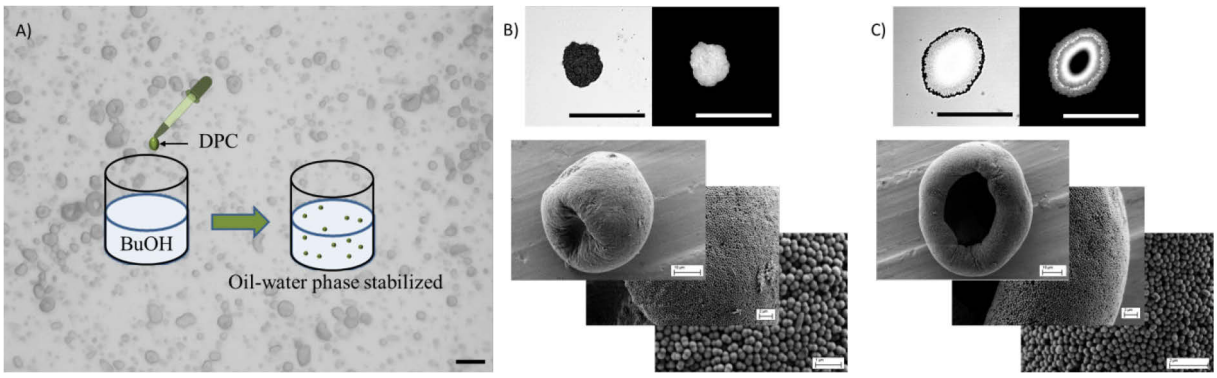

Figure 6.13: A) Water in oil emulsion stabilization by fluorescent dumbbell shaped particles (scale bars in the bright field and fluorescence images: 100 µm). B+C) Bright field (top left) and fluorescence (top right) images confirm the two different shapes that have been seen in the SEM images (lower images at different magnifications).

[††] ISS, Inc. Champaign, IL 61822, USA; Lifetime Data of Selected Fluorophores (www.iss.com).

[‡‡] ATTO-TEC GmbH, 57076 Siegen, Germany; product data sheet for Atto Rho 101 (www.atto-tec.com)

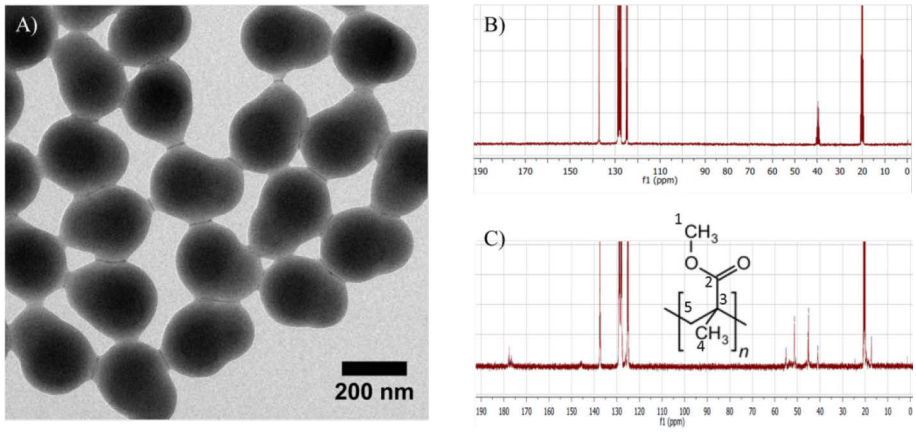

Figure 6.14: A) TEM image of dumbbell shaped PS-PMMA particles. B) ^{13}C-NMR of pure PS dumbbell particles (peak at 42 ppm corresponds to the solvent $CDCl_3$). C) ^{13}C-NMR of PS-PMMA dumbbell particles with new peaks: δ(C1): 55 ppm, δ(C2) 177.5 ppm, δ(C3): 45 ppm, δ(C4): 17 ppm, δ(C5): 20 ppm. The solvent has been deuterated toluene.

model reaction, methyl methacrylate (MMA) has been used to swell the spherical PS-MPS particles. In the same manner dumbbell shaped particles were formed with the new lobe consisting of poly(methyl methacrylate) (PMMA). ^{13}C-NMR (nuclear magnetic resonance) has been applied to verify the incorporation of PMMA with distinct chemical shift peaks e.g. at 177.5 ppm, which are common for ester and carbon acid groups. Figure 6.14B shows the ^{13}C-NMR spectra of PS-MPS-PS dumbbells that have been dissolved in deuterated chloroform ($CDCl_3$, δ = ~40 ppm). The peaks at a chemical shift around 130 ppm are characteristic for aromatic compounds and the peak at 20 ppm corresponds to the aliphatic carbon atoms. Figure 6.14C shows the ^{13}C-NMR spectra of PS-MPS-PMMA dumbbells that have been dissolved in deuterated toluene (C_7D_8, δ = ~21 ppm and ~130 ppm). There are clearly new peaks visible, though the intensity of these peaks is small. This is because of the solvent that has been used to dissolve the particles and has chemical shifts near the peaks of PS due to its chemical similarity. Hence, a quantitative analysis has not been possible. In summary, this section shows that the Janus dumbbell shaped carrier system exhibits high diversity and possibilities for further modification.

6.5 Platinum nanoparticles on Janus dumbbells in H_2O_2

Carrier systems can be used not only to carry certain nanoparticles or molecules, but also to release them after certain stimuli (pH, temperature, salts, and “key-lock” principle).[292-294] This is particular interesting in biology, where in principle, certain drugs are released in the designated area. However, autonomous transport of the carrier systems to a specific area still represents a problem. Artificial nano- and micro devices that can move like microorganisms

have attracted some attention in the past 10 years.[294-299] In principle there exist two classes of such micro-motors: fuel powered and fuel free motors. The second class is driven by external fields, i.e. magnetic and electrical fields or even light. The first class of micro-motors can be driven by chemical reactions, e.g. the decomposition of hydrogen peroxide (H_2O_2) to water and oxygen in the presence of catalytically active platinum.[294, 295, 297]

For the decomposition of H_2O_2 different mechanisms have been proposed. The most widely investigated mechanism is bubble propulsion. The decomposition of H_2O_2 results in the formation of small oxygen bubbles that pushes the particle (containing platinum) away. This propulsion mechanism is non-directive as the bubbles can form anywhere near the particle. On the other side, asymmetric particles that decompose a fuel on one side will form a concentration gradient along the surface of the nano-device. This leads to diffusion of the product away from the nano-device and results in its movement. This mechanism is called diffusiophoresis propulsion and it is directive, as the nano-device will move away from the catalyst side. Self-electrophoresis propulsion is a third mechanism and involves usually bi-metallic rods. Commonly one side consists of platinum and the other side of gold. As before, the platinum rod side decomposes in an oxidation reaction H_2O_2 to oxygen and protons (H^+) with two free electrons in the metal. On the gold side the generated protons and electrons reduce H_2O_2 to two water molecules. The electrons rich platinum anode supplies the electron poor gold cathode with the necessary electrons. Furthermore, the generated protons migrate towards the gold cathode and induce an electric gradient that leads to propulsion in the direction of the platinum side.

The last example of self-electrophoresis propulsion displayed very high speeds from 3 – 20 mm/s for pure gold/platinum rods. By certain improvements, e.g. the use of carbon nanotubes, velocities of up to 200 mm/s have been achieved.[294] Diffusiophoresis propulsion on the other hand results in lower propulsion speeds. Platinum semi-shells have been generated via platinum evaporation techniques on e.g. silica particles (1 µm diameter) or PS particles (2 µm diameter).[296, 298] The silica based system displayed an increase in speed from 6.5 µm/s to 9.5 µm/s in a 15 wt% H_2O_2 solution. The PS based system achieved speeds of 4.3 µm/s in a 10 wt% H_2O_2 solution. Our nanoparticle carrier system can be compared with these systems and is summarized in Tab. 6.1.

Small carrier systems as ours have not been investigated yet. Oxygen bubble formation via the platinum nanoparticles has been verified by adding pure dumbbell shaped nanoparticles and their platinum modified equivalent into 15 wt% H_2O_2 solution. After a few

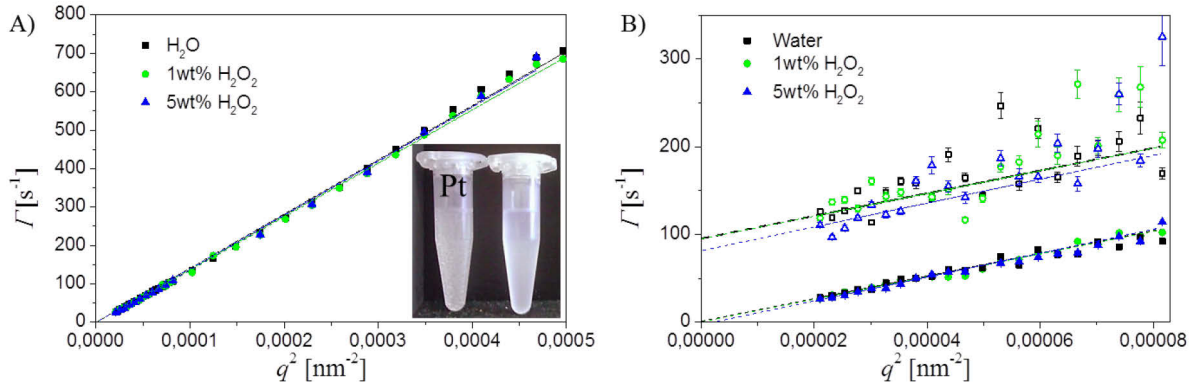

Figure 6.15: DLS (A) and DDLS (B) measurement of dumbbell shaped particles functionalized with platinum nanoparticles at different H_2O_2 concentrations. Filled symbols in B) show the slow mode of the relaxation process ($\Gamma = q^2 D_T$) and open symbols the fast mode ($\Gamma = q^2 D_T + 6D_R$). The inset in A) shows that platinum functionalized particles generate a lot of large oxygen bubbles while the pure dumbbells do not react with the H_2O_2.

seconds large bubbles are formed in the platinum functionalized system only (inset Figure 6.15A). (Depolarized) dynamic light scattering (DLS/DDLS) in 1 wt% and 5 wt% H_2O_2 solutions were applied to deduce the translational- D_T and rotational diffusion coefficient D_R. Higher H_2O_2 concentrations are impractical due to excessive bubble formation. Figure 6.15 shows the plotted relaxation processes as a function of the square of the scattering vector (q^2) and the results are summarized in Tab. 6.1. It can be shown that there is no difference after the addition of H_2O_2. This concludes that self-propulsion via the first two introduced mechanisms, i.e. bubble propulsion and diffusiophoresis propulsion is not sufficient to increase the particles speed. In fact, bubble propulsion is unrealistic. From the mean square displacement $(\Delta x)^2 = 2D_T \Delta t$ the average time for a dumbbell particle to dislocate by its own particle size (Δx = 300 nm) can be calculated, which equals Δt = 0.03 s. For average catalytic

Tab. 6.1: Comparison of diffusion coefficients of platinum (Pt) functionalized particles in different H_2O_2 concentrations.

	c (H_2O_2)	D_T (DLS) [$\mu m^2 s^{-1}$]	D_T (DDLS) [$\mu m^2 s^{-1}$]	$6 \cdot D_R$ (DDLS) [s^{-1}]
SiO_2 (1 µm) + Pt semi-shell[298]	0 wt%	0.68±0.08	-	-
SiO_2 (1 µm) + Pt semi-shell[298]	15 wt%	3.57±0.13	-	-
PS (2µm) + Pt semi-shell[296]	0 wt%	0.21	-	-
PS (2µm) + Pt semi-shell[296]	10 wt%	0.44	-	-
Dumbbell + Pt nanoparticles	0 wt%	1.42±0.01	1.29±0.04	95±3
Dumbbell + Pt nanoparticles	1 wt%	1.39±0.01	1.29±0.03	95±4
Dumbbell + Pt nanoparticles	5 wt%	1.41±0.02	1.36±0.03	81±3

H_2O_2 decomposition one can assume reaction constants of $k \sim 5 \cdot 10^{-2}$ $m^{-2}s^{-1}$.[300, 301] Under assumption of a complete platinum coverage on one lobe an oxygen bubble of 260 nm can form in a 5 wt% H_2O_2 solution while the particle diffuses 300 nm. However, this does not take into consideration that oxygen will dissolve in the water in the meantime or that the bubble will diffuse by itself. Furthermore, DLS/DDLS experiments and bright field microscopy have not observed nano-bubble formation. Hence, bubble repulsion as a propulsion mechanism can be excluded.

Howse *et al*. have calculated the velocity of a platinum functionalized 1.6 µm sized PS sphere at different H_2O_2 concentrations.[301] Interestingly the formula they give for diffusiophoresis propulsion is independent of the particle size.[301, 302] In a 5 wt% H_2O_2 solution they calculated a velocity of 2 µm/s which fits well with their experimental data. The velocity of dumbbell shaped particles calculated via the mean square displacement $(\Delta x)^2$ results in an average velocity of 1.7 µm/s and is close to the values given by Howse *et al*. for diffusiophoresis propulsion. Hence, the concentration gradient seems to be too weak to enhance the diffusion of the quickly moving (Brownian motion) particles. The depolarized experiments, which allow to determine the fast rotational diffusion, show some dependency. The rotational diffusion for higher H_2O_2 concentration is slowed, which one could explain by more directional propulsion, as has been reported elsewhere.[296, 297, 301] However, the qualities of the measurements here are not sufficiently accurate to unambiguously correlate this with directional propulsion in a 5 wt% H_2O_2 solution (Tab. 6.1 and Figure 6.15B).

To summarize this section: Dumbbell shaped particles covered with platinum nanoparticles seem to be too small to effectively enhance the diffusion speed via H_2O_2 fuelled reactions. Their Brownian motion is too strong and possible concentration gradients are too weak to affect the dumbbell fluctuations. Fuel driven propulsion on these length scales seems to be only possible via self-electrophoresis propulsion. Pure gold-platinum nanoparticles of 60 nm in size have shown a small increase of D_T from 7.3 µm^2/s to 8.8 µm^2/s at 1.5 wt% H_2O_2 concentration.[299] Yet, the platinum functionalized dumbbell particles have produced oxygen in large amounts and gradient driven motions (e.g. into cells) might still be possible for biological applications. Furthermore, a complete platinum semi-shell similar to the gold functionalized dumbbell particles might be able to have a significant effect on the fuel driven diffusion of small carrier systems like the presented one.

6.6 Outlook for the anisotropic Janus dumbbell carrier system

The presented carrier system shows highly versatile properties for many possible applications. Due to its synthetic procedure Janus morphology is added. This allows for anisotropic dye modification or metal nanoparticle deposition. Further growth leads to different sized nanoparticles towards metal shells with new plasmonic properties. These shells are colloidal stable and might come in handy for new features. Moreover, diverse silane chemistry allows for modifications with a high variety of active groups beyond amines (APTES). It was also shown that the polymeric lobe can be formed via different monomers, e.g. styrene and MMA or copolymerized with functional molecules, e.g. dyes.

This makes the Janus dumbbell particles an ideal system where multi-functionality is needed. The bivalent character might be interesting to study assembly of natural phenomena, e.g. aggregation behaviour of anisotropic charged proteins at different pH.[303, 304] After PMMA hydrolyzation pH dependency can be additionally introduced at high pH values. Hollow dumbbell shells might have potential as a drug delivery system[305] and can be functionalized accordingly to be used in biology. Furthermore, the presented synthesis approach yields gram scale products and is also interesting for applications outside of the framework of material science.

7. Summary and Outlook

The present thesis focuses on the optical properties of metal nanoparticles. The optical features stem from collective electron oscillations (plasmons) in the metal. Due to the elaborated synthesis reports various morphologies of different metal nanoparticles can be produced and functionalized. By adjusting these protocols the desired optical characteristics can be finely tuned for an individual application. Such applications make use of the properties that the plasmons provide, e.g. the generation of highly confined electric fields or strong light scattering. The work presented here has made use of these features in various ways and has been split into three main parts.

At first the effects of size, shape, refractive index and the metal itself have been investigated in chapter 3, which laid the foundation for the following chapters. As has been discussed, small isotropic particles showed a single dipolar plasmon mode for gold and silver. Upon increasing the size higher order modes appeared. By altering the shape to nanorods for gold or cubes for silver new modes occurred, which are highly dependent on e.g. the aspect ratio. Moreover, a thermosensitive PNIPA shell that collapses at temperatures above 30 °C showed the influence of the dielectric environment around the metal nanoparticles.

The gained insights from the metal nanoparticle syntheses have been further used for direct applications. Chapter 4 aimed for the fabrication and investigation of a spaser. Various approaches have been followed to synthesise a hybrid nanostructure that uses the large electric near-field to couple with a gain medium and create a coherent light source on a sub-wavelength regime. Dye molecules and quantum dots have been used as a gain medium that can be optically excited with a home-built laser setup. Gold nanoparticles of different size and shape have been synthesized and functionalized to spatially and spectrally overlap with the corresponding emitters. These nanostructures have been characterized by different optical and imaging techniques to ascertain the spectral and spatial overlap and the energy transfer of single hybrid particles. However, no spasing could be observed despite various approaches. The comparison with theoretic results has led to the conclusion that gold nanoparticles inhibit too high losses, which cannot be overcome with optical gain in a reasonable way.

Overcoming such losses might be possible with other materials, e.g. silver or non-plasmonic dielectric particles. If such a spaser could be realized, new applications in the field of nano-optics could be actualized. Ultra-fast switching in the fs-regime, low heat generation and nano-sized systems could be useful in e.g. photonic circuits and the research in this field will continue to realize a nano-sized spaser eventually.

Larger nanoparticles have been undesired in the fabrication of a spaser due to the large radiative decay rates. Such properties are favourable for the work in chapter 5, which had the aim to use metal nanoparticles for light trapping in thin-film solar cells. Silver nanoparticles show strong scattering even at relatively small particle sizes. Therefore, isotropic silver nanoparticles have been synthesized and characterized. The size of the nanoparticles, and with it the strongly scattering dipolar mode, has been adjusted to the spectral region where solar cells show reduced absorption, i.e. in the red to near-infrared wavelength region. However, after deposition on the substrate the silver nanoparticles showed mediocre scattering and enhanced absorption. An intensive structural study was executed and it could be shown that parasitic absorption due to a thin silver oxide layer could be eliminated after annealing the silver nanoparticle films at high temperatures.

Such high temperatures are often destructive on thin-film absorbers. Therefore, chemically more stable gold nanorods have been synthesized. The size and aspect ratio has been adjusted to an active wavelength region between $600 - 800$ nm. Furthermore, a protective double-layered silica shell was synthesized to avoid gold leaching and direct hole-recombination on the gold surface. These nanoparticles have been embedded in a perovskite thin-film solar cell which resulted in an increased carrier generation and, hence, higher performance of the solar cell with an increase of efficiency by 40%.

The high demand for environmental-friendly energy makes thin-film solar cells very promising. The reduced costs, due to conserving thinner absorber materials, come with a decrease in solar cell efficiency compared to conventional solar cells. The development of plasmonic solar cells, which are able to trap the light and increase the effective path length by magnitudes of order, is very important. The colloidal chemistry approach did not find wide attention yet, however, it offers several advantages over physical methods, e.g. cheapness, separated spectral and coverage tuneability and easy functionalization.

In chapter 6 a colloidal dumbbell-shaped carrier system has been introduced that exhibits morphological and chemical anisotropy. This so called Janus particle has been functionalized with gold nanoparticle seeds. The optical properties of these gold seeds have been changed by gold nanoparticle growth to a shell, eventually. The chemical anisotropy has been used to synthesize a gold semi-shell. By modification of the carrier shell a full capsule-shaped gold shell has been grown. Moreover, the carrier system shows high diversity for functionalization via the rich silane chemistry or use of new co-monomers. The deposition of other metal nanoparticles can be adopted easily, as has been shown with platinum nanoparticles. In contrast to similar work, such a colloidal system is strongly affected by

Brownian motion and self-propulsion in a chemical fuel is not sufficient. However, due to its readily functionalization, anisotropy and colloidal stability these particles could be useful e.g. as a model system for investigation of protein aggregation. Furthermore, the synthesis procedure results in a highly monodisperse gram-scale product.

8. Experimental

8.1 Materials

For all reactions ultra-pure water has been used, which was purified by reverse osmosis and ion exchange with a Millipore Milli-Q Integral 10. Glassware and stirrers that have been involved in the metal nanoparticle synthesis has been cleaned with aqua regia and extensively rinsed with water prior use. Glassware and stirrers that have been involved in the synthesis of polymer particles has been washed in excess with tetrahydrofuran and water.

Chlorauric acid ($HAuCl_4$), sodium citrate (Na_3Cit), (3-aminopropyl)triethoxysilane (APTES), sodium silicate ($NaSiO_3$), tetraethoxysilane (TEOS), cetyltrimethylammonium bromide (CTAB), ascorbic acid (AA), sodium hydroxide (NaOH), hydrochloric acid (HCl), hydrogen peroxide (H_2O_2), glycerol, polyvinylpyrrolidone (PVP, M_w = 10k, 30k and 54k), acetone, poly(allylamine hydrochloride) (PAH, M_w = 17.5k), poly(acrylic acid) (PAA, M_w = 2.1k), sodium dodecylsulfate (SDS), *N*-isopropylacrylamide (NIPA), 3-(trimethoxysilyl)propyl methacrylate (MPS), azobisisobutyronitrile (AIBN), sodium 4-styrenesulfate (NaSS), fluorescein o-methacrylate (FMA), potassium tetrachloroplatinate (K_2PtCl_4), potassium cyanide (KCN), inhibitor removers, styrene and methyl methacrylate (MMA) have been purchased by Sigma-Aldrich. Oregon Green 488 (OG-488), Alexa Fluor 532 (AF-532), ATTO Rho 101 (AR-101) and dimethyl sulfoxide (DMSO, puris) have been purchased by life technologies. Sodium borohydride ($NaBH_4$), silver nitrate ($AgNO_3$), sodium sulphide (Na_2S), sodium chloride (NaCl) and divinylbenzene (DVB) have been purchased by Merck. Ammonium hydroxide solution (NH_4OH, 30 wt%), potassium carbonate (K_2CO_3) and formaldehyde have been purchased by Roth. Ethanol (puris) has been purchased by VWR. Ethylene glycol has been purchased by Riedel deHäen. Potassium persulfate (KPS) and DOWEX 50WX2 have been purchased by Fluka. *N,N'*-Bis(acryloyl)cystamine (BAC) has been purchased by Alfa Aesar.

The ion-exchange resin DOWEX 50WX2 has been loaded with hydrogen ions before use by running 4 ml of 1 M HCl over the resin and has been cleaned by 1 ml of water. Then the resin has been dried. Styrene and MMA have been purified by an inhibitor remover prior use. All other chemicals have been used as received.

Cellulose dialysis tubing has been purchased from Roth and Fischerbrand.

8.2 Synthesis procedures

8.2.1 Metal nanoparticle synthesis

Spherical gold nanoparticles (Turkevich method)

The synthesis of 14 nm sized spherical gold nanoparticles was performed in a 50 ml one-necked round bottom flask via the Turkevich method.[65] First, 1.55 ml $HAuCl_4$ (10 mM) solution was given into 28 ml water. The solution has been heated to boiling under reflux under stirring at 600 rpm. After 10 min 0.5 ml Na_3Cit (90 mM) has been quickly added. The solution quickly turned dark at first and later red, which indicated the gold nanoparticle formation. The solution has been stirred for another 15 min and then cooled slowly down to room temperature.

These nanoparticles could be coated further with a silica shell.[97] First, the silane reagent APTES has been adsorbed on the surface of the gold nanoparticles by addition of 0.32 ml APTES (1 mM) solution. A thin silica shell has been synthesized via the hydrolysis and condensation of $NaSiO_3$ with the adsorbed APTES. The $NaSiO_3$ solution is basic and the pH had to be adjusted to 10.8 by ion exchange with an acidified ion-exchanging resin (DOWEX 50WX2). After 30 min of APTES addition, 1.5 ml of a 1.08 wt% $NaSiO_3$ solution has been dropped into the reaction mixture and left overnight under stirring. A dense silica shell could be grown onto these nanoparticles via the Stöber method.[98] The gold nanoparticles were transferred into a 250 ml round bottom flask and 115 ml of ethanol were added drop wise at 500 rpm. The pH of the mixture has been adjusted to 10.8 via the addition of approximately 0.6 ml of a 30 wt% NH_4OH solution. After 30 min of stirring the silane precursor TEOS (dissolved in 5 ml ethanol) has been added at a stirring of 250 rpm. The thickness of the silica shell can be tuned by the ratio of TEOS to gold seed particles, e.g. a 25 nm shell could be grown by the addition of 75 µl TEOS. After 5 min the stirring has been reduced to 150 rpm to control the surface morphology of the silica shell. After two days the mixture has been centrifuged and redispersed in ethanol for three times to clean the gold nanoparticles from unreacted reagents.

Growth of spherical gold nanospheres

The size of citrate stabilized gold nanospheres has been increased in a multi-step growth.[196] 6 ml gold nanoparticle dispersion prepared by the Turkevich method has been given to 6 ml of CTAB solution (30 mM) and was added to the growth solution. This growth solution

consisted of 17.55 ml CTAB (15 mM), 0.45 ml $HAuCl_4$ (10 mM) and 74 µl AA (0.1 M). The mixture has been stirred vigorously and was heated to 45 °C following the quick injection of the gold seed nanoparticles. After 10 min the solution has been centrifuged and redispersed in water. The prepared gold nanoparticles were 32 nm in diameter and could be used as seeds for the next growth step. Subsequent growth resulted in quasi-spherical gold nanoparticles up to a diameter of 188 nm. Each growth step has been adjusted by variation of the amount of growth solution to seed particles of the previous growth step with at least one centrifugation and redispersion step for cleaning.

Rodlike gold nanoparticles

Gold nanorods have been synthesized via the seeded growth method.[74] First, approximately 4 nm sized gold seeds have been prepared by the reduction of $HAuCl_4$ with $NaBH_4$ in 0.1 M CTAB solution. To 7.5 ml CTAB solution 0.25 ml $HAuCl_4$ (10 mM) was added and stirred at 250 rpm. After 10 min 0.6 ml ice-cold $NaBH_4$ (10 mM) solution was given and the mixture quickly turned light brown, which indicated the gold seed formation. The reaction was stirred for additional 2 min and then left undisturbed for 1.5 h in a 27 °C water bath.

The size and aspect ratio of the final gold nanorods depended on the ratio of the gold precursor in the growth solution to gold seeds. Larger sized gold nanoparticles have been synthesized by reducing the amount of seeds. Typically, the growth solution has been prepared by the subsequent addition of 0.6 ml $HAuCl_4$ (10 mM), 90 µl $AgNO_3$ (10 mM), 96 µl AA (0.1 M) and the aged seed solution into 14.25 ml CTAB (0.1 M) with mild stirring after each addition step. For the preparation of e.g. 39 x 10 nm sized gold nanorods with a longitudinal LSPR peak centred around λ = 800 nm, 0.15 ml of the seed solution has been added. The reaction mixture has been left undisturbed at 27 °C over night and was centrifuged and redispersed in 10 ml water to remove excess CTAB.

A mesoporous shell around the gold nanorods can be synthesized via the hydrolyzation and condensation of TEOS directly onto the CTAB stabilized gold nanorods.[280] The pH of the aqueous dispersion of gold nanorods has been adjusted to 10.8 by addition of 60 µl of NaOH (0.1 M) solution. After 5 min of stirring at 250 rpm the desired amount of 20 v/v% TEOS in methanol was added. The mixture has been stirred for 1 min at 250 rpm, 5 min at 150 rpm and then left undisturbed. Multiple TEOS injections every 30 min are possible to increase the shell thickness. Again, the ratio of TEOS to gold nanorods determines the silica shell thickness. E.g. a 20 nm silica shell has been grown by adding three times 30 µl of aforementioned TEOS solution. The gold nanorods have been left undisturbed for two days and were centrifuged and

redispersed in ethanol. The presence of CTAB surfactant on the gold nanorod surface leads to a mesoporous silica shell. A dense silica shell can be synthesized in a second growth step under Stöber conditions as mentioned in the previous section.

Gold nanorod oxidation (shortening)

The as-prepared gold nanorods usually exhibit a longitudinal LSPR at longer wavelengths, as it is very difficult to synthesize small gold nanorods with aspect ratios around 1.6. Hence, longer gold nanorods have been synthesized as described before and then oxidized. The as-prepared gold nanorods with a longitudinal LSPR peak centred around λ = 800 nm have been dispersed in fresh 0.1 M CTAB solution. To this dispersion 1.2 ml HCl (0.1 M) and 1.2 ml of 30 wt% H_2O_2 solution has been given. Approximately 1 h later the LSPR peak has been blue-shifted to $\lambda \sim 690$ nm. The oxidation was slowed down and has been increased by addition of another 1.2 ml HCl (0.1 M) and 1.2 ml of 30 wt% H_2O_2 solution. Approximately 1 h later the LSPR peak was blue-shifted to $\lambda \sim 565$ nm.

The oxidation process has been subsequently followed via UV/Vis measurements and stopped shortly before the desired longitudinal LSPR was reached. The gold nanorod dispersion has been centrifuged and redispersed in basic water to stop the oxidation process.

Spherical silver nanoparticles

Spherical silver nanoparticles have been synthesized following a modified protocol of Steinigeweg and Schlücker.[69] 50 ml water/glycerol (40 v/v % glycerol) mixture has been heated to 95 °C. To this solution, 9 mg $AgNO_3$ was added and stirred at 500 rpm for 1 min. Na_3Cit (3%) was added as reducing agent and stirred for 1 h at 500 rpm and 95 °C. The mixture turned quickly from yellow to orange after 10 min and became turbid. After 1 h the solution was strongly turbid and appeared to be yellow-green. The reaction was cooled down to room temperature and stored at 4 °C. These silver nanoparticles were 50 nm in size.

In the second growth step, a growth solution was prepared consisting of 322 ml water/glycerol (14 v/v % glycerol) and 1.16 g PVP K30. The solution was stirred for 30 min at 750 rpm before 15.6 ml aforementioned silver seed solution was added. After 20 s, 6.9 ml diamine silver complex (140 mg $AgNO_3$ in 7 ml water and 1.54 ml NH_4OH (30%)) was added and immediately followed by the addition of 92 ml AA (441.6 mg) as reducing agent. The colour changed quickly to dark green – brownish after 10 min. After 1 h stirring at 750 rpm, another portion of 12 g PVP K30 was added and stirred for additionally 30 min at 1000 rpm.

The resulting 164 nm sized silver nanoparticles have been washed twice with water, concentrated by centrifugation to 100 ml and stored at 4 °C.

Cubic silver nanoparticles

Silver nanocubes have been synthesized following the protocol of Skrabalak *et al*.[306] A 20 ml glass vial has been filled with 6 ml of ethylene glycol, heated to 152 °C and stirred at 250 rpm for 1 h to remove water. 70 µl of Na_2S (3 mM) dissolved in ethylene glycol has been added and stirred for 8 min. Then, 30 mg of PVP (30k) has been dissolved in 1.5 ml ethylene glycol and given to the reaction mixture. Immediately thereafter, 0.5 ml of $AgNO_3$ (24 mg) has been injected into the solution. The solution quickly turned from orange to brown and green after a few minutes. The reaction has been completed after 15 min and was quenched by placing the vial into cold water leaving it until the solution cooled to room temperature. The silver nanocubes were dispersed in 16 ml acetone, centrifuged and redispersed in water. This cleaning process was repeated at least three times.

8.2.2 Dye functionalization of gold nanoparticles

Dye incorporation in the silica shell of gold nanoparticles

Dye incorporation in the silica shell has been done under Stöber conditions, i.e. in a basic water/ethanol (1:4) solution. To avoid the reaction of NH_4OH solution with the amine reactive dyes NaOH has been used as base for the silica coating. One day before the addition of TEOS to the reaction mixture, the dye molecules have been conjugated with the silane reagent APTES, which provides a primary amine group. Typically, 1 mg of amine-reactive dye (i.e. OG-488, AF-532 and AR-101) has been dissolved in 1 ml water-free DMSO that contained 12 mg of APTES. This resulted in an average excess ratio of 10:1 APTES to dye to achieve a high conjugation. The mixture was vigorously stirred and then left over night on an orbital shaker in the dark until further use.

For the silica coating highest dye incorporation was achieved by the v/v ratio of APTES/TEOS = 1/5. For example, gold nanospheres were synthesized as described above and coated with a thin 7 nm silica shell. After cleaning and redispersion in 60 ml of a water/ethanol mixture (1/4) the pH has been adjusted to 10.8 by the addition of NaOH (0.1 M). The nanoparticle dispersion has been stirred at 250 rpm and meanwhile bubbled with Ar-gas for 30 min. The dye-APTES conjugate (1 ml) and 64 µl of TEOS are dissolved in 4 ml of ethanol and added slowly to the reaction mixture in the dark. After 5 min the stirring is

reduced to 150 rpm. After two days of stirring in the dark the sample is centrifuged and redispersed in ethanol for at least five times until the supernatant shows no fluorescence of unreacted dye molecules. The first supernatant is kept to determine the amount of unreacted dye molecules. The difference in intensity of the original dye solution (diluted appropriately) to this supernatant has been used to calculate the amount of dye molecules per gold nanoparticle.

Gold removal from hybrid dye-functionalized core-shell gold-silica particles

To investigate the hollow silica shell nanoparticles with embedded dye molecules the gold core has been leached with KCN. A small portion of the hybrid core-shell gold-silica nanoparticle solution ($1/20^{th}$ of above mentioned synthesis) with dye molecules embedded in the silica shell has been centrifuged and redispersed in 7 ml water. The pH has been increased to 11 by adding 0.1 M NaOH solution to avoid the formation of toxic hydrogen cyanide. Then 3 ml of 30 mM KCN solution has been added to the nanoparticle dispersion and was stirred for 24 h. Thereafter, the mixture has been centrifuged and redispersed in ethanol for three times to clean the hollow silica nanoparticles.

Layer-by-layer adsorption of dye-functionalized polyelectrolytes

Amine reactive dye molecules have been covalently linked to a cationic polyelectrolyte containing primary amines (PAH, M_w = 17.5k). 30.5 mg PAH has been dissolved in 50 ml water. The pH of the solution has been adjusted to approximately 8.5 by the addition of NaOH (1M) and was bubbled with Ar-gas for 30 min at 250 rpm. Then, 2 mg of the amine-reactive dye, dissolved in 1.5 ml DMSO, has been added to the polymer solution and has been stirred over the night in the dark. The solution has been dialyzed against water with a cut-off at M_w = 7 – 8k until the conductivity has been below 6 µS/cm. Thereafter, the solution has been lyophilized and the dye-functionalized polymer has been stored in the dark at 4 °C until further use.

The layer-by-layer functionalization has been adapted from Schneider *et al.*[24] 17.5 mg of the dye-functionalized polymer (~ 250 µM) and 35 mg NaCl (0.15 M) has been dissolved in 4 ml water. Furthermore, 2 mg of the anionic polyelectrolyte PAA (M_w = 1.6k, 310 µM) and 35 mg NaCl (0.15 M) has been dissolved in 4 ml water. For the polymer adsorption and build-up of new layers the polymer solution has been stirred vigorously. 4 ml of the as-prepared gold-silica core-shell nanoparticle solution has been added slowly at 1 ml/h with a syringe pump. The solution was left over night in the dark and centrifuged and redispersed in 4 ml

water three times to separate the nanoparticles from excess polymers. The silica shell, which was used as a spacer layer, provides negative charges via free silanol groups. Hence, dye-PAH polymers were adsorbed first on the nanoparticles. In a second step the now positively PAH modified nanoparticles were dropped into the PAA solution. This process could be repeated several times. Successful polymer adsorption has been followed via zeta potential measurements (cf. Figure 4.5B).

8.2.3 Synthesis of a PNIPA shell around gold nanorods and QDs adsorption

Five times the amount of CTAB stabilized gold nanorods has been prepared as described before and concentrated to 5 ml. For later polymerization it is beneficial to provide carbon double bonds on the surface of the gold nanorods. BAC provides two sulphur atoms that have high affinity towards gold and two carbon double bonds at the end respectively. Hence, it will be used as nucleation site and cross-linker. 21.5 mg BAC has been dissolved in 30 ml water and the gold nanorods were added slowly under sonication. After stirring at 150 rpm overnight the gold nanorods are centrifuged and dispersed in 4 ml water.

The nanorod dispersion (2 ml) was transferred into a 25 ml round bottom flask and diluted by 1 ml SDS solution (25 mM). The monomers NIPA (20 mg in 0.5 ml water) and BAC (2.3 mg in 0.5 ml water) has been added subsequently. The mixture was stirred at 350 rpm, heated to 35 °C and purged with nitrogen for 1 h. Then 0.5 mg KPS dissolved in 0.25 ml water has been added quickly. Immediately thereafter the water bath has been exchanged with one at 80 °C to initiate the radical polymerization reaction. The reaction has been finished after 7 h and after cooling to room temperature the hybrid gold nanorods have been centrifuged and redispersed in 5 ml water at least ten times to separate the gold nanorods from unreacted molecules and secondary particles.

The CdTe QDs have been provided by the group of Professor Eychmüller from Technical University Dresden. They are stabilized by the negatively charged 3-mercapto-propionic acid (MPA) and dispersed in water. Due to the negative charge of the initiator KPS the PNIPA microgel is negatively charged as well. Hence, cationic PAH has been adsorbed on the surface of the QDs. 18 mg PAH has been dissolved in 10 ml water and the pH has been adjusted to 7 with NaOH (1M). To this solution 1 ml of the MPA-stabilized QDs ($7 \cdot 10^{6}$ M) has been added drop-wise at 0.25 ml/h under vigorous stirring overnight in the dark. The QDs have been centrifuged and redispersed in 10 ml water.

The hybrid gold-PNIPA nanoparticles have been diluted ten times (1 ml nanorod dispersion in 9 ml water) and were added slowly via a syringe pump at 2 ml/h into the QDs

solution in the dark under vigorous stirring. The QDs-modified hybrid gold nanorods have been centrifuged and redispersed in water three times to separate excess QDs from the nanorods.

8.2.4 Dumbbell shaped particles and their modifications

Pure PS-MPS-PS dumbbell particles

Before dumbbell formation, spherical PS-MPS particles have been synthesized. In a first step PS particles were prepared via radical emulsion polymerization. A three-necked 1 l round bottom flask was fed with 0.35 g SDS dissolved in 350 ml water, purged with nitrogen and stirred for 30 min at 250 rpm with a sealed precision glass (KPG) stirrer with movable blades. Thereafter, 30 g of styrene (cleaned over an inhibitor remover resin) has been charged drop-wise and the mixture is stirred for another 30 min under nitrogen purge. Then 0.3 g KPS dissolved in 15 ml water is added and the solution is quickly heated to 70 °C for 8 h under nitrogen flow. After cooling down to room temperature the PS-MPS copolymer layer is synthesized onto the PS particles. For that 13.245 g solid-content of the as-prepared PS particles is charged in a 500 ml three-necked round bottom flask and diluted to a total volume of 300 ml. The dispersion is stirred for 30 min at 250 rpm with a sealed precision glass (KPG) stirrer with movable blades and purged with nitrogen. Then, 1.2525 g of MPS and 75 mg AIBN are dissolved in 12.525 g styrene and added drop-wise to the PS dispersion. Respectively, the PS-MPS particles for a higher amount of MPS have been charged with 3.44 g MPS, 75 mg AIBN and 10.33 g styrene. After 5 min stirring the solution is quickly heated to 70 °C and stirred for 7 h under nitrogen flow. After cooling to room temperature the spherical PS-MPS particles can be cleaned via ultrafiltration or further used for the preparation of dumbbell shaped colloids.

Dumbbell particles have been prepared via the phase separation technique of Park *et al.*[130] 3.2625 g solid-content of the PS-MPS particles has been charged in a 250 ml three-necked round bottom flask and diluted with water to 55 ml total volume. Then 0.08 g of NaSS has been dissolved in 5 ml water and added drop-wise. The dispersion was stirred for 20 min at 250 rpm with a sealed precision glass (KPG) stirrer with movable blades and purged with nitrogen. 0.06 g AIBN has been dissolved in 10.97 g styrene and added drop-wise into the solution. After 30 min of stirring and further nitrogen purge the temperature was rapidly increased to 70 °C for 8 h. Afterwards, the mixture is cooled to room temperature and the product is cleaned by ultrafiltration (nitrocellulose membrane, 0.22 µm GSWP, Merck Millipore Ltd.) until the eluent had a conductivity below 10 µS/cm.

Copolymerization of fluorescein and PS-MPS-PMMA dumbbells

PS-MPS particles have been synthesized according to the previous section. For fluorescein labelled dumbbell particles the procedure has been similar: 3.2625 g solid-content of the PS-MPS particles has been charged in a 250 ml three-necked round bottom flask and diluted with water to 55 ml total volume. The dispersion was stirred for 20 min at 250 rpm with a sealed precision glass (KPG) stirrer with movable blades and purged with nitrogen. 0.06 g AIBN has been dissolved in 10.97 g styrene and added drop-wise into the solution. The mixture has been stirred for 30 min with further nitrogen purge and then the temperature has been rapidly increased to 70 °C. After 30 min 22 mg of FMA dissolved in 6 ml basic water (pH~11) has been added to the reaction via a syringe pump at 6 ml/h. After 8 h total reaction time the mixture has been cooled to room temperature and was dialyzed against water with a cut-off at M_w = 8 – 10k until the water showed no fluorescence anymore.

For PS-MPS-PMMA dumbbell particles 3.2625 g solid-content of the spherical PS-MPS particles have been charged in a 250 ml three-necked round bottom flask and diluted with water to 55 ml total volume. Then 0.08 g of NaSS has been dissolved in 5 ml water and added drop-wise. The dispersion was stirred for 20 min at 250 rpm with a sealed precision glass (KPG) stirrer with movable blades and purged with nitrogen. 0.06 g AIBN, 0.5 g DVB and 1 g of styrene has been dissolved in 10 g MMA and were added drop-wise into the solution. After 30 min of stirring and further nitrogen purge the temperature was rapidly increased to 70 °C for 8 h. Afterwards, the mixture is cooled to room temperature and the product is cleaned by ultrafiltration (nitrocellulose membrane, 0.22 µm GSWP, Merck Millipore Ltd.) until the eluent had a conductivity below 10 µS/cm.

Amine functionalization of spherical PS-MPS and dumbbell shaped particles and their dye-functionalization

The dumbbell shaped particles exhibit free silanol groups by hydrolyzation of the three methoxy groups from MPS. Hence, these silanol groups can undergo silane chemistry, i.e. a condensation reaction with APTES, which provides a primary amine group. 10 ml of a diluted dumbbell dispersion (0.3 wt%) has been charged into a 20 ml vial. Then, 75 µl of NaOH (0.1 M) solution has been added and stirred for 5 min at 250 rpm. Afterwards, 1 ml APTES solution (14 mM) has been added, which corresponds to 10 molar equivalents of MPS present. For lower equivalents less APTES solution has been added respectively (0.1 ml or 0.4 ml). The mixture was stirred overnight and centrifuged and redispersed in water for three times to remove unreacted reagents.

Similar to the amine functionalization of dumbbells, spherical PS-MPS particles have been initially modified by APTES. 10 ml of a diluted PS-MPS dispersion (0.075 wt%) has been charged into a 20 ml vial. Then, 75 µl of NaOH (0.1 M) solution has been added and stirred for 5 min at 250 rpm. Afterwards, 1 ml APTES solution (14 mM) has been added, which corresponds to 10 molar equivalents of MPS present. For lower equivalents less APTES solution has been added respectively (0.1 ml or 0.4 ml). The mixture was stirred over-night and centrifuged and redispersed in water for three times to remove unreacted reagents.

The amine modified dumbbell particles can e.g. be functionalized with amine-reactive dye molecules. 5 ml of the amine functionalized dumbbell dispersion (0.2 wt%) has been charged into a vial and stirred at 250 rpm in the dark. 0.3 mg of amine-reactive AR-101 has been dissolved in 5 ml water and was added to the dispersion. This corresponds roughly to a molar ratio of 1:10 (dye:APTES). The solution has been stirred in the dark overnight and then dialyzed against water with a cut-off at $M_w = 7 - 8$k until the water did not show any fluorescence.

Gold deposition on spherical PS-MPS particles

The amine modified particles can be functionalized with metal nanoparticles by *in-situ* reduction or post-modification via grafting. The spherical PS-MPS-APTES particles have been used firstly to test the effect of the different deposition methods. Small gold nanoparticles (5 – 6 nm in diameter) have been synthesized via the reduction of 6 ml of $HAuCl_4$ (0.4 mM) by 0.6 ml $NaBH_4$ (10 mM) solution in the presence of Na_3Cit (1.2 mg) and PVP (60 mg, M_w = 10k) as stabilizers. The reaction has been stirred for 1 h and then added to 6 ml of a 0.015 wt% PS-MPS-APTES dispersion. The mixture has been stirred 1 h to let the gold nanoparticles graft onto the amine functionalized surface and was then centrifuged and redispersed in water to separate the small gold nanoparticles that have not been grafted onto the polymer carrier system. This method has been labelled as "$NaBH_4$, grafted".

In-situ reduction and adsorption of gold nanoparticles onto the surface of the PS-MPS-APTES particles was conducted in a similar way. In a 6 ml PS-MPS-APTES (0.015 wt%) dispersion 1.2 mg of Na_3Cit and 60 mg of PVP (M_w = 10k) has been dissolved. The solution has been charged with 0.25 ml $HAuCl_4$ (10 mM) following 0.6 ml $NaBH_4$ (10 mM) solution. The mixture has been stirred 1 h and was then centrifuged and redispersed in water to separate the small gold nanoparticles that have not been adsorbed onto the polymer carrier system. This method has been labelled as "$NaBH_4$, *in-situ*".

Furthermore, larger gold nanoparticles have been synthesized via the reduction with excess AA. In a 6 ml PS-MPS-APTES (0.015 wt%) dispersion 105 mg of AA (0.1 M) and 60 mg of PVP (M_w = 54k) has been dissolved. Then, 2 ml of $HAuCl_4$ (1 mM) has been added drop-wise via a syringe pump at 6 ml/h under vigorous stirring. After the addition of the gold precursor the reaction has been stirred for 1 h and was then centrifuged and redispersed in water to separate the gold nanoparticles that have not been adsorbed onto the polymer carrier system. This method has been labelled as "AA, *in-situ*".

Metal deposition on dumbbell shaped particles and nanoparticle growth

For the dumbbell shaped carrier system the second method described before has been used, i.e. *in-situ* reduction and adsorption of metal nanoparticles onto the amine modified dumbbell particle surface. In a 6 ml dispersion of amine functionalized dumbbell particles (0.05 wt%) 1.2 mg of Na_3Cit and 60 mg of PVP (M_w = 10k) has been added. The solution has been charged with 0.25 ml $HAuCl_4$ (10 mM) for gold nanoparticles or 0.25 ml K_2PtCl_4 (10 mM) for platinum nanoparticles, respectively. After 5 min of stirring 0.6 ml $NaBH_4$ (10 mM) solution has been added quickly. The mixture has been stirred 1 h and was then centrifuged and redispersed in water to separate the small gold/platinum nanoparticles that have not been adsorbed onto the polymer carrier system.

Gold nanoparticle growth has been achieved by mild reduction of $HAuCl_4$ in formaldehyde and K_2CO_3.[277, 283] First, 10 mg of K_2CO_3 has been dissolved in 20 ml $HAuCl_4$ (1 mM) solution and left overnight in the dark. The gold precursor gets reduced from Au(III) to Au(I), which can be followed by the decolouration of the yellow precursor solution. The dumbbell particles with 2 nm sized gold nanoparticles grafted (0.3 wt%) have been diluted in water and an appropriate amount of the Au(I) solution was added and stirred for 5 min at 250 rpm. Thereafter, formaldehyde solution (7.5 wt%) has been added in a 1:10 ratio of formaldehyde : growth solution. Formaldehyde is a mild reducing agent and gold reduction occurred only on the existing gold seed nanoparticles. After 1 h the reaction has been finished and the sample was centrifuged and redispersed in water to separate unreacted reagents. The total reaction volume has been kept constant at 5 ml. The added volumes for all systems are summarized in Tab. 8.1.

Tab. 8.1: Composition of volumes for different gold nanoparticle growth. A higher amount of growth solution / formaldehyde and a lower amount of seed particles ($V_{dumbbell}$) results in larger gold nanoparticles. Cf. Figure 6.6 and Figure 6.7.

Sample	MPS:Styrene 1:10			MPS:Styrene 1:3		
	1st growth	2nd growth	3rd growth	1st growth	2nd growth	3rd growth
$V_{dumbbell}$	0.2 ml	0.2 ml	0.1 ml	0.2 ml	0.2 ml	0.1 ml
V_{water}	4.7 ml	4.4 ml	3.8 ml	4.6 ml	3.7 ml	2.7 ml
$V_{growth\ sol.}$	0.1	0.4 ml	1 ml	0.2 ml	1 ml	2 ml
$V_{formaldehyde}$	10 µl	40 µl	0.1 ml	20 µl	0.1 ml	0.2 ml

8.3 Characterization methods

8.3.1 Optical characterization

UV/Vis spectroscopy

Extinction spectra in aqueous/ethanol solutions have been recorded with an Agilent 8453 UV/Vis spectrophotometer that could be externally heated or cooled via a water bath with a circulation pump. 2 ml of the solution has been given into a quartz cuvette from Hellma Analytics with a 10 mm light path length (100-QS). The cuvette has been cleaned with Hellmanex solution and ethanol after each use.

Fluorescence spectroscopy

Fluorescence spectra have been recorded with a Horiba FluoroMax-3 with a monochromator slit width of 2 nm. The excitation wavelength has been set to λ_{ex} = 488 nm for OG-488 and FMA, λ_{ex} = 532 nm for AF-532 and λ_{ex} = 565 nm for AR-101. 2 ml of the solution were given into a quartz cuvette from Hellma Analytics with a 10 mm light path length (101-QS). The cuvette has been cleaned with Hellmanex solution and ethanol after each use. The solution could be externally heated or cooled via a water bath with a circulation pump.

Absorption, transmission and reflection of substrates

The optical measurements of the silver nanoparticle coated glass samples were performed using a Perkin Elmer Lambda 1050 spectrophotometer equipped with a 150 mm integrating sphere. Gold nanorods on FTO substrates with and without perovskite and the gold decorated dumbbell particles have been measured with a Perkin Elmer Lambda 950 spectrophotometer equipped with a 150 mm integrating sphere. The integrating sphere enables the separation of transmission and reflection (Figure 8.1). It's a hollow spherical cavity that is covered with a

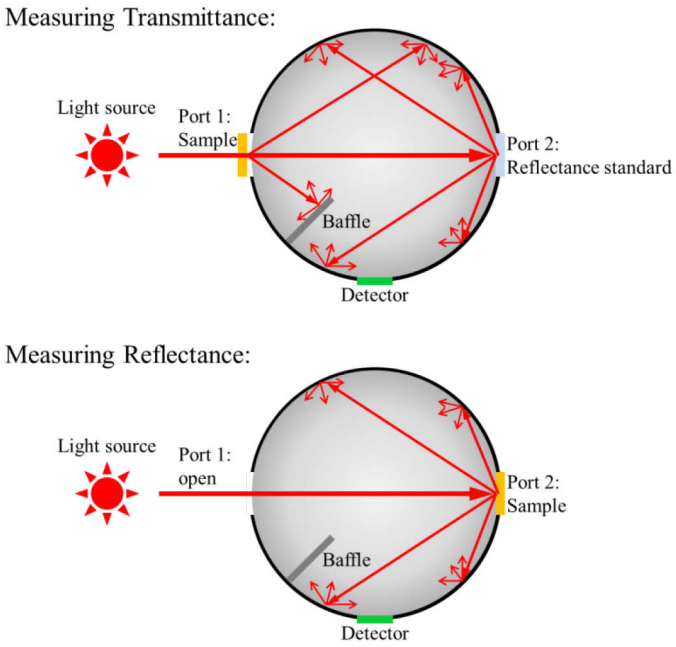

Figure 8.1: Design of the integrating sphere to measure the transmittance and reflectance of a sample on a substrate. The individual ports can be opened or closed or covered by the sample.

diffuse white reflective coating that scatters light equally in all directions and eventually is detected. Two ports can be opened or closed for different modes of measurements: If the sample is placed in front of the light source (port 1) the transmittance is measured where the second port is covered with the same reflective material as in the integrating sphere. For reflectance measurements the sample is placed at the second port with the first port opened. The absorption has been calculated by $A = 1\text{-}(R_{diff} + T_{diff})$. For silver nanoparticles the absorption has been measured with the substrate placed inside the integrating sphere.

8.3.2 Microscopy

All images have been processed with the imaging software ImageJ V1.46r (Wayne Rasband, National Institute of Health, USA) to analyse nanoparticle sizes and substrate coverages.

Transmission electron microscopy

Transmission electron microscopy (TEM) has been used to investigate the size and shape of the metal and polymer particles, as well as whether the individual functionalization has been successfully executed. Prior sample casting, the TEM grids (CF200-Cu, Electron Microscopy Sciences) have been pre-treated by glow discharge for 15 s. The sample (0.01 – 0.1 wt%, 5 µl) has been drop-casted onto the grid. After 2 min excess liquid has been blotted with a filter paper. The remaining thin film has been dried at room temperature for 1 h before inserted in

the sample holder (EM21010, JEOL). The sample has been transferred into a JEOL JEM-2100 with a LaB_6 cathode, which has been operated at a 200 kV acceleration voltage.

Scanning electron microscopy

Scanning electron microscopy (SEM) has been used to investigate the metal nanoparticle films on different substrates, i.e. corning glass (CG) and fluorinated tin oxide (FTO). The metal nanoparticle images were taken with a back-scatter detector in a Zeiss LEO GEMINI 1530 at an acceleration voltage of 10 kV. For polymer particles an acceleration voltage of 3 kV was chosen.

Optical microscopy

Bright field and fluorescence microscopy images have been obtained by using an Olympus BX51 optical microscope with an Olympus U-TV1 X CCD camera to record images digitally. Two lenses have been used: 10x magnification (Olympus UPlanFl 10x) for overviews and 60x magnification (Olympus UPlanFl N 60x). Bright field images have been illuminated from the back of the substrate.

For fluorescence images an EXFO X-Cite Series120 UV-lamp has been used with two different filters to excite different dyes and separate the respective emission, i.e. the U-MWIBBP cube for green emission (e.g. OG-488 and fluorescein) and the U-MNG cube for yellow emission (e.g. AR-101).

8.3.3 Dynamic light scattering and zeta-potential measurements

When light encounters small particles it is scattered elastic in all directions. If coherent and monochromatic light is used, the scattered light of different particles interferes with each other, which leads to intensity fluctuations $I_S(\boldsymbol{q},t)$. These intensity fluctuations arise from the constant Brownian motion of the particles that influences the interferences between these particles over time. The scattering vector q is given as:

$$q = \frac{4\pi n}{\lambda} \sin\left(\frac{\theta}{2}\right) \tag{8.1}$$

with the scattering angle θ, the wavelength λ and the refractive index n of the solvent. In a dynamic light scattering (DLS) experiment the intensity fluctuations are measured and correlated with each other. The resulting time autocorrelation function[307]:

$$g_2(q,\tau) - 1 = \beta e^{-2q^2 D_T t} \tag{8.2}$$

gives characteristic parameters of the diffusion motion of the particles, i.e. the translational diffusion coefficient D_T. The factor β is a correction factor that depends on the geometry and alignment of the laser beam. The product $q^2 \cdot D_T = \Gamma$ is the decay rate.

The translational diffusion coefficient D_T can then be used to calculate the hydrodynamic radius R_h via the Stokes-Einstein equation[308] for spherical systems if the viscosity η of the dispersion medium is known:

$$D_T = \frac{k_B T}{6\pi\eta R_h} \tag{8.3}$$

In depolarized dynamic light scattering (DDLS) the analysed light is horizontally polarized. For anisotropic particles the autocorrelation function then depends not only on D_T but also on the rotational diffusion coefficient D_R:

$$g_2(q,\tau) - 1 = \beta e^{-2(q^2 D_T + 6D_R)t} \tag{8.4}$$

The decay rate Γ is now given as:

$$\Gamma = q^2 D_T + 6D_R \tag{8.5}$$

Upon plotting Γ versus q^2, the value of $6D_R$ can be obtained directly by extrapolation of $q^2 \rightarrow 0$ and D_T by the slope of the curve (Figure 8.2B).

Dynamic light scattering for sizing

DLS measurements for sizing have been carried out with a Malvern Zetasizer Nano ZS. The instrument is equipped with a 532 nm laser with a fixed detector at a scattering angle of 173°. For the analysis 1 ml of an approximately 0.01 – 0.001 wt% dispersion was measured in a disposable PS cuvette. The cuvettes have been dedusted prior use and the water used for dilution has been filtered with a 0.2 µm syringe filter to avoid sample contamination. Each measurement has been repeated three times with 10 individual measurement runs á 30 s. The dispersion has been left for 20 min prior measurement to attain thermal equilibrium.

(Depolarized) dynamic light scattering to determine D_T *and* D_R

DLS and DDLS measurements have been conducted with an ALV-4000 compact goniometer system that uses a laser with a wavelength of 633 nm. The schematic setup is shown in Figure 8.2A. The laser passes an automatic attenuator and a vertical polarizer (Glan-Thompson prism, extinction ratio 10^4:1) before the light is scattered at the sample dispersion. The samples have been prepared in a quartz cuvette in the same way as for the sizing experiments.

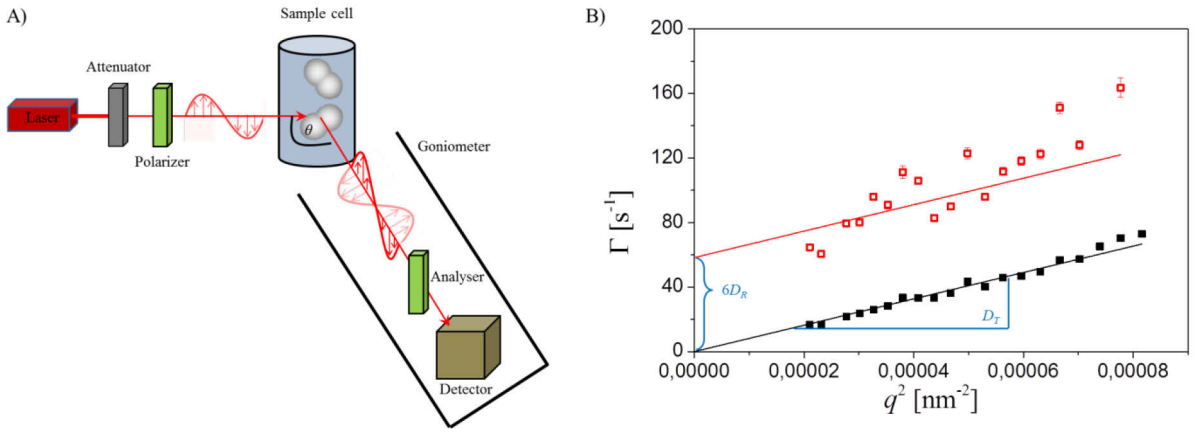

Figure 8.2: A) (D)DLS setup: Laser light passes an automated attenuator and a vertical polarizer. The light scatters at the colloidal dispersion and passes an horizontal analyser (only in DDLS) to be detected at an avalanche photo diode (APD). The intensity fluctuations are measured over different scattering vectors by changing the scattering angle θ with a goniometer. B) Exemplary fits of the relaxation rate versus q^2 to determine D_T and D_R of a DLS (filled black squares) and DDLS (hollow red squares) experiment.

Each sample has been left one hour at a set temperature to reach thermal equilibrium. For DLS measurements no analyser was used. For DDLS measurements the analyser (Glan-Thompson prism, extinction ratio 10^6:1) was set to 90° perpendicular to the polarizer. The signal was recorded with an avalanche photo diode (APD). A goniometer arm enables to measure at different scattering angles, i.e. 20 – 140° (5° steps) in DLS mode and 20 – 40° (1° steps) in DDLS mode. A LSE-5004 control unit sets the measurement conditions (scattering angle, temperature etc.) and correlates the incoming signal. Three individual measurements have been made for each scattering angle and were recorded for 120 s (DLS) or 300 s (DDLS) respectively.

To determine D_T and D_R the time autocorrelation function was fitted with an exponential decay (cf. equation 8.2 and 8.4). The resulting relaxation rate Γ has been plotted versus the square of the scattering vector q^2. D_T and D_R have been obtained as shown in Figure 8.2B.

Zeta-potential measurements

Zeta-potential measurements have been conducted with a Malvern Zetasizer Nano ZS. The cuvette that has been used (Malvern disposable folded capillary cell, DTS1070) was washed with ethanol and water, dedusted and filled with 1 ml of an approximately 0.01 wt% dispersion. The scattering angle has been fixed at 17° with a laser wavelength of 532 nm. The instrument measures the electrophoretic mobility μ_e in an applied electric field. The electrophoretic mobility is the velocity (v) of a particle/molecule divided by the applied electric field strength (E) and dependent on the dielectric constant ε, the zeta-potential ζ, an

factor from Henry's function $f(\kappa a)$ (= 1.5 with the Smoluchowski approximation) and the viscosity η:

$$\mu_e = \frac{v}{E} = \frac{2\varepsilon\zeta f(\kappa a)}{3\eta} \tag{8.6}$$

The instrument measures the velocity of the particles at a given electric field, which enables to calculate the zeta-potential. This can be done by using the Doppler effect and measuring the frequency shift caused by the moving particle (Laser Doppler Velocimetry, LDV). The measurement can be further improved by measuring not the frequency shift but the phase shift of the scattered beam (Phase Analysis Light Scattering, PALS) which is unaffected from e.g. thermal drifts etc.

8.3.4 Pump-probe experiments

The laser setup that has been used for the pump-probe experiments has been established at the Humboldt University Berlin by Günter Kewes (Figure 8.3). It enables strong excitation of the samples. For systems that have been functionalized with OG-488, the "Tsunami" (SpectraPhysics) Titanium-Sapphire (Ti:sapphire) laser has been used. This laser generates frequency-doubled laser light (barium borate crystal, BBO) at around 485 nm with a ~80 fs pulse at 80 MHz. The maximum power of this laser has been ~750 µW. For excitation of the other dye molecules, i.e. AF-532, AR-101 and RhB, a picosecond pulsed diode laser (PicoQuant) has been used. This laser diode generates laser light at 532 nm with a ~100 fs pulse at 80 MHz. The maximum power of this laser diode has been ~450 µW. The intensity of the respective excitation can be defined well by a continuous filter wheel that damps the laser power.

The setup consists of a confocal microscope with a lens mounted in an upward direction (z-axis), which can be controlled with a piezo element to focus the beam. The sample (either a dispersion in a cuvette or on a substrate) has been fixed on a piezo stage (x-y plane) that enables precise position adjustment. The luminescence of the sample is unidirectional and has been collected partly through the same lens and passes through a dichroic filter/beam splitter and a spatial filter to several detectors, e.g. a CCD camera or a spectrometer. Furthermore, the emission light can be guided to an avalanche photo diode (APD) to map the luminescence by scanning the substrate via the piezo stage (in the x-y plane), as was shown e.g. in chapter 4.2. The APD also enables lifetime measurements when the exponential decay of fluorescence is tracked over time in reference to a pulsed laser trigger signal. Moreover, an AFM can be

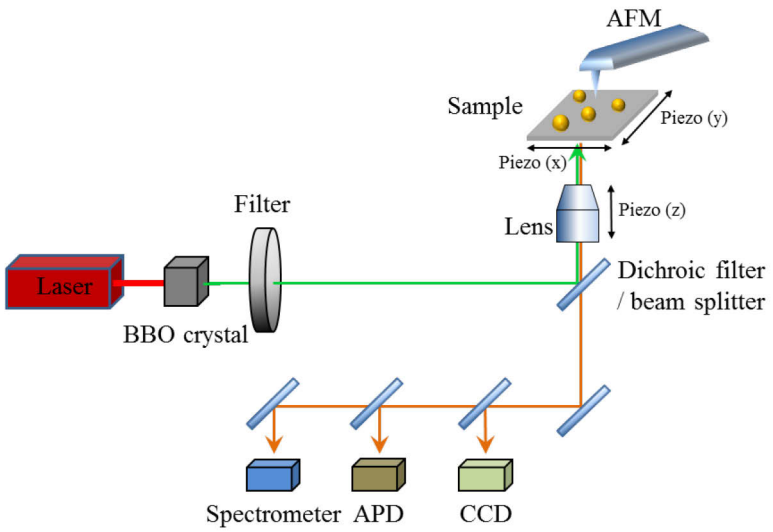

Figure 8.3: Laser setup established at the Humboldt University Berlin to analyse the hybrid nanoparticles. It consists of a confocal microscope, a piezo stage and several detection methods, i.e. a spectrometer, an avalanche photo diode (APD) and a camera (CCD). Optional an AFM can be mounted on top to correlate the optical signals with the topographic image.

mounted on top of the piezo stage to correlate the optical signals to a topographic image or manipulate them (e.g. moving single nanostructures).

Another laser setup has been established at the Max Born Institute with the help of Dr. Ingo Will. This setup was used to avoid the fast bleaching of dye molecules due to the high intensity of each pulse and high repetition rate of the aforementioned laser setup. The principle setup is similar to the one shown in Figure 8.3. A Neodyn YAG (Nd:YAG) laser was used with 25 ps pulses at 532 nm with very high pulse energies of up to 1 mJ/pulse. The repetition rate was extremely slow (1 – 50 Hz) to avoid fast bleaching and unrelaxed excited states before the new laser pulse hits the sample. To decrease any background signal, the spectrometer has been triggered by the laser pulse.

Lifetime measurements have been fitted with a double exponential decay function in Origin V8.6:

$$I(t) = I_0 + I_1 e^{-t/\tau_1} + I_2 e^{-t/\tau_2} \tag{8.7}$$

with an offset intensity I_0 and two decay rates τ_1 and τ_2 and their respective amplitudes I_1 and I_2. Average lifetimes have been calculated as:

$$\tau_{average} = \frac{I_1\tau_1^2 + I_2\tau_2^2}{I_1\tau_1 + I_2\tau_2}. \tag{8.8}$$

8.3.5 Structural characterization

X-ray photoelectron spectroscopy

X-ray photoelectron spectroscopy (XPS) is a surface sensitive technique that characterizes the chemical composition and oxidative state of an element via its binding energy ($E_{binding}$). XPS spectra are recorded by analysing the kinetic energy of electrons E_{kin} that have been generated by the photoelectric effect with an X-ray source that has a discrete photon energy E_{photon} ($E_{binding} = E_{photon} - E_{kin}$). XPS measurements have been conducted with a standard MgK_α X-ray source (E_{photon} = 1253.688 eV) and a standard hemispherical analyser both attached to the CISSY system located at BESSY II (Berlin, Germany). Due to non-conducting glass substrates the binding energies were calibrated using the carbon 1s line, assuming a binding energy of 284.8 eV for this purpose. Plot profiles were calculated using Voigt profiles in Origin V8.6.

X-ray diffraction

X-ray diffraction (XRD) analyses the structure of a crystal via diffraction of an incident beam at the regularly ordered atom lattice. The X-ray waves are elastically scattered at the electrons of an atom which form spherical waves near the scattering centre. A regular array like a crystal causes destructive and constructive interferences that can be determined by Bragg's law:

$$2d \sin\theta = n\lambda \tag{8.9}$$

with d the distance between each crystal plane, θ the scattering angle, n a positive integer and λ the X-ray wavelength. The peak that results from powder diffraction can be analysed regarding the crystal structure as well as the crystallinity. Imperfection of crystals and crystals that are smaller than 0.2 µm experience a broadening of the XRD peak.[309] Crystallite sizes L have been calculated with the Scherrer equation:

$$\Delta = \frac{K\lambda}{L\cos\theta} \tag{8.10}$$

where K is a shape factor with a value assuming 0.9. Δ is the full width at half maximum (FWHM) in radians of a certain peak at a given Bragg angle 2θ.

The XRD measurements were conducted with a Bruker D8-Advance X-ray diffractometer using a CuK_α X-ray source (λ = 1.5406 Å). Plot profiles were calculated using a pseudo-Voigt profile in Origin V8.6.

Thermogravimetric analysis

Thermogravimetric analysis (TGA) is a method to analyse physical and chemical properties with increasing temperature. Processes like solvent desorption, phase transitions, sublimation or decomposition can be monitored as a function of the temperature. Such processes can be followed by measuring the change in mass in respect to the temperature. A high precision balance and well controlled furnace are needed. TGA measurements have been performed with a NETZSCH STA 409 PC/PG with a temperature ramp of 6 K/min under argon flow. At least 20 mg of the dried sample has been loaded inside the crucible, which has been heated to 800 °C for 6 h prior use to avoid any contamination.

Nuclear magnetic resonance

Nuclear magnetic resonance (NMR) is a spectroscopic technique that investigates the electronic environment and interactions of atoms with its neighbouring atoms. It is a powerful tool for structure analysis of organic (and partly inorganic) compounds. ^{13}C-NMR spectra have been recorded with a Bruker AV 500 spectrometer at 500 MHz at room temperature. 15 mg of the respective sample has been lyophilised and dissolved in 0.6 ml deuterated chloroform (PS-MPS-PS) or toluene (PS-MPS-PMMA). The cross-linked PS-MPS shell cannot be dissolved and has been separated via centrifugation.

8.3.6 *I-V* curves to measure solar cell properties

Current−voltage (*I-V*) measurements of perovskite solar cells were performed using a Steuernagel Lichttechnik sun simulator, mimicking an AM 1.5G spectra. The size of the perovskite solar cell has been 0.16 cm^2 in the case of the Au reference electrode. All *I-V* measurements were performed in forward (from negative to positive) and reverse directions.

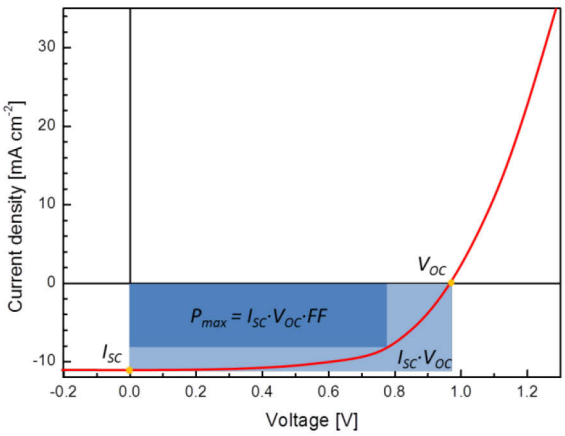

Figure 8.4: Typical *I-V* measurement and the derived values to calculate the efficiency of a solar cell.

A delay time of 40 ms with a 20 ms acquisition time, corresponding to a scan speed of 0.167 Vs^{-1}, was chosen. The solar cell performance is done by scanning an applied voltage across the solar cell and measuring the current response. The *I-V* curve is acquired by plotting the current versus the applied voltage (Figure 8.4) that enables to derive the key parameters of the solar cell performance. The open circuit voltage V_{OC} is the maximum voltage that the solar cell will supply. The short circuit current I_{SC} is the maximum current of the solar cell of a zero resistance load. The fill factor *FF* is a factor determined by the maximum power of a solar cell in respect to the product of V_{OC} and I_{SC}. The efficiency of the solar cell is defined as:

$$\eta = \frac{P_{max}}{P_{in}} = \frac{V_{OC} I_{SC} FF}{P_{in}} \tag{8.11}$$

with P_{max} the maximum power generated by the solar cell and P_{in} the input power of the light source.

Bibliography

[1] IUPAC; *Compendium of Macromolecular Nomenclature. (The IUPAC 'Purple Book')*: Blackwell Scientific Publications, Ltd.); **1991**.

[2] Abbe E.; Beiträge zur Theorie des Mikroskops und der mikroskopischen Wahrnehmung; *Archiv f. mikrosk. Anatomie* **9** 418-468, (1873).

[3] Brill R.H. and Cahill N.D.; A Red Qpaque Glass From Sardis And Some Thoughts On Red Opaques In General; *The Journal of Glass Studies* **30** 16 - 27, (1988).

[4] Freestone I., Meeks N., Sax M. and Higgitt C.; The Lycurgus Cup — A Roman nanotechnology; *Gold Bull* **40** 270-277, (2007).

[5] Faraday M.; The Bakerian Lecture: Experimental Relations of Gold (and Other Metals) to Light; *Philosophical Transactions of the Royal Society of London* **147** 145-181, (1857).

[6] Zsigmondy R.; Ueber wässrige Lösungen metallischen Goldes; *Justus Liebigs Annalen der Chemie* **301** 29-54, (1898).

[7] Siedentopf H. and Zsigmondy R.; Uber Sichtbarmachung und Größenbestimmung ultramikoskopischer Teilchen, mit besonderer Anwendung auf Goldrubingläser; *Annalen der Physik* **315** 1-39, (1902).

[8] Maxwell J.C.; A Dynamical Theory of the Electromagnetic Field; *Philosophical Transactions of the Royal Society of London* **155** 459-512, (1865).

[9] Mie G.; Beiträge zur Optik trüber Medien, speziell kolloidaler Metallösungen; *Annalen der Physik* **330** 377-445, (1908).

[10] Ritchie R.H.; Plasma Losses by Fast Electrons in Thin Films; *Physical Review* **106** 874-881, (1957).

[11] Kretschmann E.; Die Bestimmung optischer Konstanten von Metallen durch Anregung von Oberflächenplasmaschwingungen; *Z. Physik* **241** 313-324, (1971).

[12] Ritchie R.H., Arakawa E.T., Cowan J.J. and Hamm R.N.; Surface-Plasmon Resonance Effect in Grating Diffraction; *Physical Review Letters* **21** 1530-1533, (1968).

[13] Fleischmann M., Hendra P.J. and McQuillan A.J.; Raman spectra of pyridine adsorbed at a silver electrode; *Chemical Physics Letters* **26** 163-166, (1974).

[14] Moskovits M.; Surface-enhanced spectroscopy; *Reviews of Modern Physics* **57** 783-826, (1985).

[15] Aroca R.F., Alvarez-Puebla R.A., Pieczonka N., Sanchez-Cortez S. and Garcia-Ramos J.V.; Surface-enhanced Raman scattering on colloidal nanostructures; *Advances in Colloid and Interface Science* **116** 45-61, (2005).

[16] Willets K.A. and Van Duyne R.P.; Localized Surface Plasmon Resonance Spectroscopy and Sensing; *Annual Review of Physical Chemistry* **58** 267-297, (2007).

[17] Mayer K.M. and Hafner J.H.; Localized Surface Plasmon Resonance Sensors; *Chemical Reviews* **111** 3828-3857, (2011).

[18] Lewis A., Isaacson M., Harootunian A. and Muray A.; Development of a 500 Å spatial resolution light microscope: I. light is efficiently transmitted through λ/16 diameter apertures; *Ultramicroscopy* **13** 227-231, (1984).

[19] Pohl D.W., Denk W. and Lanz M.; Optical stethoscopy: Image recording with resolution λ/20; *Applied Physics Letters* **44** 651-653, (1984).

[20] Hartschuh A.; Tip-Enhanced Near-Field Optical Microscopy; *Angewandte Chemie International Edition* **47** 8178-8191, (2008).

[21] Chen J., Jin Y., Fahruddin N. and Zhao J.X.; Development of Gold Nanoparticle-Enhanced Fluorescent Nanocomposites; *Langmuir* **29** 1584-1591, (2013).

[22] Geddes C. and Lakowicz J.; Editorial: Metal-Enhanced Fluorescence; *J Fluoresc* **12** 121-129, (2002).

[23] Aslan K., Gryczynski I., Malicka J., Matveeva E., Lakowicz J.R. and Geddes C.D.; Metal-enhanced fluorescence: an emerging tool in biotechnology; *Current Opinion in Biotechnology* **16** 55-62, (2005).

[24] Schneider G., Decher G., Nerambourg N., Praho R., Werts M.H.V. and Blanchard-Desce M.; Distance-Dependent Fluorescence Quenching on Gold Nanoparticles Ensheathed with Layer-by-Layer Assembled Polyelectrolytes; *Nano Letters* **6** 530-536, (2006).

[25] Aslan K., Wu M., Lakowicz J.R. and Geddes C.D.; Fluorescent Core−Shell Ag@SiO2 Nanocomposites for Metal-Enhanced Fluorescence and Single Nanoparticle Sensing Platforms; *Journal of the American Chemical Society* **129** 1524-1525, (2007).

[26] Tovmachenko O.G., Graf C., van den Heuvel D.J., van Blaaderen A. and Gerritsen H.C.; Fluorescence Enhancement by Metal-Core/Silica-Shell Nanoparticles; *Advanced Materials* **18** 91-95, (2006).

[27] Atwater H.A. and Polman A.; Plasmonics for improved photovoltaic devices; *Nat Mater* **9** 205-213, (2010).

[28] Catchpole K.R., Mokkapati S., Beck F., Wang E.C., McKinley A., Basch A. and Lee J.; Plasmonics and nanophotonics for photovoltaics; *Mrs Bull* **36** 461-467, (2011).

[29] Zhou N., Lopez-Puente V., Wang Q., Polavarapu L., Pastoriza-Santos I. and Xu Q.-H.; Plasmon-enhanced light harvesting: applications in enhanced photocatalysis, photodynamic therapy and photovoltaics; *RSC Advances* **5** 29076-29097, (2015).

[30] Bergman D.J. and Stockman M.I.; Surface plasmon amplification by stimulated emission of radiation: Quantum generation of coherent surface plasmons in nanosystems; *Physical Review Letters* **90** 0274021-0274024, (2003).

[31] Noginov M.A., Zhu G., Belgrave A.M., Bakker R., Shalaev V.M., Narimanov E.E., Stout S., Herz E., Suteewong T. and Wiesner U.; Demonstration of a spaser-based nanolaser; *Nature* **460** 1110-1112, (2009).

[32] Peng B., Zhang Q., Liu X., Ji Y., Demir H.V., Huan C.H.A., Sum T.C. and Xiong Q.; Fluorophore-Doped Core–Multishell Spherical Plasmonic Nanocavities: Resonant Energy Transfer toward a Loss Compensation; *ACS Nano* **6** 6250-6259, (2012).

[33] De Luca A., Grzelczak M.P., Pastoriza-Santos I., Liz-Marzán L.M., La Deda M., Striccoli M. and Strangi G.; Dispersed and Encapsulated Gain Medium in Plasmonic Nanoparticles: a Multipronged Approach to Mitigate Optical Losses; *ACS Nano* **5** 5823-5829, (2011).

[34] Juan M.L., Righini M. and Quidant R.; Plasmon nano-optical tweezers; *Nat Photon* **5** 349-356, (2011).

[35] Liu Y. and Zhang X.; Metamaterials: a new frontier of science and technology; *Chemical Society Reviews* **40** 2494-2507, (2011).

[36] Xuming Z., Yu Lim C., Ru-Shi L. and Din Ping T.; Plasmonic photocatalysis; *Reports on Progress in Physics* **76** 046401, (2013).

[37] Astruc D., Lu F. and Aranzaes J.R.; Nanoparticles as Recyclable Catalysts: The Frontier between Homogeneous and Heterogeneous Catalysis; *Angewandte Chemie International Edition* **44** 7852-7872, (2005).

[38] Gu S., Kaiser J., Marzun G., Ott A., Lu Y., Ballauff M., Zaccone A., Barcikowski S. and Wagener P.; Ligand-free Gold Nanoparticles as a Reference Material for Kinetic Modelling of Catalytic Reduction of 4-Nitrophenol; *Catal Lett* **145** 1105-1112, (2015).

[39] Zhang Q., Uchaker E., Candelaria S.L. and Cao G.; Nanomaterials for energy conversion and storage; *Chemical Society Reviews* **42** 3127-3171, (2013).

[40] Jain P.K., Huang X.H., El-Sayed I.H. and El-Sayed M.A.; Noble Metals on the Nanoscale: Optical and Photothermal Properties and Some Applications in Imaging, Sensing, Biology, and Medicine; *Accounts of Chemical Research* **41** 1578-1586, (2008).

[41] Portney N. and Ozkan M.; Nano-oncology: drug delivery, imaging, and sensing; *Anal Bioanal Chem* **384** 620-630, (2006).

[42] Thanh N.T.K. and Green L.A.W.; Functionalisation of nanoparticles for biomedical applications; *Nano Today* **5** 213-230, (2010).

[43] Tong L., Wei Q., Wei A. and Cheng J.-X.; Gold Nanorods as Contrast Agents for Biological Imaging: Optical Properties, Surface Conjugation and Photothermal Effects†; *Photochemistry and Photobiology* **85** 21-32, (2009).

[44] Otsuka H., Nagasaki Y. and Kataoka K.; PEGylated nanoparticles for biological and pharmaceutical applications; *Advanced Drug Delivery Reviews* **55** 403-419, (2003).

[45] Oulton R.F.; Surface plasmon lasers: sources of nanoscopic light; *Materials Today* **15** 26-34, (2012).

[46] Hartland G.V.; Optical Studies of Dynamics in Noble Metal Nanostructures; *Chemical Reviews* **111** 3858-3887, (2011).

[47] Pelton M. and Bryant G.; *Introduction to Metal-Nanoparticle Plasmonics*; (Hoboken, New Jersey: John Wiley & Sons, Inc.); **2013**.

[48] Schuller J.A., Barnard E.S., Cai W., Jun Y.C., White J.S. and Brongersma M.L.; Plasmonics for extreme light concentration and manipulation; *Nat Mater* **9** 193-204, (2010).

[49] Berini P. and De Leon I.; Surface plasmon-polariton amplifiers and lasers; *Nat Photon* **6** 16-24, (2012).

[50] Oulton R.F., Sorger V.J., Zentgraf T., Ma R.-M., Gladden C., Dai L., Bartal G. and Zhang X.; Plasmon lasers at deep subwavelength scale; *Nature* **461** 629-632, (2009).

[51] Lu Y.-J., Kim J., Chen H.-Y., Wu C., Dabidian N., Sanders C.E., Wang C.-Y., Lu M.-Y., Li B.-H., Qiu X., Chang W.-H., Chen L.-J., Shvets G., Shih C.-K. and Gwo S.; Plasmonic Nanolaser Using Epitaxially Grown Silver Film; *Science* **337** 450-453, (2012).

[52] Hou Y., Renwick P., Liu B., Bai J. and Wang T.; Room temperature plasmonic lasing in a continuous wave operation mode from an InGaN/GaN single nanorod with a low threshold; *Scientific Reports* **4** 5014, (2014).

[53] Lu Y.-J., Wang C.-Y., Kim J., Chen H.-Y., Lu M.-Y., Chen Y.-C., Chang W.-H., Chen L.-J., Stockman M.I., Shih C.-K. and Gwo S.; All-Color Plasmonic Nanolasers with Ultralow Thresholds: Autotuning Mechanism for Single-Mode Lasing; *Nano Letters* **14** 4381-4388, (2014).

[54] Sidiropoulos T.P.H., Roder R., Geburt S., Hess O., Maier S.A., Ronning C. and Oulton R.F.; Ultrafast plasmonic nanowire lasers near the surface plasmon frequency; *Nat Phys* **10** 870-876, (2014).

[55] Zhang Q., Li G., Liu X., Qian F., Li Y., Sum T.C., Lieber C.M. and Xiong Q.; A room temperature low-threshold ultraviolet plasmonic nanolaser; *Nat Commun* **5**2014).

[56] International Energy Agency; *Key World Energy Statistics 2014*; (Paris, France); **2014**.

[57] European Photovoltaic Industry Association; *Global Market Outlook For Solar Power / 2015 - 2019*; (Brussels, Belgium); **2014**.

[58] Frauenhofer Institute for Solar Energy Systems ISE; *Photovoltaics Report*; (Freiburg, Germany); **2015**.

[59] Ott A., Ring S., Yin G., Calvet W., Stannowski B., Lu Y., Schlatmann R. and Ballauff M.; Efficient plasmonic scattering of colloidal silver particles through annealing-induced changes; *Nanotechnology* **25** 455706, (2014).

[60] Nathan C.L., Prashant N., Kevin M.M., David J.N. and Sang-Hyun O.; Engineering metallic nanostructures for plasmonics and nanophotonics; *Reports on Progress in Physics* **75** 036501, (2012).

[61] Broers A.N., Molzen W.W., Cuomo J.J. and Wittels N.D.; Electron-beam fabrication of 80-Å metal structures; *Applied Physics Letters* **29** 596-598, (1976).

[62] Ampere A.T.; Recent developments in micromilling using focused ion beam technology; *Journal of Micromechanics and Microengineering* **14** R15, (2004).

[63] Gates B.D., Xu Q., Stewart M., Ryan D., Willson C.G. and Whitesides G.M.; New Approaches to Nanofabrication: Molding, Printing, and Other Techniques; *Chemical Reviews* **105** 1171-1196, (2005).

[64] Suryanarayana C.; Mechanical alloying and milling; *Progress in Materials Science* **46** 1-184, (2001).

[65] Turkevich J., Stevenson P.C. and Hillier J.; A Study of the Nucleation and Growth Processes in the Synthesis of Colloidal Gold; *Discussions of the Faraday Society* 55-&, (1951).

[66] Frens G.; Particle size and sol stability in metal colloids; *Kolloid-Z.u.Z.Polymere* **250** 736-741, (1972).

[67] Frens G.; Controlled Nucleation for the Regulation of the Particle Size in Monodisperse Gold Suspensions; *Nature, Phys. Sci.* **241** 20-22, (1973).

[68] Lee P.C. and Meisel D.; Adsorption and surface-enhanced Raman of dyes on silver and gold sols; *The Journal of Physical Chemistry* **86** 3391-3395, (1982).

[69] Steinigeweg D. and Schlucker S.; Monodispersity and size control in the synthesis of 20-100 nm quasi-spherical silver nanoparticles by citrate and ascorbic acid reduction in glycerol-water mixtures; *Chemical Communications* **48** 8682-8684, (2012).

[70] Wan Y., Guo Z., Jiang X., Fang K., Lu X., Zhang Y. and Gu N.; Quasi-spherical silver nanoparticles: Aqueous synthesis and size control by the seed-mediated Lee–Meisel method; *Journal of Colloid and Interface Science* **394** 263-268, (2013).

[71] Bastús N.G., Comenge J. and Puntes V.; Kinetically Controlled Seeded Growth Synthesis of Citrate-Stabilized Gold Nanoparticles of up to 200 nm: Size Focusing versus Ostwald Ripening; *Langmuir* **27** 11098-11105, (2011).

[72] Gao J., Bender C.M. and Murphy C.J.; Dependence of the Gold Nanorod Aspect Ratio on the Nature of the Directing Surfactant in Aqueous Solution; *Langmuir* **19** 9065-9070, (2003).

[73] Meena S.K. and Sulpizi M.; Understanding the Microscopic Origin of Gold Nanoparticle Anisotropic Growth from Molecular Dynamics Simulations; *Langmuir* **29** 14954-14961, (2013).

[74] Nikoobakht B. and El-Sayed M.A.; Preparation and Growth Mechanism of Gold Nanorods (NRs) Using Seed-Mediated Growth Method; *Chemistry of Materials* **15** 1957-1962, (2003).

[75] Mohanty U.S.; Electrodeposition: a versatile and inexpensive tool for the synthesis of nanoparticles, nanorods, nanowires, and nanoclusters of metals; *J Appl Electrochem* **41** 257-270, (2011).

[76] Yu, Chang S.-S., Lee C.-L. and Wang C.R.C.; Gold Nanorods: Electrochemical Synthesis and Optical Properties; *The Journal of Physical Chemistry B* **101** 6661-6664, (1997).

[77] Sharma D.K., Ott A., O'Mullane A.P. and Bhargava S.K.; The facile formation of silver dendritic structures in the absence of surfactants and their electrochemical and SERS properties; *Colloids and Surfaces A: Physicochemical and Engineering Aspects* **386** 98-106, (2011).

[78] van der Zande B.M.I., Böhmer M.R., Fokkink L.G.J. and Schönenberger C.; Aqueous Gold Sols of Rod-Shaped Particles; *The Journal of Physical Chemistry B* **101** 852-854, (1997).

[79] Ott A., Jones L.A. and Bhargava S.K.; Direct electrodeposition of porous platinum honeycomb structures; *Electrochemistry Communications* **13** 1248-1251, (2011).

[80] Tao A.R., Habas S. and Yang P.; Shape Control of Colloidal Metal Nanocrystals; *Small* **4** 310-325, (2008).

[81] Park J.C., Kim J., Kwon H. and Song H.; Gram-Scale Synthesis of Cu2O Nanocubes and Subsequent Oxidation to CuO Hollow Nanostructures for Lithium-Ion Battery Anode Materials; *Advanced Materials* **21** 803-807, (2009).

[82] Wierenga A.M., Lenstra T.A.J. and Philipse A.P.; Aqueous dispersions of colloidal gibbsite platelets: synthesis, characterisation and intrinsic viscosity measurements; *Colloids and Surfaces A: Physicochemical and Engineering Aspects* **134** 359-371, (1998).

[83] Kumar S. and Nann T.; Shape Control of II–VI Semiconductor Nanomaterials; *Small* **2** 316-329, (2006).

[84] Ghosh S.K. and Pal T.; Interparticle Coupling Effect on the Surface Plasmon Resonance of Gold Nanoparticles: From Theory to Applications; *Chemical Reviews* **107** 4797-4862, (2007).

[85] Khlebtsov B.N., Khanadeyev V.A., Ye J., Mackowski D.W., Borghs G. and Khlebtsov N.G.; Coupled plasmon resonances in monolayers of metal nanoparticles and nanoshells; *Physical Review B* **77** 035440, (2008).

[86] Banerjee I.A., Yu L. and Matsui H.; Cu nanocrystal growth on peptide nanotubes by biomineralization: Size control of Cu nanocrystals by tuning peptide conformation; *Proceedings of the National Academy of Sciences* **100** 14678-14682, (2003).

[87] Brown S., Sarikaya M. and Johnson E.; A genetic analysis of crystal growth1; *Journal of Molecular Biology* **299** 725-735, (2000).

[88] Naik R.R., Stringer S.J., Agarwal G., Jones S.E. and Stone M.O.; Biomimetic synthesis and patterning of silver nanoparticles; *Nat Mater* **1** 169-172, (2002).

[89] Shan J. and Tenhu H.; Recent advances in polymer protected gold nanoparticles: synthesis, properties and applications; *Chemical Communications* 4580-4598, (2007).

[90] McLeod M.C., McHenry R.S., Beckman E.J. and Roberts C.B.; Synthesis and Stabilization of Silver Metallic Nanoparticles and Premetallic Intermediates in Perfluoropolyether/CO2 Reverse Micelle Systems; *The Journal of Physical Chemistry B* **107** 2693-2700, (2003).

[91] Seregina M.V., Bronstein L.M., Platonova O.A., Chernyshov D.M., Valetsky P.M., Hartmann J., Wenz E. and Antonietti M.; Preparation of Noble-Metal Colloids in Block Copolymer Micelles and Their Catalytic Properties in Hydrogenation; *Chemistry of Materials* **9** 923-931, (1997).

[92] Taleb A., Petit C. and Pileni M.P.; Synthesis of Highly Monodisperse Silver Nanoparticles from AOT Reverse Micelles: A Way to 2D and 3D Self-Organization; *Chemistry of Materials* **9** 950-959, (1997).

[93] Wu C., Szymanski C. and McNeill J.; Preparation and Encapsulation of Highly Fluorescent Conjugated Polymer Nanoparticles; *Langmuir* **22** 2956-2960, (2006).

[94] Wu S., Dzubiella J., Kaiser J., Drechsler M., Guo X., Ballauff M. and Lu Y.; Thermosensitive Au-PNIPA Yolk–Shell Nanoparticles with Tunable Selectivity for Catalysis; *Angewandte Chemie International Edition* **51** 2229-2233, (2012).

[95] Lu Y. and Ballauff M.; Thermosensitive core–shell microgels: From colloidal model systems to nanoreactors; *Progress in Polymer Science* **36** 767-792, (2011).

[96] Ballauff M. and Lu Y.; "Smart" nanoparticles: Preparation, characterization and applications; *Polymer* **48** 1815-1823, (2007).

[97] Mulvaney P., Liz-Marzan L.M., Giersig M. and Ung T.; Silica encapsulation of quantum dots and metal clusters; *Journal of Materials Chemistry* **10** 1259-1270, (2000).

[98] Stöber W., Fink A. and Bohn E.; Controlled growth of monodisperse silica spheres in the micron size range; *Journal of Colloid and Interface Science* **26** 62-69, (1968).

[99] Arifin E. and Lee j.-K.; The Distance-Dependent Fluorescence Enhancement Phenomena in Uniform Size Ag@SiO2@SiO2(dye) Nanocomposites; *Bulletin of the Korean Chemical Society* **34** 539 - 544, (2013).

[100] Van Blaaderen A. and Vrij A.; Synthesis and characterization of colloidal dispersions of fluorescent, monodisperse silica spheres; *Langmuir* **8** 2921-2931, (1992).

[101] Contreras-Cáceres R., Sánchez-Iglesias A., Karg M., Pastoriza-Santos I., Pérez-Juste J., Pacifico J., Hellweg T., Fernández-Barbero A. and Liz-Marzán L.M.; Encapsulation and Growth of Gold Nanoparticles in Thermoresponsive Microgels; *Advanced Materials* **20** 1666-1670, (2008).

[102] Wu S., Kaiser J., Drechsler M., Ballauff M. and Lu Y.; Thermosensitive Au-PNIPA yolk-shell particles as "nanoreactors" with tunable optical properties; *Colloid Polym Sci* **291** 231-237, (2013).

[103] Álvarez-Puebla R.A., Contreras-Cáceres R., Pastoriza-Santos I., Pérez-Juste J. and Liz-Marzán L.M.; Au@pNIPAM Colloids as Molecular Traps for Surface-Enhanced, Spectroscopic, Ultra-Sensitive Analysis; *Angewandte Chemie International Edition* **48** 138-143, (2009).

[104] Katsumoto Y., Tanaka T., Sato H. and Ozaki Y.; Conformational Change of Poly(N-isopropylacrylamide) during the Coil−Globule Transition Investigated by Attenuated Total Reflection/Infrared Spectroscopy and Density Functional Theory Calculation†; *The Journal of Physical Chemistry A* **106** 3429-3435, (2002).

[105] Simmons D.S. and Sanchez I.C.; A Model for a Thermally Induced Polymer Coil-to-Globule Transition; *Macromolecules* **41** 5885-5889, (2008).

[106] Heskins M. and Guillet J.E.; Solution Properties of Poly(N-isopropylacrylamide); *Journal of Macromolecular Science: Part A - Chemistry* **2** 1441-1455, (1968).

[107] Contreras-Cáceres R., Pastoriza-Santos I., Alvarez-Puebla R.A., Pérez-Juste J., Fernández-Barbero A. and Liz-Marzán L.M.; Growing Au/Ag Nanoparticles within Microgel Colloids for Improved Surface-Enhanced Raman Scattering Detection; *Chemistry – A European Journal* **16** 9462-9467, (2010).

[108] Povolotskaya A.V., Povolotskiy A.V. and Manshina A.A.; Hybrid nanostructures: synthesis, morphology and functional properties; *Russian Chemical Reviews* **84** 579, (2015).

[109] Song H.; Metal Hybrid Nanoparticles for Catalytic Organic and Photochemical Transformations; *Accounts of Chemical Research* **48** 491-499, (2015).

[110] Xu Y., Chen L., Wang X., Yao W. and Zhang Q.; Recent advances in noble metal based composite nanocatalysts: colloidal synthesis, properties, and catalytic applications; *Nanoscale* **7** 10559-10583, (2015).

[111] Thomas V., Namdeo M., Murali Mohan Y., Bajpai S.K. and Bajpai M.; Review on Polymer, Hydrogel and Microgel Metal Nanocomposites: A Facile Nanotechnological Approach; *Journal of Macromolecular Science, Part A* **45** 107-119, (2007).

[112] Wang T.C., Chen B., Rubner M.F. and Cohen R.E.; Selective Electroless Nickel Plating on Polyelectrolyte Multilayer Platforms; *Langmuir* **17** 6610-6615, (2001).

[113] Wang T.C., Rubner M.F. and Cohen R.E.; Polyelectrolyte Multilayer Nanoreactors for Preparing Silver Nanoparticle Composites: Controlling Metal Concentration and Nanoparticle Size; *Langmuir* **18** 3370-3375, (2002).

[114] Bohm D. and Pines D.; A Collective Description of Electron Interactions. I. Magnetic Interactions; *Physical Review* **82** 625-634, (1951).

[115] Pines D.; A Collective Description of Electron Interactions: IV. Electron Interaction in Metals; *Physical Review* **92** 626-636, (1953).

[116] Kühnle A.; Self-assembly of organic molecules at metal surfaces; *Current Opinion in Colloid & Interface Science* **14** 157-168, (2009).

[117] Lavrich D.J., Wetterer S.M., Bernasek S.L. and Scoles G.; Physisorption and Chemisorption of Alkanethiols and Alkyl Sulfides on Au(111); *The Journal of Physical Chemistry B* **102** 3456-3465, (1998).

[118] Du X. and He J.; Amino-functionalized silica nanoparticles with center-radially hierarchical mesopores as ideal catalyst carriers; *Nanoscale* **4** 852-859, (2012).

[119] Oldenburg S.J., Westcott S.L., Averitt R.D. and Halas N.J.; Surface enhanced Raman scattering in the near infrared using metal nanoshell substrates; *The Journal of Chemical Physics* **111** 4729-4735, (1999).

[120] Lu Z., Goebl J., Ge J. and Yin Y.; Self-assembly and tunable plasmonic property of gold nanoparticles on mercapto-silica microspheres; *Journal of Materials Chemistry* **19** 4597-4602, (2009).

[121] Mei Y., Sharma G., Lu Y., Ballauff M., Drechsler M., Irrgang T. and Kempe R.; High Catalytic Activity of Platinum Nanoparticles Immobilized on Spherical Polyelectrolyte Brushes; *Langmuir* **21** 12229-12234, (2005).

[122] Schrinner M., Polzer F., Mei Y., Lu Y., Haupt B., Ballauff M., Göldel A., Drechsler M., Preussner J. and Glatzel U.; Mechanism of the Formation of Amorphous Gold Nanoparticles within Spherical Polyelectrolyte Brushes; *Macromolecular Chemistry and Physics* **208** 1542-1547, (2007).

[123] Davies P.T. and Vincent B.; Uptake of anionic gold nanoparticles by cationic microgel particles in dispersion: The effect of pH; *Colloids and Surfaces A: Physicochemical and Engineering Aspects* **354** 99-105, (2010).

[124] Mei Y., Lu Y., Polzer F., Ballauff M. and Drechsler M.; Catalytic Activity of Palladium Nanoparticles Encapsulated in Spherical Polyelectrolyte Brushes and Core−Shell Microgels; *Chemistry of Materials* **19** 1062-1069, (2007).

[125] Jia H., Schmitz D., Ott A., Pich A. and Lu Y.; Cyclodextrin modified microgels as "nanoreactor" for the generation of Au nanoparticles with enhanced catalytic activity; *Journal of Materials Chemistry A* **3** 6187-6195, (2015).

[126] Oldenburg S.J., Averitt R.D., Westcott S.L. and Halas N.J.; Nanoengineering of optical resonances; *Chemical Physics Letters* **288** 243-247, (1998).

[127] Yong K.-T., Sahoo Y., Swihart M.T. and Prasad P.N.; Synthesis and plasmonic properties of silver and gold nanoshells on polystyrene cores of different size and of gold–silver core–shell nanostructures; *Colloids and Surfaces A: Physicochemical and Engineering Aspects* **290** 89-105, (2006).

[128] de Gennes P.-G.; Soft Matter (Nobel Lecture); *Angewandte Chemie International Edition in English* **31** 842-845, (1992).

[129] Mock E.B. and Zukoski C.F.; Emulsion Polymerization Routes to Chemically Anisotropic Particles; *Langmuir* **26** 13747-13750, (2010).

[130] Park J.-G., Forster J.D. and Dufresne E.R.; High-Yield Synthesis of Monodisperse Dumbbell-Shaped Polymer Nanoparticles; *Journal of the American Chemical Society* **132** 5960-5961, (2010).

[131] Kim J.-W., Larsen R.J. and Weitz D.A.; Synthesis of Nonspherical Colloidal Particles with Anisotropic Properties; *Journal of the American Chemical Society* **128** 14374-14377, (2006).

[132] Peng B., Vutukuri H.R., van Blaaderen A. and Imhof A.; Synthesis of fluorescent monodisperse non-spherical dumbbell-like model colloids; *Journal of Materials Chemistry* **22** 21893-21900, (2012).

[133] Yoon K., Lee D., Kim J.W., Kim J. and Weitz D.A.; Asymmetric functionalization of colloidal dimer particles with gold nanoparticles; *Chemical Communications* **48** 9056-9058, (2012).

[134] Johnson P.B. and Christy R.W.; Optical Constants of the Noble Metals; *Physical Review B* **6** 4370-4379, (1972).

[135] Olmon R.L., Slovick B., Johnson T.W., Shelton D., Oh S.-H., Boreman G.D. and Raschke M.B.; Optical dielectric function of gold; *Physical Review B* **86** 235147, (2012).

[136] Barnes W.L., Dereux A. and Ebbesen T.W.; Surface plasmon subwavelength optics; *Nature* **424** 824-830, (2003).

[137] Anatoly V.Z. and Igor I.S.; Near-field photonics: surface plasmon polaritons and localized surface plasmons; *Journal of Optics A: Pure and Applied Optics* **5** S16, (2003).

[138] Alexander P.D.; Nanoparticles and nanocomposites for fluorescence sensing and imaging; *Methods and Applications in Fluorescence* **1** 022001, (2013).

[139] Malitson I.H.; Interspecimen Comparison of the Refractive Index of Fused Silica; *J. Opt. Soc. Am.* **55** 1205-1208, (1965).

[140] Jain P.K. and El-Sayed M.A.; Plasmonic coupling in noble metal nanostructures; *Chemical Physics Letters* **487** 153-164, (2010).

[141] Gans R.; Über die Form ultramikroskopischer Goldteilchen; *Annalen der Physik* **342** 881-900, (1912).

[142] Kelly K.L., Coronado E., Zhao L.L. and Schatz G.C.; The Optical Properties of Metal Nanoparticles: The Influence of Size, Shape, and Dielectric Environment; *The Journal of Physical Chemistry B* **107** 668-677, (2003).

[143] Miller E.K.; Time-domain modeling in electromagnetics; *Journal of Electromagnetic Waves and Applications* **8** 1125-1172, (1994).

[144] Yang W.H., Schatz G.C. and Van Duyne R.P.; Discrete dipole approximation for calculating extinction and Raman intensities for small particles with arbitrary shapes; *The Journal of Chemical Physics* **103** 869-875, (1995).

[145] Jain P.K., Lee K.S., El-Sayed I.H. and El-Sayed M.A.; Calculated Absorption and Scattering Properties of Gold Nanoparticles of Different Size, Shape, and Composition: Applications in Biological Imaging and Biomedicine; *The Journal of Physical Chemistry B* **110** 7238-7248, (2006).

[146] Pelton M., Aizpurua J. and Bryant G.; Metal-nanoparticle plasmonics; *Laser & Photonics Reviews* **2** 136-159, (2008).

[147] Etchegoin P., Cohen L.F., Hartigan H., Brown R.J.C., Milton M.J.T. and Gallop J.C.; Electromagnetic contribution to surface enhanced Raman scattering revisited; *The Journal of Chemical Physics* **119** 5281-5289, (2003).

[148] Chen C.J. and Osgood R.M.; Direct Observation of the Local-Field-Enhanced Surface Photochemical Reactions; *Physical Review Letters* **50** 1705-1708, (1983).

[149] Nitzan A. and Brus L.E.; Theoretical model for enhanced photochemistry on rough surfaces; *The Journal of Chemical Physics* **75** 2205-2214, (1981).

[150] Baffou G., Kreuzer M.P., Kulzer F. and Quidant R.; Temperature mapping near plasmonic nanostructures using fluorescence polarization anisotropy; *Opt. Express* **17** 3291-3298, (2009).

[151] Hirsch L.R., Stafford R.J., Bankson J.A., Sershen S.R., Rivera B., Price R.E., Hazle J.D., Halas N.J. and West J.L.; Nanoshell-mediated near-infrared thermal therapy of tumors under magnetic resonance guidance; *Proceedings of the National Academy of Sciences* **100** 13549-13554, (2003).

[152] Purcell E.M., Torrey H.C. and Pound R.V.; Resonance Absorption by Nuclear Magnetic Moments in a Solid; *Physical Review* **69** 37-38, (1946).

[153] Carminati R., Greffet J.J., Henkel C. and Vigoureux J.M.; Radiative and non-radiative decay of a single molecule close to a metallic nanoparticle; *Optics Communications* **261** 368-375, (2006).

[154] Colas des Francs G., Bouhelier A., Finot E., Weeber J.C., Dereux A., Girard C. and Dujardin E.; Fluorescence relaxation in the near–field of a mesoscopic metallic

particle: distance dependence and role of plasmon modes; *Opt. Express* **16** 17654-17666, (2008).

[155] Kinkhabwala A., Yu Z., Fan S., Avlasevich Y., Mullen K. and Moerner W.E.; Large single-molecule fluorescence enhancements produced by a bowtie nanoantenna; *Nat Photon* **3** 654-657, (2009).

[156] Stockman M.I.; Spasers explained; *Nat Photon* **2** 327-329, (2008).

[157] Mark I.S.; The spaser as a nanoscale quantum generator and ultrafast amplifier; *Journal of Optics* **12** 024004, (2010).

[158] Stockman M.I.; Nanoplasmonics: past, present, and glimpse into future; *Opt. Express* **19** 22029-22106, (2011).

[159] Liu S.-Y., Li J., Zhou F., Gan L. and Li Z.-Y.; Efficient surface plasmon amplification from gain-assisted gold nanorods; *Optics Letters* **36** 1296-1298, (2011).

[160] Maier S.A.; Plasmonics: The benefits of darkness; *Nat Mater* **8** 699-700, (2009).

[161] Li K., Li X., Stockman M.I. and Bergman D.J.; Surface plasmon amplification by stimulated emission in nanolenses; *Physical Review B* **71** 115409, (2005).

[162] Plum E., Fedotov V.A., Kuo P., Tsai D.P. and Zheludev N.I.; Towards the lasing spaser: controlling metamaterial optical response with semiconductor quantum dots; *Opt. Express* **17** 8548-8551, (2009).

[163] De Leon I. and Berini P.; Amplification of long-range surface plasmons by a dipolar gain medium; *Nat Photon* **4** 382-387, (2010).

[164] Kitur J.K., Podolskiy V.A. and Noginov M.A.; Stimulated Emission of Surface Plasmon Polaritons in a Microcylinder Cavity; *Physical Review Letters* **106** 183903, (2011).

[165] Noginov M.A., Zhu G., Mayy M., Ritzo B.A., Noginova N. and Podolskiy V.A.; Stimulated Emission of Surface Plasmon Polaritons; *Physical Review Letters* **101** 226806, (2008).

[166] Seidel J., Grafström S. and Eng L.; Stimulated Emission of Surface Plasmons at the Interface between a Silver Film and an Optically Pumped Dye Solution; *Physical Review Letters* **94** 177401, (2005).

[167] Xiao S., Drachev V.P., Kildishev A.V., Ni X., Chettiar U.K., Yuan H.-K. and Shalaev V.M.; Loss-free and active optical negative-index metamaterials; *Nature* **466** 735-738, (2010).

[168] Yablonovitch E. and Cody G.D.; Intensity enhancement in textured optical sheets for solar cells; *Electron Devices, IEEE Transactions on* **29** 300-305, (1982).

[169] Stuart H.R. and Hall D.G.; Absorption enhancement in silicon-on-insulator waveguides using metal island films; *Applied Physics Letters* **69** 2327-2329, (1996).

[170] Stuart H.R. and Hall D.G.; Island size effects in nanoparticle-enhanced photodetectors; *Applied Physics Letters* **73** 3815-3817, (1998).

[171] Bohren C.F. and Huffman D.R.; *Absorption and Scattering of Light by Small Particles*; (Ney York, United States of America: John Wiley & Sons, Inc.); **1983**.

[172] Manley P., Burger S., Schmidt F. and Schmid M.; *Progress in Nonlinear Nano-Optics (Design Principles for Plasmonic Nanoparticle Devices, p. 223-247)*; (Heidelberg, Germany: Springer International Publishing); **2015**.

[173] Morawiec S., Mendes M.J., Mirabella S., Simone F., Priolo F. and Crupi I.; Self-assembled silver nanoparticles for plasmon-enhanced solar cell back reflectors: correlation between structural and optical properties; *Nanotechnology* **24** 265601, (2013).

[174] Pillai S., Catchpole K.R., Trupke T. and Green M.A.; Surface plasmon enhanced silicon solar cells; *Journal of Applied Physics* **101** 093105, (2007).

[175] Er-Chien W., Mokkapati S., Soderstrom T., Varlamov S. and Catchpole K.R.; Effect of Nanoparticle Size Distribution on the Performance of Plasmonic Thin-Film Solar Cells: Monodisperse Versus Multidisperse Arrays; *Photovoltaics, IEEE Journal of* **3** 267-270, (2013).

[176] Spinelli P., Hebbink M., de Waele R., Black L., Lenzmann F. and Polman A.; Optical Impedance Matching Using Coupled Plasmonic Nanoparticle Arrays; *Nano Letters* **11** 1760-1765, (2011).

[177] Nakayama K., Tanabe K. and Atwater H.A.; Plasmonic nanoparticle enhanced light absorption in GaAs solar cells; *Applied Physics Letters* **93** -, (2008).

[178] Chen X., Jia B., Saha J.K., Cai B., Stokes N., Qiao Q., Wang Y., Shi Z. and Gu M.; Broadband Enhancement in Thin-Film Amorphous Silicon Solar Cells Enabled by Nucleated Silver Nanoparticles; *Nano Letters* **12** 2187-2192, (2012).

[179] de Souza M.L., Corio P. and Brolo A.G.; Cu nanoparticles enable plasmonic-improved silicon photovoltaic devices; *Physical Chemistry Chemical Physics* **14** 15722-15728, (2012).

[180] Ho C.-I., Yeh D.-J., Su V.-C., Yang C.-H., Yang P.-C., Pu M.-Y., Kuan C.-H., Cheng I.-C. and Lee S.-C.; Plasmonic multilayer nanoparticles enhanced photocurrent in thin film hydrogenated amorphous silicon solar cells; *Journal of Applied Physics* **112** 023113, (2012).

[181] Matheu P., Lim S.H., Derkacs D., McPheeters C. and Yu E.T.; Metal and dielectric nanoparticle scattering for improved optical absorption in photovoltaic devices; *Applied Physics Letters* **93** 113108, (2008).

[182] Mendes M.J., Morawiec S., Crupi I., Simone F. and Priolo F.; Colloidal Self-assembled Nanosphere Arrays for Plasmon-enhanced Light Trapping in Thin Film Silicon Solar Cells; *Energy Procedia* **44** 184-191, (2014).

[183] Yang Y., Pillai S., Mehrvarz H. and Green M.A.; Plasmonic degradation and the importance of over-coating metal nanoparticles for a plasmonic solar cell; *Solar Energy Materials and Solar Cells* **122** 208-216, (2014).

[184] Rand B.P., Peumans P. and Forrest S.R.; Long-range absorption enhancement in organic tandem thin-film solar cells containing silver nanoclusters; *Journal of Applied Physics* **96** 7519-7526, (2004).

[185] Hägglund C., Zäch M. and Kasemo B.; Enhanced charge carrier generation in dye sensitized solar cells by nanoparticle plasmons; *Applied Physics Letters* **92** 013113, (2008).

[186] Westphalen M., Kreibig U., Rostalski J., Lüth H. and Meissner D.; Metal cluster enhanced organic solar cells; *Solar Energy Materials and Solar Cells* **61** 97-105, (2000).

[187] Konda R.B., Mundle R., Mustafa H., Bamiduro O., Pradhan A.K., Roy U.N., Cui Y. and Burger A.; Surface plasmon excitation via Au nanoparticles in n-CdSe⁄p-Si heterojunction diodes; *Applied Physics Letters* **91** 191111, (2007).

[188] Dionne J.A., Sweatlock L.A., Atwater H.A. and Polman A.; Planar metal plasmon waveguides: frequency-dependent dispersion, propagation, localization, and loss beyond the free electron model; *Physical Review B* **72** 075405, (2005).

[189] Tvingstedt K., Persson N.-K., Inganäs O., Rahachou A. and Zozoulenko I.V.; Surface plasmon increase absorption in polymer photovoltaic cells; *Applied Physics Letters* **91** 113514, (2007).

[190] Ferry V.E., Verschuuren M.A., Li H.B.T., Schropp R.E.I., Atwater H.A. and Polman A.; Improved red-response in thin film a-Si:H solar cells with soft-imprinted plasmonic back reflectors; *Applied Physics Letters* **95** 183503, (2009).

[191] Mapel J.K., Singh M., Baldo M.A. and Celebi K.; Plasmonic excitation of organic double heterostructure solar cells; *Applied Physics Letters* **90** 121102, (2007).

[192] Heidel T.D., Mapel J.K., Singh M., Celebi K. and Baldo M.A.; Surface plasmon polariton mediated energy transfer in organic photovoltaic devices; *Applied Physics Letters* **91** 093506, (2007).

[193] Kreibig U. and Fragstein C.v.; The limitation of electron mean free path in small silver particles; *Z. Physik* **224** 307-323, (1969).

[194] Link S. and El-Sayed M.A.; Spectral Properties and Relaxation Dynamics of Surface Plasmon Electronic Oscillations in Gold and Silver Nanodots and Nanorods; *The Journal of Physical Chemistry B* **103** 8410-8426, (1999).

[195] Kolwas K. and Derkachova A.; Plasmonic abilities of gold and silver spherical nanoantennas in terms of size dependent multipolar resonance frequencies and plasmon damping rates; *Opto-Electron. Rev.* **18** 429-437, (2010).

[196] Rodríguez-Fernández J., Pérez-Juste J., García de Abajo F.J. and Liz-Marzán L.M.; Seeded Growth of Submicron Au Colloids with Quadrupole Plasmon Resonance Modes; *Langmuir* **22** 7007-7010, (2006).

[197] Skrabalak S.E., Chen J., Sun Y., Lu X., Au L., Cobley C.M. and Xia Y.; Gold Nanocages: Synthesis, Properties, and Applications; *Accounts of Chemical Research* **41** 1587-1595, (2008).

[198] Millstone J.E., Park S., Shuford K.L., Qin L., Schatz G.C. and Mirkin C.A.; Observation of a Quadrupole Plasmon Mode for a Colloidal Solution of Gold Nanoprisms; *Journal of the American Chemical Society* **127** 5312-5313, (2005).

[199] Li C., Shuford K.L., Park Q.H., Cai W., Li Y., Lee E.J. and Cho S.O.; High-Yield Synthesis of Single-Crystalline Gold Nano-octahedra; *Angewandte Chemie* **119** 3328-3332, (2007).

[200] Sánchez-Iglesias A., Pastoriza-Santos I., Pérez-Juste J., Rodríguez-González B., García de Abajo F.J. and Liz-Marzán L.M.; Synthesis and Optical Properties of Gold Nanodecahedra with Size Control; *Advanced Materials* **18** 2529-2534, (2006).

[201] Sönnichsen C., Franzl T., Wilk T., von Plessen G., Feldmann J., Wilson O. and Mulvaney P.; Drastic Reduction of Plasmon Damping in Gold Nanorods; *Physical Review Letters* **88** 077402, (2002).

[202] Mock J.J., Smith D.R. and Schultz S.; Local Refractive Index Dependence of Plasmon Resonance Spectra from Individual Nanoparticles; *Nano Letters* **3** 485-491, (2003).

[203] Mohapatra S., Mishra Y.K., Avasthi D.K., Kabiraj D., Ghatak J. and Varma S.; Synthesis of gold-silicon core-shell nanoparticles with tunable localized surface plasmon resonance; *Applied Physics Letters* **92** 103105, (2008).

[204] Kewes G.; *Individual Nanoscopic Modes for Active Nanooptics*; (Dissertation: Humboldt Universität zu Berlin); **2015**.

[205] Kewes G., Rodríguez-Oliveros R., Höfner K., Kuhlicke A., Benson O. and Busch K.; Threshold Limitations of the SPASER; **arXiv:1408.7054v1 [physics.optics]** (2014).

[206] Kewes G., Rodríguez-Oliveros R., Höfner K., Kuhlicke A., Benson O. and Busch K.; A fully nanoscopic dielectric laser; **arXiv:1412.4549 [physics.optics]** (2014).

[207] Vigderman L. and Zubarev E.R.; High-Yield Synthesis of Gold Nanorods with Longitudinal SPR Peak Greater than 1200 nm Using Hydroquinone as a Reducing Agent; *Chemistry of Materials* **25** 1450-1457, (2013).

[208] Kresge C.T., Leonowicz M.E., Roth W.J., Vartuli J.C. and Beck J.S.; Ordered mesoporous molecular sieves synthesized by a liquid-crystal template mechanism; *Nature* **359** 710-712, (1992).

[209] Meng X., Kildishev A.V., Fujita K., Tanaka K. and Shalaev V.M.; Wavelength-Tunable Spasing in the Visible; *Nano Letters* **13** 4106-4112, (2013).

[210] Rogach A.L., Franzl T., Klar T.A., Feldmann J., Gaponik N., Lesnyak V., Shavel A., Eychmüller A., Rakovich Y.P. and Donegan J.F.; Aqueous Synthesis of Thiol-Capped CdTe Nanocrystals: State-of-the-Art; *The Journal of Physical Chemistry C* **111** 14628-14637, (2007).

[211] Song L., Hennink E.J., Young I.T. and Tanke H.J.; Photobleaching kinetics of fluorescein in quantitative fluorescence microscopy; *Biophysical Journal* **68** 2588-2600, (1995).

[212] Lambright S., Butaeva E., Razgoniaeva N., Hopkins T., Smith B., Perera D., Corbin J., Khon E., Thomas R., Moroz P., Mereshchenko A., Tarnovsky A. and Zamkov M.; Enhanced Lifetime of Excitons in Nonepitaxial Au/CdS Core/Shell Nanocrystals; *ACS Nano* **8** 352-361, (2014).

[213] Baldeck P.L., Navarro J., Micouin G., Gabudean A.M., Lerouge F., Monnerau C., Chaput F., Andraud C. and Parola S. 2014 Ultrabright and bleaching-resistant hybrid gold nanoparticles for confocal and two-photon fluorecence imaging(vol 8956) p 89560T-89560T-89564

[214] Geddes C.D., Cao H. and Lakowicz J.R.; Enhanced photostability of ICG in close proximity to gold colloids; *Spectrochimica Acta Part A: Molecular and Biomolecular Spectroscopy* **59** 2611-2617, (2003).

[215] Navarro J.R.G., Lerouge F., Micouin G., Cepraga C., Favier A., Charreyre M.T., Blanchard N.P., Lerme J., Chaput F., Focsan M., Kamada K., Baldeck P.L. and Parola S.; Plasmonic bipyramids for fluorescence enhancement and protection against photobleaching; *Nanoscale* **6** 5138-5145, (2014).

[216] Vasilev K., Stefani F.D., Jacobsen V., Knoll W. and Kreiter M.; Reduced photobleaching of chromophores close to a metal surface; *The Journal of Chemical Physics* **120** 6701-6704, (2004).

[217] Zaiba S., Lerouge F., Gabudean A.-M., Focsan M., Lermé J., Gallavardin T., Maury O., Andraud C., Parola S. and Baldeck P.L.; Transparent Plasmonic Nanocontainers Protect Organic Fluorophores against Photobleaching; *Nano Letters* **11** 2043-2047, (2011).

[218] Saxena V., Sadoqi M. and Shao J.; Enhanced photo-stability, thermal-stability and aqueous-stability of indocyanine green in polymeric nanoparticulate systems; *Journal of Photochemistry and Photobiology B: Biology* **74** 29-38, (2004).

[219] Penzkofer A. and Lu Y.; Fluorescence quenching of rhodamine 6G in methanol at high concentration; *Chemical Physics* **103** 399-405, (1986).

[220] Su H., Zhong Y., Ming T., Wang J. and Wong K.S.; Extraordinary Surface Plasmon Coupled Emission Using Core/Shell Gold Nanorods; *The Journal of Physical Chemistry C* **116** 9259-9264, (2012).

[221] Baker D.R. and Kamat P.V.; Tuning the Emission of CdSe Quantum Dots by Controlled Trap Enhancement; *Langmuir* **26** 11272-11276, (2010).

[222] Gaunt J.A., Knight A.E., Windsor S.A. and Chechik V.; Stability and quantum yield effects of small molecule additives on solutions of semiconductor nanoparticles; *Journal of Colloid and Interface Science* **290** 437-443, (2005).

[223] Wuister S.F., Swart I., van Driel F., Hickey S.G. and de Mello Donegá C.; Highly Luminescent Water-Soluble CdTe Quantum Dots; *Nano Letters* **3** 503-507, (2003).

[224] van Sark W.G.J.H.M., Frederix P.L.T.M., Bol A.A., Gerritsen H.C. and Meijerink A.; Blueing, Bleaching, and Blinking of Single CdSe/ZnS Quantum Dots; *ChemPhysChem* **3** 871-879, (2002).

[225] Yu Y., Rowland C.E., Schaller R.D. and Korgel B.A.; Synthesis and Ligand Exchange of Thiol-Capped Silicon Nanocrystals; *Langmuir* **31** 6886-6893, (2015).

[226] Boldt K., Bruns O.T., Gaponik N. and Eychmüller A.; Comparative Examination of the Stability of Semiconductor Quantum Dots in Various Biochemical Buffers; *The Journal of Physical Chemistry B* **110** 1959-1963, (2006).

[227] Biju V., Makita Y., Sonoda A., Yokoyama H., Baba Y. and Ishikawa M.; Temperature-Sensitive Photoluminescence of CdSe Quantum Dot Clusters; *The Journal of Physical Chemistry B* **109** 13899-13905, (2005).

[228] Morello G., De Giorgi M., Kudera S., Manna L., Cingolani R. and Anni M.; Temperature and Size Dependence of Nonradiative Relaxation and Exciton−Phonon Coupling in Colloidal CdTe Quantum Dots; *The Journal of Physical Chemistry C* **111** 5846-5849, (2007).

[229] Blokland J.H., Claessen V.I., Wijnen F.J.P., Groeneveld E., de Mello Donegá C., Vanmaekelbergh D., Meijerink A., Maan J.C. and Christianen P.C.M.; Exciton lifetimes of CdTe nanocrystal quantum dots in high magnetic fields; *Physical Review B* **83** 035304, (2011).

[230] Karan S., Majumder M. and Mallik B.; Controlled surface trap state photoluminescence from CdS QDs impregnated in poly(methyl methacrylate); *Photochemical & Photobiological Sciences* **11** 1220-1232, (2012).

[231] Bera D., Qian L., Tseng T.-K. and Holloway P.H.; Quantum Dots and Their Multimodal Applications: A Review; *Materials* **3** 2260, (2010).

[232] LeBlanc S.J., McClanahan M.R., Jones M. and Moyer P.J.; Enhancement of Multiphoton Emission from Single CdSe Quantum Dots Coupled to Gold Films; *Nano Letters* **13** 1662-1669, (2013).

[233] Wu J., Lee S., Reddy V.R., Manasreh M.O., Weaver B.D., Yakes M.K., Furrow C.S., Kunets V.P., Benamara M. and Salamo G.J.; Photoluminescence plasmonic enhancement in InAs quantum dots coupled to gold nanoparticles; *Materials Letters* **65** 3605-3608, (2011).

[234] Ma X., Tan H., Kipp T. and Mews A.; Fluorescence Enhancement, Blinking Suppression, and Gray States of Individual Semiconductor Nanocrystals Close to Gold Nanoparticles; *Nano Letters* **10** 4166-4174, (2010).

[235] Cremes D.A. and Radziemski L.J.; *Handbook of Laser-Induced Breakdown Spectroscopy, Second Edition*; (Chichester, U. K.: John Wiley & Sons, Ltd); **2013**.

[236] McGehee M.D., Gupta R., Veenstra S., Miller E.K., Díaz-García M.A. and Heeger A.J.; Amplified spontaneous emission from photopumped films of a conjugated polymer; *Physical Review B* **58** 7035-7039, (1998).

[237] Yang P., Wirnsberger G., Huang H.C., Cordero S.R., McGehee M.D., Scott B., Deng T., Whitesides G.M., Chmelka B.F., Buratto S.K. and Stucky G.D.; Mirrorless Lasing from Mesostructured Waveguides Patterned by Soft Lithography; *Science* **287** 465-467, (2000).

[238] Chen Y.-H., Li J., Ren M.-L., Wang B.-L., Fu J.-X., Liu S.-Y. and Li Z.-Y.; Direct observation of amplified spontaneous emission of surface plasmon polaritons at metal/dielectric interfaces; *Applied Physics Letters* **98** 261912, (2011).

[239] Popov O., Zilbershtein A. and Davidov D.; Random lasing from dye-gold nanoparticles in polymer films: Enhanced gain at the surface-plasmon-resonance wavelength; *Applied Physics Letters* **89** 191116, (2006).

[240] Leatherdale C.A., Woo W.K., Mikulec F.V. and Bawendi M.G.; On the Absorption Cross Section of CdSe Nanocrystal Quantum Dots; *The Journal of Physical Chemistry B* **106** 7619-7622, (2002).

[241] Osborne S.W., Blood P., Smowton P.M., Xin Y.C., Stintz A., Huffaker D. and Lester L.F.; Optical absorption cross section of quantum dots; *Journal of Physics: Condensed Matter* **16** S3749, (2004).

[242] Yu P., Beard M.C., Ellingson R.J., Ferrere S., Curtis C., Drexler J., Luiszer F. and Nozik A.J.; Absorption Cross-Section and Related Optical Properties of Colloidal InAs Quantum Dots; *The Journal of Physical Chemistry B* **109** 7084-7087, (2005).

[243] Evanoff D.D. and Chumanov G.; Size-Controlled Synthesis of Nanoparticles. 2. Measurement of Extinction, Scattering, and Absorption Cross Sections; *The Journal of Physical Chemistry B* **108** 13957-13962, (2004).

[244] Segelstein D.J. 1981 The complex refractive index of water. (Kansas City, Missouri: University of Missouri-Kansas City)

[245] Ingham B., Lim T.H., Dotzler C.J., Henning A., Toney M.F. and Tilley R.D.; How Nanoparticles Coalesce: An in Situ Study of Au Nanoparticle Aggregation and Grain Growth; *Chemistry of Materials* **23** 3312-3317, (2011).

[246] Moon K.-S., Dong H., Maric R., Pothukuchi S., Hunt A., Li Y. and Wong C.P.; Thermal behavior of silver nanoparticles for low-temperature interconnect applications; *Journal of Elec Materi* **34** 168-175, (2005).

[247] Pinkhasova P., Chen H., Verhoeven M.W.G.M., Sukhishvili S. and Du H.; Thermally annealed Ag nanoparticles on anodized aluminium oxide for SERS sensing; *RSC Advances* **3** 17954-17961, (2013).

[248] Trügler A., Tinguely J.-C., Krenn J.R., Hohenau A. and Hohenester U.; Influence of surface roughness on the optical properties of plasmonic nanoparticles; *Physical Review B* **83** 081412, (2011).

[249] Günendi M.C., Tanyeli r., Akgüç G.B., Bek A., Turan R.i. and Gülseren O.u.; Understanding the plasmonic properties of dewetting formed Ag nanoparticles for large area solar cell applications; *Opt. Express* **21** 18344-18353, (2013).

[250] Hairen T., Santbergen R., Guangtao Y., Smets A.H.M. and Zeman M.; Combined Optical and Electrical Design of Plasmonic Back Reflector for High-Efficiency Thin-Film Silicon Solar Cells; *Photovoltaics, IEEE Journal of* **3** 53-58, (2013).

[251] Mendes M.J., Morawiec S., Simone F., Priolo F. and Crupi I.; Colloidal plasmonic back reflectors for light trapping in solar cells; *Nanoscale* **6** 4796-4805, (2014).

[252] Tan H., Santbergen R., Smets A.H.M. and Zeman M.; Plasmonic Light Trapping in Thin-film Silicon Solar Cells with Improved Self-Assembled Silver Nanoparticles; *Nano Letters* **12** 4070-4076, (2012).

[253] Weaver J.F. and Hoflund G.B.; Surface Characterization Study of the Thermal Decomposition of AgO; *The Journal of Physical Chemistry* **98** 8519-8524, (1994).

[254] Grillet N., Manchon D., Cottancin E., Bertorelle F., Bonnet C., Broyer M., Lermé J. and Pellarin M.; Photo-Oxidation of Individual Silver Nanoparticles: A Real-Time Tracking of Optical and Morphological Changes; *The Journal of Physical Chemistry C* **117** 2274-2282, (2013).

[255] Pol V.G., Srivastava D.N., Palchik O., Palchik V., Slifkin M.A., Weiss A.M. and Gedanken A.; Sonochemical Deposition of Silver Nanoparticles on Silica Spheres; *Langmuir* **18** 3352-3357, (2002).

[256] Yin Y., Li Z.-Y., Zhong Z., Gates B., Xia Y. and Venkateswaran S.; Synthesis and characterization of stable aqueous dispersions of silver nanoparticles through the Tollens process; *Journal of Materials Chemistry* **12** 522-527, (2002).

[257] Waterhouse G.I.N., Bowmaker G.A. and Metson J.B.; The thermal decomposition of silver (I, III) oxide: A combined XRD, FT-IR and Raman spectroscopic study; *Physical Chemistry Chemical Physics* **3** 3838-3845, (2001).

[258] Han Y., Lupitskyy R., Chou T.-M., Stafford C.M., Du H. and Sukhishvili S.; Effect of Oxidation on Surface-Enhanced Raman Scattering Activity of Silver Nanoparticles: A Quantitative Correlation; *Analytical Chemistry* **83** 5873-5880, (2011).

[259] Schinca D.C., Scaffardi L.B., Videla F.A., Torchia G.A., Moreno P. and Roso L.; Silver–silver oxide core–shell nanoparticles by femtosecond laser ablation: core and shell sizing by extinction spectroscopy; *Journal of Physics D: Applied Physics* **42** 215102, (2009).

[260] Akimov Y. and Koh W.; Design of Plasmonic Nanoparticles for Efficient Subwavelength Light Trapping in Thin-Film Solar Cells; *Plasmonics* **6** 155-161, (2011).

[261] Al-Kuhaili M.F.; Characterization of thin films produced by the thermal evaporation of silver oxide; *Journal of Physics D: Applied Physics* **40** 2847, (2007).

[262] Volkman S.K., Yin S., Bakhishev T., Puntambekar K., Subramanian V. and Toney M.F.; Mechanistic Studies on Sintering of Silver Nanoparticles; *Chemistry of Materials* **23** 4634-4640, (2011).

[263] Söderström K., Haug F.J., Escarré J., Pahud C., Biron R. and Ballif C.; Highly reflective nanotextured sputtered silver back reflector for flexible high-efficiency n–i–p thin-film silicon solar cells; *Solar Energy Materials and Solar Cells* **95** 3585-3591, (2011).

[264] Sotelo J., Ederth J. and Niklasson G.; Optical properties of polycrystalline metallic films; *Physical Review B* **67** 195106, (2003).

[265] Kojima A., Teshima K., Shirai Y. and Miyasaka T.; Organometal Halide Perovskites as Visible-Light Sensitizers for Photovoltaic Cells; *Journal of the American Chemical Society* **131** 6050-6051, (2009).

[266] Zhou H., Chen Q., Li G., Luo S., Song T.-b., Duan H.-S., Hong Z., You J., Liu Y. and Yang Y.; Interface engineering of highly efficient perovskite solar cells; *Science* **345** 542-546, (2014).

[267] Lin Q., Armin A., Nagiri R.C.R., Burn P.L. and Meredith P.; Electro-optics of perovskite solar cells; *Nat Photon* **9** 106-112, (2015).

[268] Collavini S., Völker S.F. and Delgado J.L.; Understanding the Outstanding Power Conversion Efficiency of Perovskite-Based Solar Cells; *Angewandte Chemie International Edition* **54** 9757-9759, (2015).

[269] Stranks S.D., Eperon G.E., Grancini G., Menelaou C., Alcocer M.J.P., Leijtens T., Herz L.M., Petrozza A. and Snaith H.J.; Electron-Hole Diffusion Lengths Exceeding 1 Micrometer in an Organometal Trihalide Perovskite Absorber; *Science* **342** 341-344, (2013).

[270] Eperon G.E., Stranks S.D., Menelaou C., Johnston M.B., Herz L.M. and Snaith H.J.; Formamidinium lead trihalide: a broadly tunable perovskite for efficient planar heterojunction solar cells; *Energy & Environmental Science* **7** 982-988, (2014).

[271] Das S. and Asefa T.; Core–Shell–Shell Microsphere Catalysts Containing Au Nanoparticles for Styrene Epoxidation; *Top Catal* **55** 587-594, (2012).

[272] Darrah Thomas T. and Weightman P.; Valence electronic structure of AuZn and AuMg alloys derived from a new way of analyzing Auger-parameter shifts; *Physical Review B* **33** 5406-5413, (1986).

[273] Jeon N.J., Noh J.H., Kim Y.C., Yang W.S., Ryu S. and Seok S.I.; Solvent engineering for high-performance inorganic–organic hybrid perovskite solar cells; *Nat Mater* **13** 897-903, (2014).

[274] Löper P., Stuckelberger M., Niesen B., Werner J., Filipič M., Moon S.-J., Yum J.-H., Topič M., De Wolf S. and Ballif C.; Complex Refractive Index Spectra of CH3NH3PbI3 Perovskite Thin Films Determined by Spectroscopic Ellipsometry and Spectrophotometry; *The Journal of Physical Chemistry Letters* **6** 66-71, (2015).

[275] Wang S., Ma F., Zhao H. and Wu N.; Bulk Synthesis of Metal–Organic Hybrid Dimers and Their Propulsion under Electric Fields; *ACS Applied Materials & Interfaces* **6** 4560-4569, (2014).

[276] Moon G.D., Lee T.I., Kim B., Chae G., Kim J., Kim S., Myoung J.-M. and Jeong U.; Assembled Monolayers of Hydrophilic Particles on Water Surfaces; *ACS Nano* **5** 8600-8612, (2011).

[277] Loo C., Lin A., Hirsch L., Lee M.-H., Barton J., Halas N., West J. and Drezek R.; Nanoshell-Enabled Photonics-Based Imaging and Therapy of Cancer; *Technology in Cancer Research & Treatment* **3** 33-40, (2004).

[278] Duraiswamy S. and Khan S.A.; Plasmonic Nanoshell Synthesis in Microfluidic Composite Foams; *Nano Letters* **10** 3757-3763, (2010).

[279] Qian J., Chen Z., Chen J., Li Y., Xu J. and Sun Q.; Two-dimensional angularly selective optical properties of gold nanoshell with holes; *Opt. Express* **20** 14614-14620, (2012).

[280] Wu S., Schell A., Lublow M., Kaiser J., Aichele T., Schietinger S., Polzer F., Kühn S., Guo X., Benson O., Ballauff M. and Lu Y.; Silica-coated Au/Ag nanorods with tunable surface plasmon bands for nanoplasmonics with single particles; *Colloid Polym Sci* **291** 585-594, (2013).

[281] Brinson B.E., Lassiter J.B., Levin C.S., Bardhan R., Mirin N. and Halas N.J.; Nanoshells Made Easy: Improving Au Layer Growth on Nanoparticle Surfaces; *Langmuir* **24** 14166-14171, (2008).

[282] Falcão-Filho E.L., Barbosa-Silva R., Sobral-Filho R.G., Brito-Silva A.M., Galembeck A. and de Araújo C.B.; High-order nonlinearity of silica-gold nanoshells in chloroform at 1560 nm; *Opt. Express* **18** 21636-21644, (2010).

[283] Lim Y.T., Park O.O. and Jung H.-T.; Gold nanolayer-encapsulated silica particles synthesized by surface seeding and shell growing method: near infrared responsive materials; *Journal of Colloid and Interface Science* **263** 449-453, (2003).

[284] Weber V., Feis A., Gellini C., Pilot R., Salvi P.R. and Signorini R.; Far- and near-field properties of gold nanoshells studied by photoacoustic and surface-enhanced Raman spectroscopies; *Physical Chemistry Chemical Physics* **17** 21190-21197, (2015).

[285] Wu C., Yu C. and Chu M.; A gold nanoshell with a silica inner shell synthesized using liposome templates for doxorubicin loading and near-infrared photothermal therapy; *International Journal of Nanomedicine* **6** 807-813, (2011).

[286] Yuetong X., Wensheng L. and Long J.; Fabrication of color changeable polystyrene spheres decorated by gold nanoparticles and their label-free biosensing; *Nanotechnology* **21** 085501, (2010).

[287] Bergmann K. and O'Konski C.T.; A SPECTROSCOPIC STUDY OF METHYLENE BLUE MONOMER, DIMER, AND COMPLEXES WITH MONTMORILLONITE; *The Journal of Physical Chemistry* **67** 2169-2177, (1963).

[288] Lewschin W.L.; Die Auslöschung der Fluoreszenz in festen und flüssigen Farbstofflösungen; *Z. Physik* **43** 230-253, (1927).

[289] Rabinowitch E. and Epstein L.F.; Polymerization of Dyestuffs in Solution. Thionine and Methylene Blue1; *Journal of the American Chemical Society* **63** 69-78, (1941).

[290] Rösch U., Yao S., Wortmann R. and Würthner F.; Fluorescent H-Aggregates of Merocyanine Dyes; *Angewandte Chemie International Edition* **45** 7026-7030, (2006).

[291] Selvin P.R.; The renaissance of fluorescence resonance energy transfer; *Nat Struct Mol Biol* **7** 730-734, (2000).

[292] Yang P., Gai S. and Lin J.; Functionalized mesoporous silica materials for controlled drug delivery; *Chemical Society Reviews* **41** 3679-3698, (2012).

[293] Zha L., Banik B. and Alexis F.; Stimulus responsive nanogels for drug delivery; *Soft Matter* **7** 5908-5916, (2011).

[294] Abdelmohsen L.K.E.A., Peng F., Tu Y. and Wilson D.A.; Micro- and nano-motors for biomedical applications; *Journal of Materials Chemistry B* **2** 2395-2408, (2014).

[295] Degen P.; Self-propelling capsules as artificial microswimmers; *Current Opinion in Colloid & Interface Science* **19** 611-619, (2014).

[296] Ebbens S., Gregory D.A., Dunderdale G., Howse J.R., Ibrahim Y., Liverpool T.B. and Golestanian R.; Electrokinetic effects in catalytic platinum-insulator Janus swimmers; *EPL (Europhysics Letters)* **106** 58003, (2014).

[297] Ebbens S.J. and Howse J.R.; In pursuit of propulsion at the nanoscale; *Soft Matter* **6** 726-738, (2010).

[298] Ke H., Ye S., Carroll R.L. and Showalter K.; Motion Analysis of Self-Propelled Pt−Silica Particles in Hydrogen Peroxide Solutions; *The Journal of Physical Chemistry A* **114** 5462-5467, (2010).

[299] Lee T.-C., Alarcón-Correa M., Miksch C., Hahn K., Gibbs J.G. and Fischer P.; Self-Propelling Nanomotors in the Presence of Strong Brownian Forces; *Nano Letters* **14** 2407-2412, (2014).

[300] Bianchi G., Mazza F. and Mussini T.; Catalytic decomposition of acid hydrogen peroxide solutions on platinum, iridium, palladium and gold surfaces; *Electrochimica Acta* **7** 457-473, (1962).

[301] Howse J.R., Jones R.A.L., Ryan A.J., Gough T., Vafabakhsh R. and Golestanian R.; Self-Motile Colloidal Particles: From Directed Propulsion to Random Walk; *Physical Review Letters* **99** 048102, (2007).

[302] Golestanian R., Liverpool T.B. and Ajdari A.; Designing phoretic micro- and nano-swimmers; *New Journal of Physics* **9** 126, (2007).

[303] Kaieda S., Lund M., Plivelic T.S. and Halle B.; Weak Self-Interactions of Globular Proteins Studied by Small-Angle X-ray Scattering and Structure-Based Modeling; *The Journal of Physical Chemistry B* **118** 10111-10119, (2014).

[304] Li W., Persson B.A., Morin M., Behrens M.A., Lund M. and Zackrisson Oskolkova M.; Charge-Induced Patchy Attractions between Proteins; *The Journal of Physical Chemistry B* **119** 503-508, (2015).

[305] Chu F., Polzer F., Severin N., Lu Y., Ott A., Rabe J. and Ballauff M.; Thermosensitive hollow Janus dumbbells; *Colloid Polym Sci* **292** 1785-1793, (2014).

[306] Skrabalak S.E., Au L., Li X. and Xia Y.; Facile synthesis of Ag nanocubes and Au nanocages; *Nat. Protocols* **2** 2182-2190, (2007).

[307] Berne B.J. and Pecora R.; *Dynamic Light Scattering: With Applications to Chemistry, Biology, and Physics*; (New York: Dover Publications, INC.); **2000**.

[308] Einstein A.; Über die von der molekularkinetischen Theorie der Wärme geforderte Bewegung von in ruhenden Flüssigkeiten suspendierten Teilchen; *Annalen der Physik* **322** 549-560, (1905).

[309] Singh A.K.; *Advanced X-ray Techniques in Research and Industries*; (Amsterdam: IOS Press); **2005**.

List of Figures

List of Tables

Abbreviations

Symbols

α	polarizability
a	radius
A	absorbance
β	correction factor of DLS instrument
c	concentration or speed of light
δ	chemical shift
Δ	crystallite size
$(\Delta x)^2$	mean square displacement
d	crystal-plane distance
D	displacement field
D_R	rotational diffusion coefficient
D_T	translational diffusion coefficient
ε	dielectric constant
E	electric field
E_B	binding energy
E_{kin}	kinetic energy
η	viscosity of efficiency
FF	fill factor
F_P	Purcell factor
g	gain factor
Γ	decay rate
I	Intensity
I_{SC}	short circuit current
k	wavevector
k_B	Boltzmann constant
K	shape-factor of crystallite
λ	wavelength
l	length
L	ellipsoid shape-factor
μ_e	electrophoretic mobility
M	molar mass
n	refractive index
N	number
P	power
Q	quality factor
$q2$	scattering vector
ρ	density
σ	cross section
r	radius
R_h	hydrodynamic radius
τ	decay- / life time
θ	scattering angle
t	time
T	temperature
υ	velocity
υ_m	mode volume
V	volume

V_{OC}	open circuit voltage
ω	angular frequency
ζ	zeta potential

Chemicals

AA	ascorbic acid
AF-532	Alexa Fluor 532
Ag_2O	silver oxide
$AgNO_3$	silver nitrate
AIBN	azobisisobutyronitrile
APTES	(3-aminopropyl)triethoxysilane
AR-101	ATTO Rho 101
BAC	*N,N′*-bis(acryloyl)cystamine
CDCl3	deuterated chloroform
CdTe	cadmium telluride
CTAB	cetyltrimethylammonium bromide
DMSO	dimethyl sulfoxide
DVB	divinylbenzene
FMA	fluorescein o-methacrylate
FTO	fluorinated tin oxide
$HAuCl_4$	chlorauric acid
HCl	hydrochloric acid
H_2O_2	hydrogen peroxide
ITC	isothiocyanate
KCN	potassium cyanide
K_2CO_3	potassium carbonate
KPS	potassium persulfate
K_2PtCl_4	potassium tetrachloroplatinate
MMA	methyl methacrylate
MPS	3-(trimethoxysilyl)propyl methacrylate
MPA	3-mercaptopropionic acid
$NaBH_4$	Sodium borohydride
Na_3Cit	sodium citrate
NaCl	sodium chloride
NH_4OH	ammonium hydroxide
NaOH	sodium hydroxide
Na_2S	sodium sulphide
$NaSiO_3$	sodium silicate
NaSS	sodium 4-styrenesulfate
NHS	*N*-hydroxysuccinimide esters
NIPA	*N*-isopropylacrylamide
OG-488	Oregon Green 488
PAA	poly(acrylic acid)
PAH	poly(allylamine hydrochloride)
PMMA	poly(methyl methacrylate)
PNIPA	poly(*N*-isopropylacrylamide)
PS	polystyrene
PVP	polyvinylpyrrolidone
R6G	rhodamine 6G

RhB	rhodamine B
SDS	sodium dodecylsulfate
SiO_2	silica
TEOS	tetraethoxysilane
TiO_2	titanium dioxide

Other abbrevations

Ag	silver
ASE	amplified spontaneous emission
a-Si	amorphous silica
Au	gold
AuNR	gold nanorods
AuNS	gold nanospheres
CG	corning glass
DDLS	depolarized dynamic light scattering
DLS	dynamic light scattering
DLVO	Derjaguin, Landau, Verwey, Overbeek
EQE	external quantum efficiency
fcc	face centred-cubic
FWHM	full width at half maximum
IQE	internal quantum efficiency
IR	infrared
I-V	current-voltage curve
LCST	lower critical solution temperature
Nd:YAG	neodymium-doped yttrium aluminium garnet
NIR	near infrared
NMR	nuclear magnetic resonance spectroscopy
PL	photo luminescence
QD	quantum dot
$R_{diff} + T_{diff}$	scattered light fraction (diffuse reflectance and transmittance)
SEM	scanning electron microscopy
SERS	surface enhanced Raman scattering
SPASER	surface plasmon amplification by stimulated emission of radiation
SPP	surface plasmon polariton
TEM	transmission electron microscopy
Ti:sapphire	titanium-sapphire
UV/Vis	ultraviolet to visible
XPS	X-ray photoelectron spectroscopy
XRD	X-ray diffraction

Acknowledgement

It's a pleasure to thank the many people who helped me during my doctorate time and made this dissertation possible. I experienced a lot of new knowledge, assistance and encouragement owing to these people, which I would like to name here.

First of all I am very grateful to my doctoral advisor Prof. Matthias Ballauff who not only gave me the chance to work in his group, but also introduced me to the fascinating field of metal nanoparticles and plasmonics. I would like to thank him for his constant support in my research, ideas and discussions and for the trust and respect he expressed towards me.

Equally I want to thank Dr. Yan Lu who guided me through my PhD time as my principal advisor. She always had a friendly ear towards my ideas and helped me with a lot of advises and her broad knowledge in synthesis.

Furthermore, special thanks go out to the many collaborators that I was allowed and enjoyed to work with:

I like to thank Prof. Oliver Benson and Dr. Günter Kewes from the Humboldt University Berlin that worked closely with me to strive for the spaser. They provided a profound theoretical background and precious discussions. Günter has not only derived a model to describe the spaser and its working conditions but also did the measurements with the Nd:YAG laser.

I am also very grateful to Dr. Sven Ring who has encouraged me to investigate the large silver nanoparticles and offered a lot of valuable discussions. Moreover he has done the annealing, optical measurements and silicon deposition.

I also want to thank Yang Liu who stimulated the work on the perovskite solar cells and has done the preparation and characterization of the solar cell.

Moreover, I appreciated to work with Dr. Fangfang Chu who has introduced me to the dumbbell-shaped particles and helped me with the synthesis. I also want to thank her for the many nice discussions and the good atmosphere in- and outside of the office.

I also want to express my thanks to many people that have assisted me with my work, i.e. Dr. Guanchao Yin who helped me to measured SEM, XRD and XPS with Alexander Steigert; Dr. Wolfram Calvet who also helped me to measure XPS; Prof. Alexander Eychmüller from the Technical University Dresden who supplied me with the CdTe quantum dots; Carmen Stolze from the Humboldt University Berlin who has measured the NMR spectra for me and Dr. Annegret Günter who has helped me with the analysis of some DLS data.

The financial support is highly appreciated from the Deutsche Forschungsgemeinschaft with the project B2 of the collaborative research centre Sfb-951 (“Hybrid Inorganic Organic Systems”).

Of course I also want to thank all of my colleagues from the HZB for their worthwhile discussions about science and non-scientific distraction in the coffee breaks. I have made a lot of good friends and experienced a beautiful intercultural atmosphere.

Finally, I would like to thank my whole family and in particular my parents Christian and Regina and my brother and his wife Matthias and Denise. They have always supported me in my life and gave me a loving home.

Selbstständigkeitserklärung

Die vorliegende Arbeit wurde selbstständig und nur unter Verwendung der hier genannten Quellen, Hilfen und Hilfsmittel angefertigt.

Ich habe mich nicht anderweitig beworben einen Doktorgrad in dem genannten Promotionsfach zu erlangen und besitze keinen entsprechenden Doktorgrad.

Ich habe Kenntnis über das Verfahren und der Promotionsordnung des dem angestrebten Abschlusses.

Berlin, den 26.01.2016

Andreas Ott